The Connection Between Galaxy Stellar Masses and Dark Matter Halo Masses: Constraints from Semi-Analytic Modeling and Correlation Functions

by

Catherine E. White

A dissertation submitted to The Johns Hopkins University in conformity with the requirements for the degree of Doctor of Philosophy.

Baltimore, Maryland

August, 2016

Abstract

One of the basic observations that galaxy formation models try to reproduce is the buildup of stellar mass in dark matter halos, generally characterized by the stellar mass-halo mass relation, $M_\star\,(M_{\rm halo})$. Models have difficulty matching the observed $M_\star\,(M_{\rm halo})$: modeled low mass galaxies ($M_{\rm halo} \lesssim 10^{11}\ M_\odot$) form their stars significantly earlier than observations suggest. Our goal in this thesis is twofold: first, work with a well-tested semi-analytic model of galaxy formation to explore the physics needed to match existing measurements of the $M_\star\,(M_{\rm halo})$ relation for low mass galaxies and second, use correlation functions to place additional constraints on $M_\star\,(M_{\rm halo})$. For the first project, we introduce idealized physical prescriptions into the semi-analytic model to test the effects of (1) more efficient supernova feedback with a higher mass-loading factor for low mass galaxies at higher redshifts, (2) less efficient star formation with longer star formation timescales at higher redshift, or (3) less efficient gas accretion with longer infall timescales for lower mass galaxies. In addition to $M_\star\,(M_{\rm halo})$, we examine cold gas fractions, star formation rates, and metallicities to characterize the secondary effects of these prescriptions.

ABSTRACT

The technique of abundance matching has been widely used to estimate $M_\star\,(M_{\rm halo})$ at high redshift, and in principle, clustering measurements provide a powerful independent means to derive this relation. Our second project is to measure the $M_\star\,(M_{\rm halo})$ relation from clustering in the CANDELS fields. We measure angular correlation functions in bins of stellar mass over $10^8 M_\odot < M_\star < 10^{12} M_\odot$ and photometric redshifts $1 < z < 6$, then calculate the linear bias from power law fit coefficients. To validate the measurement technique, we perform a careful analysis of the power-law mass measurement on a dark-matter simulation and use this to calibrate the conversion between clustering amplitude and linear bias (and hence, halo mass). Our clustering $M_\star\,(M_{\rm halo})$ relation is in agreement with abundance matching results and the tension between the fiducial semi-analytic model and our best estimates of $M_\star\,(M_{\rm halo})$ remains.

Primary Reader: Harry Ferguson

Secondary Reader: Colin Norman

Acknowledgments

I would like to begin by thanking my advisor, Harry Ferguson, without whom I would not have finished my doctorate. He has been an amazing mentor, challenging me, allowing me to puzzle through most things on my own, and gently guiding me back to the path when I was too far off in the weeds. Throughout, he has been kind and understanding and I could not have asked for a better advisor.

I would also like to thank my husband, who has spent the last several years helping me stay sane, supplying me alternately with advice, comfort, and frozen yogurt. He has also been exceedingly understanding the past few months, picking up chores as I disappeared into my work and always being available for hugs when I needed them.

Thanks to my parents, who have always guided me, supported me, and encouraged me in all of my endeavors. My father has often helped me work through problems, scientific and professional alike, and my mother has always being willing to listen, commiserate, and offer hugs and wonderful food.

Many thanks to Colin Norman and my colleagues on the CANDELS team, in particular Peter Behroozi, Rachel Somerville, Jeff Newman, Eric Gawiser, and Soo

ACKNOWLEDGMENTS

Lee for their support, assistance, and enlightening discussions. Thanks to my friends for their support and encouragement, and particular thanks to Alireza Mortazavi whose revision has significantly improved this work.

Lastly, thanks to my cats, Andromeda and Remy, who blessed this thesis with an abundance of cat hair and provided the occasional adorable distraction.

Dedication

For my father, who inspired my curiosity about the world around me; for my mother, who has always been at my side to support me; and for my husband, who loves me no matter how much I complain about correlation functions.

Contents

List of Tables

List of Figures

Chapter 1

Introduction

The Hubble Space Telescope (HST) has produced some of the most iconic and awe-inspiring images that we have of the universe. From the Pillars of Creation, a star-forming region in our own galaxy, to the nearby Whirlpool Galaxy, to the few-pixels-wide red smudge that is the most distant known galaxy, Hubble has brought the universe to our fingertips.

Perhaps surprisingly, we have only known of the existence of galaxies outside of our own for about a hundred years: Edwin Hubble first measured the distance to the Andromeda galaxy in 1924, showing it to be a large object very far from us. The Andromeda "nebula" was in fact another galaxy comparable to our own. Since then, we have observed millions of galaxies. We have also worked to build an understanding of how galaxies form and evolve. Why do stars form in galaxies rather than spread evenly throughout the universe? How and when do galaxies form their stars? How

is gas heated and cooled? How does galaxy formation fit into our understanding of cosmology? Our current theories do fairly well in reconstructing the broad properties of the galaxies that we observe, but the details are still a work in progress.

In this work, we discuss the buildup of stellar mass in galaxies, a basic and important but not fully-explained aspect of galaxy formation. The time at which a galaxy forms most of its stars is related to the mass of the galaxy: the more massive the galaxy, the earlier its star formation peaked. Today, most low mass galaxies are still forming stars actively while most high mass galaxies finished forming the bulk of their stars more than ten billion years ago. Models have difficulty reproducing this trend, tending to predict earlier star formation in low mass galaxies than is observed. We tackle this both from the modeling side, trying to adapt the theory to match the observations, and from the observational side, using galaxy clustering to constrain the relationship between galaxies' stellar and dark matter masses.

1.1 Cosmological context

The best cosmological model that we have is ΛCDM, shorthand for a model that includes dark energy (Λ) and Cold Dark Matter (CDM). ΛCDM cosmology consists of three main components: dark energy, which is responsible for the acceleration of the expansion of the universe; dark matter, which only interacts gravitationally; and baryonic matter, which is what we think of as "normal matter" and makes up

stars, gas, dust, and planets. The most recent measurements of the composition of the universe from the Planck mission show that the universe is about 68% dark energy, 27% dark matter, and 5% baryonic matter (Planck Collaboration et al., 2015). Despite making up 95% of the mass-energy of the universe, we do not know exactly what dark matter and dark energy are; their existence is inferred from phenomena that cannot be explained by a universe that contains only baryonic matter. We do have constraints on the nature of dark matter from astrophysical probes, particle colliders, and direct or indirect detection experiments, but no conclusive results (Bauer et al., 2015).

The first sign that dark matter existed was the "missing mass problem." There are a few situations in which we can measure the gravitational mass of a galaxy independent of the visible baryonic mass in the form of gas and stars. In all of these situations, we measure more gravitational mass than baryonic mass. The accepted solution to the missing mass problem is to assume that there is mass present that gravitates but does not emit light. This is dark matter. In addition to explaining observations of galaxy masses, dark matter is also an essential part of ΛCDM cosmology . ΛCDM explains a host of observed phenomena including fluctuations in the cosmic microwave background (Spergel et al., 2007), the power spectrum observed via the Lyman α forest (Weinberg et al., 1999; Jena et al., 2005), and strong lensing by galaxy clusters (Horesh et al., 2011).

Most of our detailed knowledge of dark matter behavior comes from simulation

because it is difficult to detect dark matter directly. Dark matter is a relatively simple substance to model because the only relevant force is gravity. Computational models of dark matter evolution, N-body simulations, have been performed on scales from single halos on the order of a hundred million light years across (e.g. Kuhlen et al., 2008) to cosmological volumes tens of billions of light years on a side (e.g. Kim et al., 2011; Angulo et al., 2012). N-body simulations' initial conditions are set by the properties of the density variations in the cosmic microwave background, a time when the universe was nearly homogeneous and much hotter and denser than it is today. As the universe expanded and cooled, gravity pulled material towards over-densities, causing slightly over-dense regions to become more over-dense and slightly under-dense regions to become more under-dense. Eventually, sufficiently over-dense regions collapsed into bound structures. Collapsed dark matter structures are called "halos" and are the eventual sites of galaxy formation.

Very large-scale over-densities in the early universe did not collapse into single halos, but rather into larger-scale structure. The large scale over-densities collapse first along the shortest axis, making a "pancake." That pancake then collapses along the next-shortest axis, forming a filament. Giant clusters form where filaments come together. The end result of this process is the cosmic web, shown in Figure 1.1 by the dark matter mass density from a slice of the Millennium XXL simulation (Angulo et al., 2012).

In Figure 1.1, the dark matter mass density is lowest in the light blue areas, higher

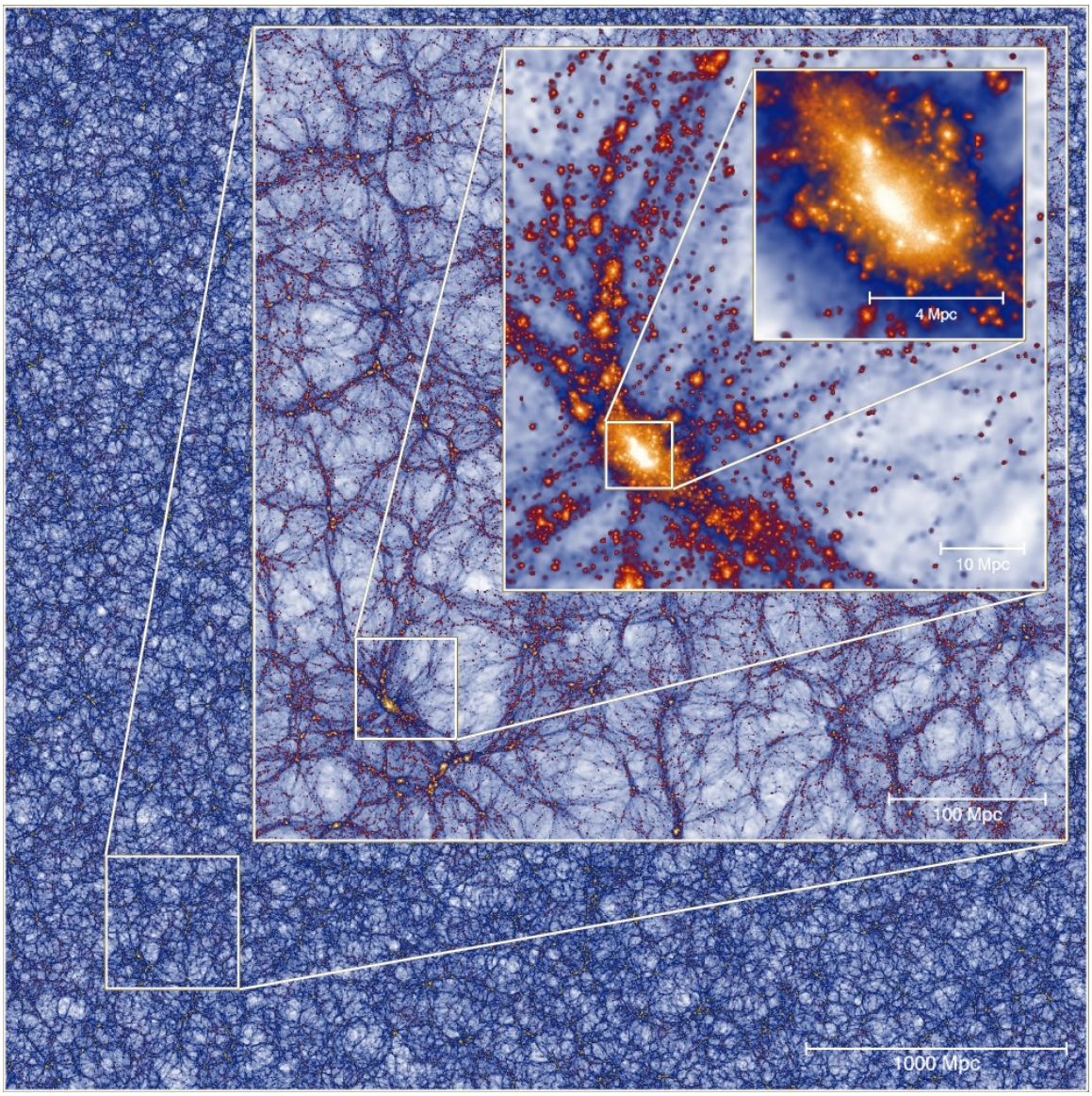

Figure 1.1: The cosmic web as shown by the Millennium XXL simulation (Angulo et al., 2012). The image shows the dark matter density of a slice of the simulation that is 8 Mpc thick.

in the dark blue areas, and highest in the yellow areas. The spongy structure seen in the most zoomed-out layer is made up of pancakes and filaments surrounding voids, largely empty regions of space. In the more zoomed-in views, halos are visible as small, discrete, high-density lumps of dark matter. The most zoomed-in view shows the largest cluster in their simulation. Note the presence of substructure within the halo. The bound sections of substructure are called "subhalos" and may continue to orbit the central halo, may have material stripped off them, or may eventually merge with the central halo.

1.2 Galaxy processes

We observe many processes that contribute to the formation and evolution of galaxies, but their interplay and relative importance are not always clear. The main components of a galaxy are the dark matter halo, the stars, the gas, and the central supermassive black hole (SMBH). In Section 1.1, we discussed the formation of dark matter halos and in this section, we will discuss the behavior of the galaxy within the halo.[1] Galaxies form when gas in a halo cools and settles to the center of the halo. When it gets sufficiently cool and dense, the gas can form stars. Supernovae and active galactic nuclei drive winds and can prevent further star formation. In general, galaxies tend to be either velocity dispersion-supported elliptical galaxies that are

[1]If gas outside of a halo were to get dense enough, the gas could theoretically form a galaxy anyway, but the source of such a gas-only over-density is not obvious. The over-densities in dark matter and baryonic matter in the early universe are thought to occur in the same places.

red and not star-forming or rotation-supported disk galaxies that are blue and star-forming, though irregular or intermediate types of galaxies exist. (Silk & Mamon, 2012; Somerville & Davé, 2015)

When halos first collapse, they bring coincident gas with them. Broadly speaking, gas tends to be hot and diffuse or cold and dense. Cold gas is generally thought to be confined to the disk of the galaxy. Hot gas can be found in regions of the disk or also as a hot gas halo around the galaxy. Recent COS-Halos results show a significant quantity of gas out to 150 kpc (Tumlinson et al., 2011, 2013), enriched with elements not present in pristine, unprocessed gas. This suggests that at least some of the gas in the hot halo was processed in the galaxy and subsequently expelled in galactic winds (Peeples et al., 2014). Gas cools radiatively when electrons are forced into excited states by collisions and subsequently decay, emitting a photon. If photons emitted this way can escape the gas, they carry away some of the gas' energy. Star formation occurs in the coldest, densest regions of gas in self-shielded clouds of molecular hydrogen. In these dense clouds, the gas can fragment into small enough segments to form individual stars.

Once stars have formed, they heat the gas around them radiatively and via core-collapse supernovae. Massive stars are much bluer than low-mass stars, end their lives in supernovae, and are quite short-lived, so they provide the most ionizing radiation and the most immediate and dramatic feedback. Core-collapse supernovae from these massive stars inject kinetic energy or momentum as well as heat into the surrounding

medium and likely drive galactic outflows, pushing gas out of the disk or even out of the halo entirely. Once enough of the gas in a star forming region has been heated sufficiently, star formation stops because the gas can no longer fragment and collapse. The heating of gas near young stars by stellar radiation and supernovae are called stellar (or radiative) feedback and supernova feedback, respectively.[2] The gas heated by feedback may eventually cool and settle back into the disk, becoming available for star formation again.

A large factor in galaxies' star formation histories is the availability of gas to form into stars. Gas moves between the cold gas disk and the hot halo, but new gas also accretes onto the galaxy. Some of this accretion is pristine gas from the intergalactic medium or processed gas that was ejected and then reaccreted. Some is associated with smaller galaxies that merge and bring their own gas with them. Generally, one galaxy in a merger is significantly less massive than the other. The smaller galaxy either has material stripped from its outskirts or is completely destroyed and incorporated into the larger. Very massive galaxies seem to have either expelled or heated enough of their gas to effectively halt star formation, a process called quenching. (Conselice, 2012; Silk & Mamon, 2012)

Most galaxies are thought to contain a supermassive black hole at their center. We expect black holes at the centers of galaxies because massive stars leave behind black holes as remnants, which will migrate to the center of the galaxy due to dynamical

[2] "Stellar feedback" is also sometimes used to refer to radiative and supernova feedback together.

friction. Black hole masses predicted for this process are significantly lower than the observed masses, perhaps $10^4 M_\odot$ rather than $10^6 - 10^{10} M_\odot$ as observed (Greene, 2012). The general solution to this problem is to posit some sort of massive seed black hole, but the source of such an object is debated (Greene, 2012; Kormendy & Ho, 2013). Evidence for supermassive black holes comes from stellar velocities, reverberation mapping, megamasers, x-rays, velocity maps (Kormendy & Ho, 2013, and references therein), and most recently, gravitational waves from LIGO (Abbott et al., 2016). These supermassive black holes power active galactic nuclei (AGN), which are extremely energetic sources sometimes found at the centers of galaxies. Supermassive black holes become AGN when material falls onto them, spiraling down to the black hole in an accretion disk. AGN can also heat the gas in a galaxy and drive outflows, possibly significant enough to quench star formation in the galaxy.

1.3 Observing galaxy properties

All of the information that we have about galaxies can be boiled down to light and location: we know the number and wavelengths of the photons received from a galaxy and we know the direction from which we received those photons. The closer a galaxy is to us, the better we can resolve it. At high redshifts, most of our insight into galaxy properties comes from a galaxy's spectral energy distribution (SED), the distribution of energy received at different wavelengths. A galaxy's SED is determined by the

stellar spectra plus absorption and emission from gas and dust. Stellar spectra are determined by the stars' masses, metallicities, and ages. Absorption and emission by dust and gas depend on the amount of material and properties such as density, temperature, and composition. Because all of these things go into determining the galaxy's SED, the SED contains information about the stellar mass of the galaxy, the ages of the stars, the amount of gas and dust between the stars and us, and the composition of the gas.

The standard method of extracting information from SEDs is to construct a library of template galaxy SEDs with different masses, metallicities, and star formation histories and then to fit an observed SED with the templates at various redshifts. The templates are constructed by adding together all the spectra of the stars expected to be in the galaxy based on the star formation history. Getting the spectra of the stars requires models for stellar evolutionary tracks and either stellar atmosphere models or libraries of observed stellar spectra. The template galaxy's SED also generally includes a model for dust absorption, scattering, and nebular emission lines. A major uncertainty in SED template generation is the stellar initial mass function (IMF), the number of stars of a certain mass formed per unit star formation. We have estimates of the local initial mass function from nearby star forming regions, but the universal stellar IMF, and even if such a thing exists, remains uncertain. All SED fitting methods assume a stellar IMF, so the systematic uncertainty on the IMF propagates to stellar masses from SED fitting.

Once the library of templates is created, the template SEDs are redshifted and compared to the observed SED in question. The redshift used for the best fit SED is the photometric redshift and the template galaxy properties are estimates of the properties of the galaxy. The most reliable galaxy property from SED fitting is the redshift, followed by the total stellar mass of the galaxy and then the star formation rate. The galaxy's age and metallicity are degenerate, so SED ages and metallicities should be used with caution.

Mobasher et al. (2015) study in detail the accuracy of a number of SED fitting codes at reproducing the properties of simulated galaxies and the consistency between codes on observed galaxies. They find that stellar masses are accurate to about a factor of two. The errors on masses and ages are related, which makes sense: low mass stars are long-lived and contribute most of the stellar mass but not a significant fraction of the galaxy's luminosity. An assumed large population of old, low-mass stars could bias ages and masses higher.

In principle, galaxies' gravitational masses can be measured from rotation curves and velocity dispersions. These velocity measures provide constraints on the gravitational mass contained within the radii measured. At high redshift, this method is impractical due to lack of resolution and galaxies' faintness. Where it can be applied, the measurements are usually of the central regions of the galaxy, where the mass is predominantly baryonic. These measurements can also be thrown off by galaxy winds or mergers.

1.4 Trends in galaxy properties

Many galaxy properties are interrelated. These dependences often provide insight into how galaxies form and evolve. In this section, we discuss some of the main galaxy property relations that will be important to this work.

1.4.1 Stellar and halo masses

One of the most basic galaxy properties is the dependence of number density on mass or luminosity. A mass or luminosity function is defined as the volume number density of galaxies per unit mass or luminosity. Essentially, it's a histogram of masses or luminosities with the survey volume and bin widths factored out for universality. We will mainly be dealing with the galaxy stellar mass function (SMF) and halo mass function (HMF). Stellar mass functions have been measured by a multitude of groups (e.g. Baldry et al., 2008; Marchesini et al., 2009; Baldry et al., 2012; Santini et al., 2012; Moustakas et al., 2013; Tomczak et al., 2014; Duncan et al., 2014; Mortlock et al., 2015). Halo mass functions are predicted from simulation and also from analytic theories such as Press-Schechter (Binney & Tremaine, 2008).

Estimates of the stellar mass function over redshifts $0.3 < z < 3$ from Mortlock et al. (2015) are shown in Figure 1.2. Note that higher mass galaxies are to the left on the x axis. What these stellar mass functions reveal is that at all redshifts, low mass galaxies are more abundant than high mass galaxies. At high masses, abundances

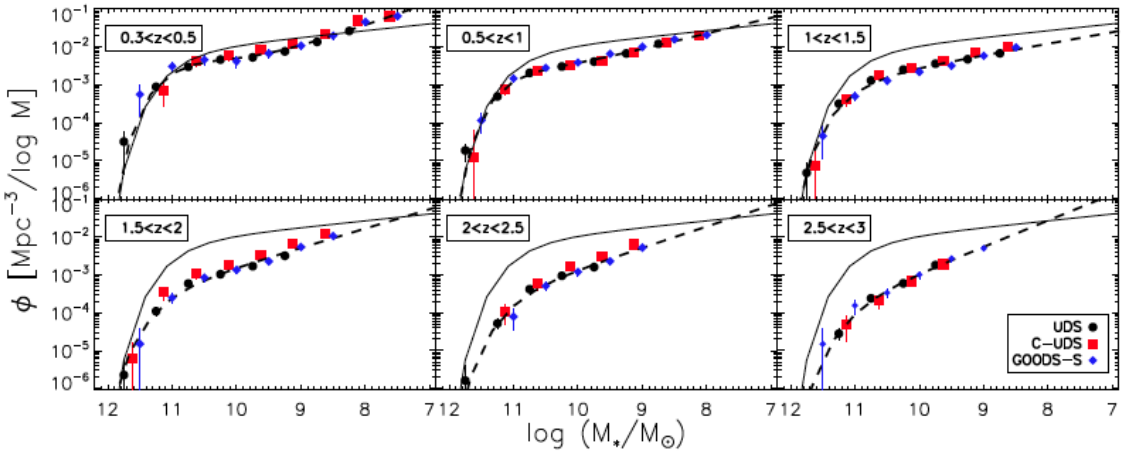

Figure 1.2: Stellar mass functions from Figure 5 of Mortlock et al. (2015). Black circles show the SMF for the entire UDS survey, the red squares are the SMF for the CANDELS UDS field, and the blue diamonds are the SMF for GOODS-S. The dashed lines are Schechter function fits to the SMFs and the solid line in each panel shows the redshift $z = 0$ relation from Cole et al. (2001) converted to a Chabrier initial mass function.

drop off drastically. There is a definite evolution of the stellar mass function over different redshifts: at early times, galaxies were less abundant in general and the shape of the stellar mass function is flatter. Stellar mass functions are generally fit with either a single Schechter function (Schechter, 1976) or a double Schechter function and the exact values of the fit parameters are not entirely agreed upon between studies (Duncan et al., 2014). However, the qualitative shape is the same: a power law slope at the low-mass end, perhaps with a turn-up at the lowest masses and redshifts, and an exponential cutoff at high masses.

Halo mass functions (HMFs) are often obtained from dark matter simulations. Halo detection in simulations can be tricky, particularly when accounting for substructure or during major mergers. Generally, halo finders use some subset of the

position, velocity, and temporal information to group simulated dark matter particles into halos. They apply some algorithm on the dark matter particles to divide them into discrete, bound structures, then create a catalog of halos and their properties. These algorithms range from simple, like the spherical over-density technique used in Tinker et al. (2010), to complex, incorporating velocity information and requiring consistency between time steps (e.g. Behroozi et al., 2013b). Behroozi et al. (2013c) compare five halo finder codes in the specific case of major mergers, one of the more difficult problems for halo finders. They find that position-only algorithms can accurately track halo positions and velocities, but are inconsistent with mass determination and satellite/central assignment. Finders that use velocity information are better at tracking masses, but still have difficulty in the final merger stages. Finally, those that use position, velocity, and temporal information produce the best results but still may have trouble with consistency at the final merger stages.

The halo mass function used in Moster et al. (2010) is shown in Figure 1.3.[3] The halo mass function, the dashed line in the figure, is a different shape than the galaxy stellar mass function. If the halo and stellar mass functions were the same shape, it would imply that all halo masses were equally efficient at turning gas into stars. The fact that they are not the same shape suggests more complicated galaxy physics. The departure of the stellar mass function from the halo mass function at low masses is

[3]Moster et al. (2010) use halos from an N-body simulation run with WMAP3 cosmology, $\Omega_m = 0.26$, $\Omega_\Lambda = 0.74$, $h = H_0/(100\text{km s}^{-1}\text{ Mpc}^{-1}) = 0.72$, $\sigma_8 = 0.77$, and $n = 0.95$. This differs from Planck cosmology somewhat, but the differences don't affect the shape of the halo mass function significantly.

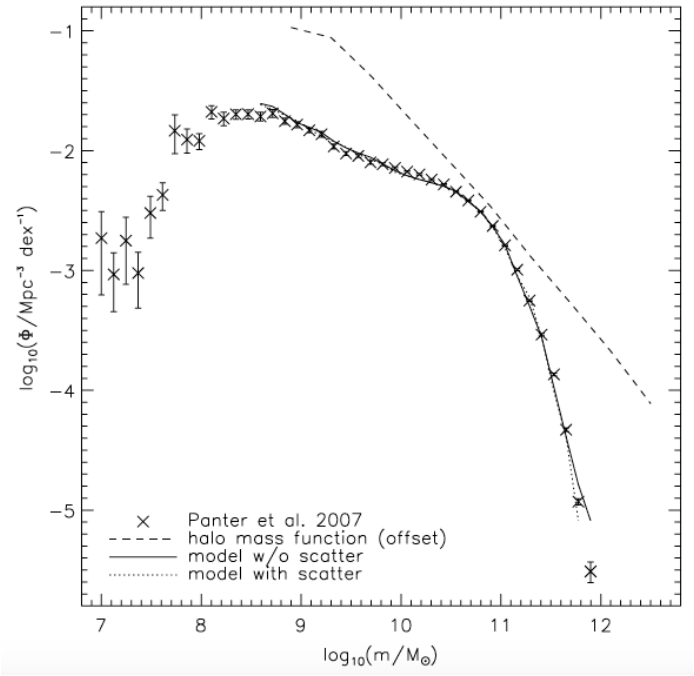

Figure 1.3: Stellar and halo mass functions from Moster et al. (2010). The halo mass function is shown as the dashed line. Stellar mass function data from Panter et al. (2007) is shown as crosses and the Moster et al. (2010) abundance matching results are shown as the solid and dotted lines. The halo mass function has been offset by a factor of 0.05 to bring it to the stellar mass function.

attributed to supernova feedback and the departure at high masses is attributed to AGN feedback.

To investigate the star formation efficiency of different mass halos, we need to know both the stellar and halo masses of galaxies. This presents a challenge due to the difficulty of measuring dark matter masses. Abundance matching is a class of empirical models that match stellar masses to halo masses by number density (see Section 1.5.1 for more details). The stellar mass as a function of halo mass, $M_\star\,(M_{\rm halo})$, gives us a sense of how efficient halos of a certain mass are at turning their gas into stars.

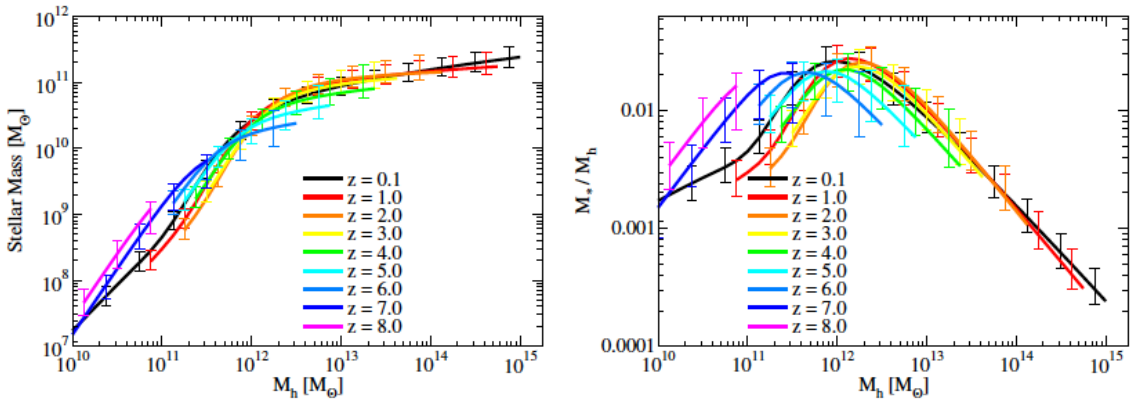

Figure 1.4: Figure 7 from Behroozi et al. (2013a), who use a subhalo abundance matching routine with a large ensemble of stellar mass function estimates to determine $M_\star\,(M_{\rm halo})$, shown on the left, and $f_\star\,(M_{\rm halo})$, shown on the right. The colors of the curves indicate the redshifts.

The left panel of Figure 1.4 shows the $M_\star\,(M_{\rm halo})$ relation from redshift $z = 0.1$ to $z = 8$ and the right panel shows $f_\star\,(M_{\rm halo})$= $M_\star/M_{\rm halo}$, the ratio of stellar mass to halo mass. Halos are thought to start with approximately the same fractional amount of gas $M_{\rm gas}/M_{\rm halo}$: the universal baryon fraction, $\Omega_{\rm baryon}/\Omega_{\rm DM} \approx 0.19$ for Planck cosmology. If all halos were equally efficient at converting their allotment of gas to stars, the $M_\star\,(M_{\rm halo})$ relation would be linear and the $f_\star\,(M_{\rm halo})$ relation would be flat. Instead, halos with $10^{11} < M_{\rm halo} < 10^{12}\ M_\odot$ are more efficient at forming their gas to stars with star formation efficiency falling both to higher and lower masses. Naive galaxy formation models tend to have star formation efficiencies that are approximately constant with halo mass (Somerville et al., 2008b). To match the shape of the $M_\star\,(M_{\rm halo})$ relation, galaxy formation models invoke supernova feedback at low halo masses and AGN feedback at high halo masses.

1.4.2 Clustering

Galaxies are not distributed evenly throughout the universe; they follow large-scale dark matter structure. Figure 1.5 shows nearby galaxies from the Sloan Digital Sky Survey and the galaxy distribution is highly reminiscent of the dark matter structure in Figure 1.1. Correlation functions are a statistical tool that quantify how clustered a population is. Clustering is scale-dependent: one could imagine a set of small, high-density clumps of objects distributed randomly, which would be highly clustered on very small scales but completely unclustered on large scales. Correlation functions work with the set of separations between all possible pairs of objects, comparing the population of interest to a randomly distributed sample. Galaxies tend to be more clustered on small scales and unclustered on the largest scales. The lack of clustering at large scales is synonymous with the statement that the universe is homogeneous and isotropic on large enough scales.

Galaxy clustering is a function of galaxy properties, which provides useful information about how galaxy properties depend on environment. For instance, red galaxies tend to be more clustered than blue galaxies, suggesting that star formation prefers less dense environments. Brighter and more massive galaxies also tend to be more clustered. (e.g. Zehavi et al., 2002; Coil et al., 2008; Zehavi et al., 2011; Coil, 2013; Barone-Nugent et al., 2014) Galaxies of a given mass tend to be more clustered at higher redshifts because the same mass halo represents a rarer over-density at higher

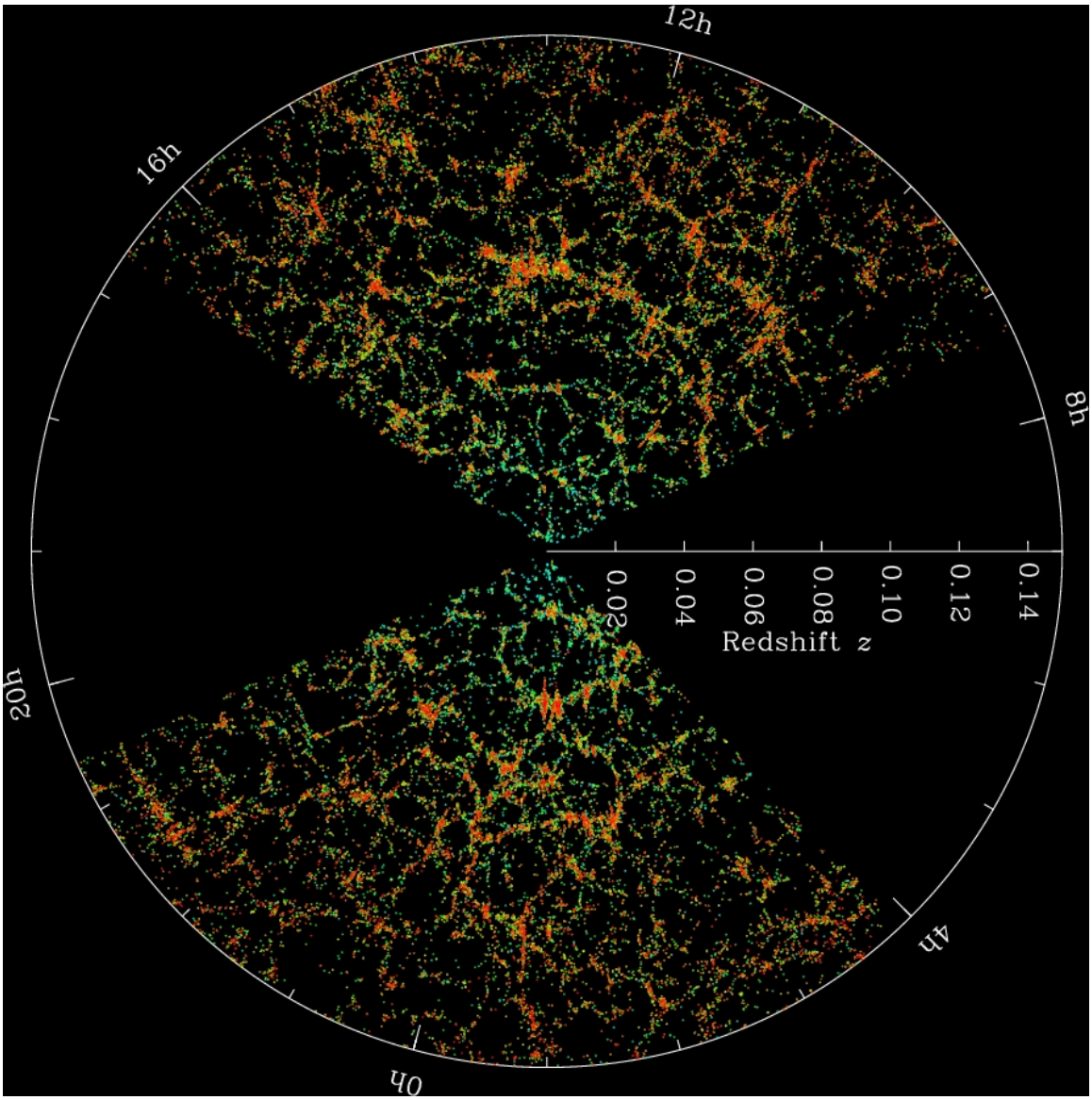

Figure 1.5: Galaxies in a slice of the Sloan Digital Sky Survey (SDSS). Each dot in the image is a galaxy. (Image courtesy of www.sdss.org/)

redshifts.[4]

Galaxy conformity, the tendency of blue galaxies to have blue neighbors and red galaxies to have red neighbors, is a fairly recent discovery in clustering (Weinmann et al., 2006). There is conformity between satellites and centrals–centrals and satellites tend to be the same color (Weinmann et al., 2006; Hartley et al., 2015)–but this tendency also persists significantly beyond the virial radii of halos, out to 1-5 Mpc (Kauffmann et al., 2013). Galaxy processes do not extend to these large radii, suggesting that halo assembly history plays a role in determining galaxy color (Hearin et al., 2015).

Correlation functions are often used as a way to determine the average halo mass of a galaxy population. They can be used to estimate a population's bias, a clustering metric. Bias measurements are defined with respect to some baseline and the standard baseline for halos is a linear extrapolation of the primordial density fluctuations. The halo bias defined thus is directly related to halo mass, with higher mass halos having higher bias. We can determine the bias to halo mass relation, $b\,(M_{\rm halo})$, from simulations and use it to estimate typical halo masses of galaxy populations with measured biases. Doing this requires a model of how galaxies populate halos, either assuming that galaxies are unbiased tracers of halos or using a more sophisticated model, such as a halo occupation distribution (see Section 1.5.2). This is often done

[4]In order to form a massive galaxy at high redshift, the halo must have formed from a peak many standard deviations from the average density. By definition, peaks many standard deviations from average are rare. The higher the mass of the halo and the higher the redshift, the rarer the over-densities required to form them.

with Lyman Break Galaxies (LBGs) at high redshift, generally finding a halo mass of around $10^{10.5} - 10^{11.5} M_{\odot}$ (e.g. Lee et al., 2006; Barone-Nugent et al., 2014; Harikane et al., 2015)

Correlation function measurements can either be performed in two dimensions, characterizing the distribution of projected angular separations, or in three dimensions, characterizing the real-space separations. Real-space correlation functions are preferred because they avoid projections effects but are more difficult to measure. Precise distance measurements to astronomical objects are costly and can only be obtained efficiently for large samples at low redshifts: photometric redshift errors at high redshift are too large (e.g. Shepherd et al., 1997; Hawkins et al., 2003; Coil et al., 2008; de la Torre et al., 2013). At higher redshifts, accurate distances are too expensive to measure on large samples, so Lyman break criteria or photometric redshifts are used instead to select a slice in redshift for angular correlation function calculations (e.g. Lee et al., 2006; Barone-Nugent et al., 2014; Harikane et al., 2015). Completeness is also a concern for high-redshift correlation functions: high-redshift objects are faint and difficult to detect.

1.5 Galaxy models

All of the galaxy processes discussed in Section 1.2, such as supernova and AGN feedback, are certainly present in galaxies but their relative importance in shaping

galaxy properties and the ways in which the processes interact are less clear. Empirical models of galaxy formation start from the end result, observed galaxy properties, and try to reconstruct what must have happened to produce the observations. An alternative approach is to start from known physics, set up realistic initial conditions, and see what sort of galaxies are formed in the simulated universe. Abundance matching and halo occupation distributions are examples of the first, while semi-analytic and hydrodynamic models are examples of the second.

1.5.1 Abundance matching

Abundance matching is a class of empirical model that starts from the halo and stellar mass functions. In the simplest implementation of abundance matching, the most massive/rarest halos are matched with the most massive/rarest galaxies. Then the next most massive halos are matched with the next most massive galaxies and so forth down to the lowest mass galaxies. More sophisticated abundance matching models can also treat scatter in the relations or differences between central halos and subhalos, which are subject to somewhat different processes. Subhalos may have some of their dark matter or baryonic mass stripped from them and added to the main halo's mass. They may even be completely destroyed and merge with the central halo and galaxy. The handling of subhalos may require more sophisticated machinery than the simplest "most massive halo gets the most massive galaxy" mechanic (Behroozi et al., 2013a).

Abundance matching may also be constrained by more than just the halo and stellar mass functions. Our knowledge of dark matter evolution allows us to trace a galaxy's star formation history in an abundance matching model if the abundance matching is performed at multiple epochs. In this case, the model can use observations of star formation rates as a constraint. Models fit thus can reproduce galaxy stellar mass functions, star formation rates, and star formation histories (Behroozi et al., 2013a). Guo et al. (2016) test the success of subhalo abundance matching in reproducing clustering measures and find that it matches acceptably well at high luminosities. Their SHAM procedure applies the same galaxy-halo mass relation to subhalos and centrals by default. This assumption leads to incorrect small-scale clustering for low luminosity galaxies. Allowing subhalos and centrals to follow different galaxy-halo mass relations corrects this tendency, though low mass centrals end up with more satellites than observed. Guo et al. (2016) note that this is likely due to how satellites populate subhalos as a function of radius: subhalos tend to be located farther from the center than satellite galaxies seem to be.

1.5.2 Halo occupation distributions

Halo occupation distribution models (HODs) are another class of empirical galaxy model. The core of an HOD is the halo occupation, $P(N|M)$, the probability of observing N galaxies in a halo of mass M. HODs are most often used to predict galaxy clustering from our knowledge of dark matter. Generally the true halo occupation is

not known, so a parametric form is adopted and fit to observed clustering statistics. They also require assumptions about the distribution of galaxies within the halos (Berlind & Weinberg, 2002).

While the concept of halo occupation has been around since the 70's, Benson et al. (2000) was among the first to apply it in its current form (Berlind & Weinberg, 2002). Benson et al. (2000) placed galaxies from a semi-analytic model of galaxy formation in halos from an N-body simulation and successfully modeled observed galaxy clustering. Berlind & Weinberg (2002) and Zehavi et al. (2004) examined halo occupation distributions without simulated galaxies, simply predicting the number of galaxies in each halo from the observed clustering measures. van den Bosch et al. (2003) and van den Bosch et al. (2007) used a halo occupation distribution framework paired with a conditional luminosity function ($\Phi(L|M)$) to predict clustering as a function of luminosity and constrain the cosmological model: models fit to WMAP3 cosmology were more accurate than those fit to WMAP1. van den Bosch et al. (2007) predicted that the actual cosmological values of Ω_m and/or σ_8 were somewhere in between the two. The Planck value of Ω_m is 0.31, which is close to the WMAP1 value and the Planck value of σ_8 is 0.82, which is between the WMAP1 value of 0.9 and the WMAP3 value of 0.74 (Planck Collaboration et al., 2015).

Lee et al. (2006) use HOD modeling to examine Lyman Break Galaxies (LBGs) at redshifts $z \sim 4$ and 5, finding that there are about 4 to 5 times as many halos expected in their sample as they observe galaxies. They conclude that the duty cycle

for star formation[5] is less than 100% and that faint LBGs have shorter duty cycles. Lee et al. (2009) examine star formation duty cycles at redshifts $z \sim 4$ and 5 in more detail, combining HOD modeling with a conditional UV luminosity function that has duty cycle as a free parameter. They find that the 1σ range for the star formation duty cycle for high redshift LBGs is 15% - 60% for redshift $z = 4$ and <70% for redshift $z = 5$.

Recently, Hearin et al. (2016) presented a framework to extend halo occupation distributions to treat occupation as a function of more than just halo mass. Galaxy conformity suggests that galaxy properties depend on some halo property other than mass, most likely the halo assembly history. If this is the case, then there is little reason to believe that halo occupation would not also be affected by halo assembly history. They find that their decorated HOD can reproduce assembly bias signatures such as galaxy conformity and they make predictions for conformity and lensing signatures as a function of redshift.

Halo occupation distributions are very powerful tools that separate the effects of cosmology from the messy baryonic physics. The baryonic physics are distilled into a single quantity, the halo occupation number, and then placed into halos whose properties are entirely determined by the cosmological model. Any model that seeks to reproduce galaxy properties from first principles must also replicate the halo occupation distribution in order to correctly reproduce galaxy clustering observations.

[5] "Duty cycle" is defined as the percentage of time that a galaxy is "on," i.e. forming stars and therefore bright in the UV. This is equivalent to the fraction of galaxies forming stars at any one time.

1.5.3 Semi-analytic models

Semi-analytic models are essentially a system of differential equations ("recipes") that dictate how mass moves between different reservoirs in a galaxy. These recipes are integrated over dark matter histories generated from theory or N-body simulations to produce bulk galaxy properties. Galaxies in semi-analytic models are represented by reservoirs of mass such as a dark matter halo, a stellar disk, a stellar bulge, a cold gas disk, and a hot gas halo. The recipes represent processes that move gas from one reservoir to another. For example, star formation moves cold gas in the disk to stellar mass in the disk, supernova feedback moves cold gas in the disk to the hot gas halo or ejects it from the galaxy, and gas cooling moves gas in the hot halo to the cold gas disk.

The dark matter halos that a semi-analytic model takes as input are arranged into merger trees. Merger trees represent the dark matter history of a single halo. They can be constructed either from N-body simulations or from analytic models such as Press-Schechter theory. Either way, the merger tree contains all of the dark matter halos down to a certain threshold that have merged to become a part of the halo of interest. Semi-analytic models don't need any spatial information about the paths that the halos took, just the masses of all the progenitor halos and times at which they merged. Figure 1.6 shows a simple example merger tree from Giocoli et al. (2010). The top of the figure is the initial configuration and time progresses towards the bottom of the figure. The most massive progenitor at each time step is shown in

purple at the left and smaller halos are shown merging in to become subhalos of the larger halos. Subhalos can be destroyed and incorporated into their host halos, such as subhalo a between redshift z_2 and z_1. The merger tree shown allows for subhalos to have subhalos of their own, such as subhalo D with subhalos b and c at redshift z_0. In some SAMs, this is not allowed and b and c would be considered subhalos of the main halo and not associated with D.

The main strength of semi-analytic models is their speed. They can take a large number of physical processes, represented as recipes, and generate billions of galaxies within hours. Because they are so fast, semi-analytic models are often used to tune recipes, adjusting free parameters until the model matches some set of observations. Some of the recipes that semi-analytic models use are similar to those used in hydrodynamic models, which take much longer to run. Semi-analytic models are a good way to inform hydrodynamic models.

Semi-analytic models are generally tuned to match the present-day stellar mass function and sometimes other local relations. In general, SAMs match the broad strokes of galaxy evolution, but miss some of the details. In particular, they have some difficulty with the buildup of stellar mass in galaxies, which shows itself in the stellar mass function, star formation rates, and metallicities. (Lu et al., 2014) These discrepancies are also seen in hydrodynamic models. Note that SAMs don't necessarily contain information about the locations of galaxies on the sky. If this is the case, then clustering must be put in by hand, as with the Benson et al. (2000)

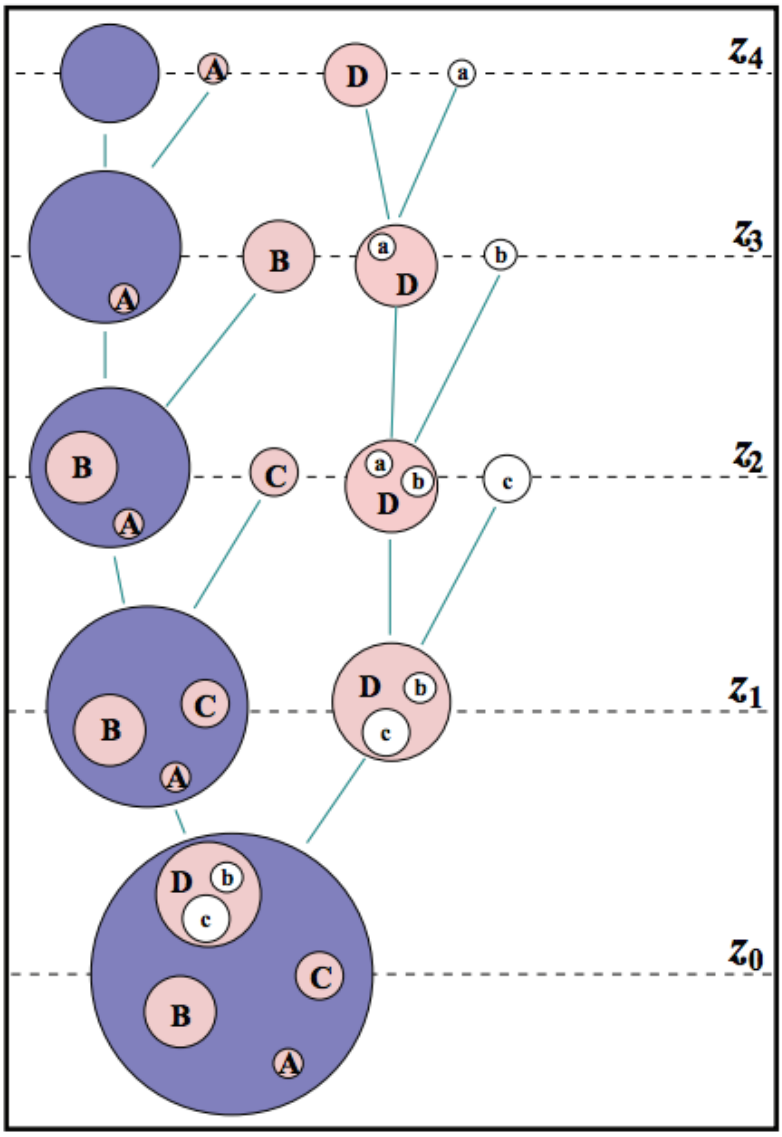

Figure 1.6: Figure 1 of Giocoli et al. (2010). Schematic halo merger tree with the most massive progenitor at each step shown in purple. Minor progenitors are shown in pink and white. Time progresses from the top of the plot to the bottom, moving from the highest redshift, z_4, to the final redshift, z_0.

model. If the SAM is run on an N-body simulation, locations of the centrals and possibly the satellites can be taken from the N-body simulation.

1.5.4 Hydrodynamic models

Hydrodynamic models aim to reproduce galaxy formation from as close to first principles as possible. They include dark matter, stellar matter, and gas and they model gravitational and hydrodynamic forces as well as possible. With our current computing power, hydrodynamic models can't resolve processes on all relevant scales: the Milky Way disk is about 10^5 ly in diameter and individual star formation occurs in regions on the order of 10^{-4} ly (a few AU). Often, hydrodynamic models of cosmological volumes are 10^8 or 10^9 ly on a side. Timescales are also highly variable in addition to the physical scale disparity. Supernovae occur on timescales of tens of days, galaxy rotation periods are hundreds of millions of years, and the Universe is 14 billion years old. Adaptive mesh codes can ameliorate the problems with spatial resolution but not with temporal resolution. There exist treatments that allow for adaptive temporal resolution, but our computing power is still insufficient to resolve all relevant scales.

Since we can't model all the relevant properties in detail, hydrodynamic models include "sub-grid" recipes that regulate unresolved processes such as star formation and supernova feedback, similar to the recipes in semi-analytic models. When certain conditions are met in the gas, usually involving temperature and density, the gas

forms stars at a prescribed rate. Feedback processes are modeled by adding energy or momentum to the appropriate section of the gas.

Hydrodynamic models are more useful than semi-analytic models when it comes to testing some details of a theory. Galaxies in semi-analytic models must be simple. Cold gas is always arranged in a thin disk, stars are either arranged in an exponential disk or a bulge, and all of the components have very restricted interactions and spatial arrangement. In hydrodynamic models, this is not the case. Galaxies can be irregular, have spiral structure, merge in a realistic way, have clumpy star formation, etc. All of these departures from the assumed distributions and mechanics of semi-analytic models test the galaxy formation model in a way that semi-analytics cannot. Qualitatively, hydrodynamic models do well in reproducing galaxy appearances at redshift $z = 0$. Not much quantitative study has been done on modeled galaxy morphology, largely due to the lack of metrics applicable to both observations and simulations (Somerville & Davé, 2015).

Hydrodynamic models perform similarly to semi-analytic models in reproducing the overall trends of galaxy properties. They have difficulty with the details of stellar mass buildup in the same way and at about the same level as SAMs. They also tend to have difficulty reproducing the observed clumpiness of disks at intermediate redshifts: excessive star formation is prevented by gas pressurization, but the pressure must be decreased in order to form clumps. This means that sufficiently clumpy galaxies tend to be too efficient at forming stars. (Somerville & Davé, 2015)

1.6 The problem

Currently, semi-analytic and hydrodynamic models fail to reproduce our best estimates of galaxies' observed star formation histories. Compared to abundance matching results, low mass halos form their stars too early and high mass halos form their stars too late. Abundance matching results may not be completely reliable: abundance matching is a fairly simple process and requires assumptions about how galaxies populate halos that may not reflect all the complexity introduced by galaxy formation processes. The problem remains even disregarding results from abundance matching, however. At redshift $z = 0$, modeled low mass galaxies have star formation rates that are lower than observed and colors that are too red. In addition, while the modeled redshift $z = 0$ stellar mass function matches observations, higher redshift stellar mass functions do not. At the heart of all three is galaxies' buildup of stellar mass over time.

How a galaxy builds up its stellar mass depends on star formation rates, feedback, and all of the processes that regulate gas availability. This is a complicated system of highly interdependent processes, so it is not unreasonable to think that we may not be modeling it properly. However, the most directly useful observed relation is $M_\star\left(M_{\rm halo}\right)$ as a function of redshift, which is very difficult to observe directly due to the difficulty in measuring halo masses. The two aspects of this problem are accurately measuring the $M_\star\left(M_{\rm halo}\right)$ relation and matching it with models. We work first with the models to match abundance matching results, then we use clustering

measurements in the CANDELS survey to constrain the observed $M_\star\,(M_{\rm halo})$ relation.

1.6.1 Modeling problems

The evolution of the stellar mass function (see Section 1.4.1) is an essential galaxy observation that models aim to reproduce. Most models are tuned to match the redshift $z = 0$ stellar mass function and in general do not match at higher redshifts. Both hydrodynamic and semi-analytic models tend to build up stellar mass in low mass halos too early and in high mass halos too late. Recasting the problem in terms of halos' star formation histories is useful to understand the physical processes that drive the evolution of the stellar mass function. These star formation histories can be teased out of abundance matching, along with the $M_\star\,(M_{\rm halo})$ relation.

High mass galaxies formed the bulk of their stars over ten billion years ago, as evidenced by galaxy colors, SED fitting results, and abundance matching. Low mass galaxies are still actively forming stars, although the epoch of peak star formation in the universe happened at redshift $z \approx 2$. Most galaxy formation models regulate star formation through availability of cold gas: as soon as cold gas is available, it forms stars. Lack of cold gas is the only way modeled galaxies will stop forming stars. Gas accretion onto halos tends to mirror the accretion of dark matter, so the star formation history of modeled galaxies tends to mirror the halo assembly history. Observed star formation does not have the same shape as the halo assembly history. Low mass halos accrete their halo mass, and therefore gas, earlier than they form their

stars, meaning that something must prevent stars from forming from the accreted gas.

The current method for preventing star formation from gas in low mass galaxies is to increase the star formation feedback. This decreases the overall efficiency of star formation but acts in the same way at all redshifts; it does not change the shape of the star formation history, only the normalization. The question is then what process could prevent star formation at high redshifts while allowing it to proceed at lower redshifts. The physical options available roughly fall into three categories: (1) cold gas is present in the galaxy but star formation feedback is more efficient at higher redshifts, so small amounts of star formation are capable of shutting off further star formation until the gas cools again, (2) cold gas is present and feedback is the same, but star formation itself is less efficient at higher redshifts, or (3) cold gas can't fall into the halo at higher redshifts and is thus unavailable for star formation until lower redshifts.

In Chapter 2, we examine the effectiveness of these three paradigms with the Santa Cruz semi-analytic model (Somerville et al., 2008b, 2012) by introducing ad hoc recipes to produce the physical effect desired. In our preferential reheating model, we introduce a redshift dependence to the supernova feedback recipe. In the direct suppression model, we let the star formation law vary with redshift. In the parking lot model, we trap gas in a reservoir outside the galaxy until lower redshifts.

1.6.2 Observational problems

Since dark matter halos are difficult to observe on their own, abundance matching is our main source for measurements of the $M_\star\,(M_{\rm halo})$ relation. More direct measurements exist, but are more difficult to obtain. Gravitational lensing is one of the best ways to measure halo masses, but occurrences are too rare and measurements are too time-consuming to use on a statistical sample. Rotation curves of spiral galaxies only measure the mass inside the outermost measurable orbit and halos extend far beyond the size of the disk, even at low redshifts where we can measure galaxy outskirts. Galaxy correlation functions provide a statistical way to measure halo masses for galaxy populations. Correlation function mass measurements require a model for how galaxies populate halos, but are more direct than abundance matching (see Section 1.4.2).

There are several ways to determine the bias of a galaxy sample from correlation functions. One commonly used option is to fit a power law to the correlation function and use an analytic formula to convert the power law fit to a bias. This method assumes that the bias is not a function of scale, which should be true at large separations. Another option is to divide the galaxy correlation function by the baseline correlation function extrapolated from the primordial density fluctuations. This allows for a scale-dependent bias and shows the excess bias at small separations but converges to a single value at large scales. The large scale value is the galaxy bias in this method. In either of these methods, the galaxy bias can be converted directly

to a halo mass if the galaxy bias is assumed to be the same as the halo bias. If the two are not the same, a more complicated halo occupation model is required. These two approaches should yield the same results if only the large scale, linear regime is measured.

An alternative to calculating the bias from the observations is to use forward modeling, which brings the theory closer to the observations instead of the other way around. Forward modeling predicts the correlation function of galaxies based on an assumed halo mass range and a way in which galaxies populate halos. An array of such correlation functions are generated, then compared to the observations. The halo mass of the closest match is taken to be the halo mass of the observed sample. Halo occupation distributions are very convenient for this application as well.

In this work, we focus on calculating the halo mass from a power law fit to the correlation function. In the literature, this is often the default mass estimation from correlation functions, since it is the least model-dependent. This method has not been analyzed in detail to check accuracy. In Chapter 3, we discuss the details of calculating the correlation function. In Chapter 4, we discuss the conversion from correlation functions to halo mass using simulations. We use the techniques tested to measure the $M_\star\,(M_{\rm halo})$ relation in the CANDELS fields.

Chapter 2

Matching $M_\star\,(M_{\rm halo})$ with semi-analytic models

2.1 Introduction

Semi-analytic models (SAMs) of galaxy formation are simulations that take dark matter halo histories and use simple recipes to paste the behavior of baryonic matter on top. The recipes they use are simple analytic formulae that describe physical processes like star formation, feedback, and gas cooling. Since they do not actually try to solve for the complicated hydrodynamic processes that baryons follow on small scales, SAMs are ideal for exploring the parameter space of recipes that full hydrodynamic simulations use for their sub-grid recipes. Their speed also makes them ideal candidates for exploring the effects of different recipes or physical processes.

In this section, we use physically motivated ad hoc recipes to try to reproduce the observed build-up of stellar mass in low mass halos ($M_{\rm halo} \lesssim 10^{11}\ M_\odot$). This work was published as White et al. (2015).

2.1.1 The Problem

Both hydrodynamic and semi-analytic models have difficulty reproducing the properties of galaxies in low mass halos (virial mass $M_{\rm H} \lesssim 10^{11}\ M_\odot$). Simulated low mass galaxies tend to form stars too early and too efficiently, producing a population of low mass galaxies at redshift $z = 0$ with redder colors, lower star formation rates, and older stellar population ages than are observed (Fontanot et al., 2009). Star formation histories for these galaxies peak too early, resulting in an excess of low mass galaxies ($10^9\ M_\odot \lesssim M_\star \lesssim 10^{10}\ M_\odot$) at $z > 0$ (Weinmann et al., 2012). In addition, observed star forming galaxies tend to have decreasing specific star formation rates (sSFR; $\dot{M}_\star/M_\star$) with increasing mass, a trend that is not reproduced in the models: the models produce constant sSFRs over a large range of stellar mass or even show higher sSFRs at higher stellar mass. These are all symptoms of the same fundamental problem: in the models, gas accretion closely follows dark matter accretion and star formation follows gas accretion. The net result is that star formation histories mirror dark matter accretion histories, which are nearly self-similar for different halo masses in ΛCDM cosmology. Something must break the self-similarity between accretion rate and star formation rate for models to reproduce low mass galaxies' observed star

formation histories (Conroy & Wechsler, 2009; Behroozi et al., 2010; Moster et al., 2013; Behroozi et al., 2013a).[1]

Nearly all current models of galaxy formation set within the ΛCDM framework rely on qualitatively similar recipes for unresolved sub-grid processes. First, powerful outflows driven by massive stars and supernovae ("stellar-driven winds"), are assumed to efficiently heat and eject cold gas from the interstellar medium (ISM) of galaxies. Outflows must be more efficient in lower mass galaxies, ejecting more gas per unit star formation, in order to match the observed slope of the $z \sim 0$ stellar mass function and the observed mass-metallicity relation. Matching high gas fractions at redshift $z = 0$ requires lower efficiency star formation in low mass galaxies, which is usually achieved by imposing a minimum gas surface density threshold below which star formation does not occur. A second consequence of the adopted sub-grid recipes is that star formation in low mass halos is strongly self-regulated, meaning that modifying the star formation and stellar feedback in the models can have a smaller impact than anticipated on many observables: lower efficiency star formation leads to less stellar feedback, leading to more cold gas available and therefore more star formation (Davé et al., 2011; Haas et al., 2013).

[1] Although we are focusing on low mass galaxies, it is worth noting that high mass galaxies show the same sort of "breaking" of the self-similar scaling governed by the halo mass accretion histories but in the opposite sense in time: massive galaxies' stellar masses apparently grow more slowly than their halos at late times. This trend has been more successfully reproduced by models that implement feedback from Active Galactic Nuclei (AGN).

2.1.2 Previous work

Several previous modelers have attempted to address these problems. For instance, Krumholz & Dekel (2012) implemented a metallicity-dependent star formation efficiency in an analytic toy model. In their model, stars can form only in molecular gas (H_2) and the formation efficiency of molecular gas depends on metallicity. They suggested that this would delay star formation in low mass galaxies since it would take time for sufficient metals to build up to provide efficient formation of H_2 and stars. However, they did not actually show that their model quantitatively reproduces galaxy stellar mass functions at low and high redshift. In another toy model, Bouché et al. (2010) cut off accretion for halo masses $M_{\rm H} < 10^{11}\ M_\odot$ and successfully match the slope of the star forming sequence and the Tully-Fisher relation. However, the accretion floor means halos with $M_{\rm H} < 10^{11}\ M_\odot$ will have no stars at all, which is inconsistent with observations of nearby dwarf galaxies.

Henriques et al. (2013, H13) attempted to solve the problems with the redshift evolution of the stellar mass function and luminosity function by altering the timescale for re-accretion of previously ejected gas. They found that changing the ejecta reincorporation timescale and retuning parameters controlling star formation and gas handling could match observed B- and K-band luminosity functions and the stellar mass function over redshifts $0 \leq z \leq 3$ while no retuning of their standard model could. In their altered model, ejecta reincorporation timescales are inversely proportional to halo mass but independent of redshift. In their standard model, the

timescale is inversely proportional to halo dynamical time, which is a fairly strong function of redshift but independent of halo mass. In addition, they showed that their model predictions agree with the $M_\star\,(M_{\rm halo})$ relation derived from abundance matching by Moster et al. (2013) over the same redshift range and produced higher sSFRs and younger ages for galaxies with $M_* \simeq 10^9 - 10^{9.5}\ M_\odot$, in better agreement with observations. Although H13 point out that the form of the reincorporation timescale that they adopt is similar to that found in some hydrodynamic simulations (e.g. Oppenheimer et al., 2010), recent hydrodynamic simulations that implement similar recipes for stellar winds still overproduce low mass galaxies at intermediate redshifts (Weinmann et al., 2012; Torrey et al., 2013).

2.1.3 The goal of this project

In general, any solution to the problems in modeled dwarf galaxies must suppress star formation preferentially at higher redshift and lower halo masses. In this chapter, we explore three different physical scenarios that seem promising for solving the problems with low mass galaxies. We alter (1) the scaling of the mass-loading factor for stellar-driven winds, defined as the outflow rate divided by the star formation rate, (2) the timescale for turning cold gas into stars, or (3) the timescale for gas to accrete into dark matter halos. In the present work, we restrict ourselves to modifications of only one of these recipes at a time. Although our scenarios are physically motivated, we adopt a flexible and empirical approach with the aim of identifying general prop-

erties of the necessary scalings, which may provide clues to more physically motivated forms of solution.

As discussed above, models already require high mass-loading factors for low mass galaxies in order to reproduce galaxy stellar mass functions. Most models define mass-loading factors that depend only on the halo circular velocity $V_{\rm circ}$, but it is likely that in reality the mass-loading factor depends on other galaxy properties as well. These other properties, such as metallicity, gas density, and pressure, could introduce an effective redshift dependence in the mass-loading factor expressed in terms of $V_{\rm circ}$. To reproduce dwarf galaxy properties by altering supernova feedback, reheating must be preferentially more efficient at low masses and high redshifts, a scenario we call "preferential reheating." If we instead address the problem in terms of star formation itself, star formation efficiencies in low mass halos must be lower than in high mass halos. Models usually implement this as a gas surface density threshold, another quantity that is most likely dependent on galaxy properties not taken into account in the model. A changing star formation efficiency can be viewed as either a redshift and/or halo mass dependent fraction of a galaxy's gas available for star formation or as a changing star formation timescale. In either case, adjusting the star formation efficiency could allow low mass galaxies to have their star formation suppressed until more gas accumulates onto the disk, delaying the galaxy's star formation. We will refer to this scenario as "direct suppression." Lastly, small halos may have trouble accreting gas in the first place. The photo-ionizing background suppresses gas accre-

tion in the very smallest halos at high redshift (Efstathiou, 1992; Quinn et al., 1996; Somerville, 2002; Somerville et al., 2008b, and references therein), but there could be some "pre-heating" mechanism that acts on halos up to $\sim 10^{10}\ M_\odot$, preventing accretion of gas (e.g. Lu et al., 2015). The gas would instead remain in a "parking lot," waiting to be accreted at later times. Star formation in low mass galaxies would then be delayed until gas is released from the parking lot at lower redshifts. We will refer to this as the parking lot scenario.

We implement these three model variants, preferential reheating, direct suppression, and parking lot, within the Santa Cruz semi-analytic model (Somerville et al., 2008b, 2012), and explore the implications for a set of complementary observations. These include the fraction of stellar mass to halo mass as a function of halo mass, the comoving number density of low mass galaxies as a function of redshift, and scaling relations between the galaxy stellar mass and the cold gas fraction, specific star formation rates, and metallicity.

The baseline semi-analytic model is described in Section 2.2 and we discuss the predictions of the fiducial model in Section 2.3. In Section 2.4, we describe an exploration of parameter space in the existing model in order to gain insight into how various model ingredients affect the observables. In Section 2.5, we present the results of our preferential reheating, direct suppression, and parking lot models. Section 2.6 explores possible reasons for differences between our results and those presented by Henriques et al. (2013) and we discuss the implications of our results and conclude

in Section 2.7.

2.2 Summary of the model

In this work, we use the baseline model described in Somerville et al. (2008b, S08) and Somerville et al. (2012, S12). We adopt a Chabrier stellar initial mass function (IMF) and WMAP5 cosmological parameters: $\Omega_0 = 0.28$, $\Omega_\Lambda = 0.72$, $h_{100} = 0.70$, and $f_{\rm baryon} = 0.1658$ (Komatsu et al., 2009). We shut off AGN feedback, both radio mode and quasar mode, in all of the simulations presented. AGN feedback as implemented in our model does not noticeably affect galaxies with halo masses $\rm M_H \lesssim 10^{11.75}$ and omitting AGN feedback isolates any effects from our adjusted recipes on high mass halos.

The merging histories of dark matter halos are constructed based on the Extended Press-Schechter (EPS) formalism following the method described in Somerville & Kolatt (1999) and Somerville et al. (2008b). We follow the merger history of a particular halo back to a minimum progenitor mass of 0.01 times the final mass of the halo. Whenever dark matter halos merge, the central galaxy of the largest progenitor halo becomes the new central galaxy and all the other galaxies become "satellites." Satellite galaxies may eventually merge with the central galaxy due to dynamical friction and these merger timescales are estimated using a variant of the Chandrasekhar formula from Boylan-Kolchin et al. (2008). Tidal stripping and destruction of the

satellites is included as described in Somerville et al. (2008b).

2.2.1 Gas handling

The SAM tracks four "boxes" of gas: a cold disk representing the ISM, a hot halo representing the intra-group or -cluster medium (ICM), an ejected gas reservoir holding gas that has been ejected from the galaxy and pristine gas prevented from accreting from the IGM by the photo-ionizing background, and a reservoir containing intergalactic medium (IGM) gas that has never been inside a resolved halo. Gas is assigned to reservoirs and moves between them as follows. Gas in the ejected reservoir is allowed to accrete into the hot halo, and gas in the hot halo may cool and fall onto the cold disk. Stellar feedback reheats gas in the cold disk, moving it to the hot halo or ejecting it to the ejected reservoir. New gas is added to the hot halo through pristine gas accretion from the IGM and stripping of gas from satellites as they fall into the main halo.

On creation, halos are assigned a certain mass of gas. Before the reionization of the universe, each halo is assigned its universal baryon fraction's worth of gas, but after reionization the collapse of gas into low-mass halos is suppressed by the photo-ionizing background ("squelching"). In the published models of S08 and S12, the fraction of baryons that can collapse into halos of a given mass after reionization is modeled using the fitting functions provided by Gnedin (2000) and Kravtsov et al. (2004b). Some more recent studies indicate that the characteristic mass below which squelching

strongly prevents accretion, called the filtering mass, predicted by Gnedin (2000) may be too large (e.g. Okamoto et al., 2008). According to this more recent work, the halo mass at which halos have their baryon fractions reduced by a factor of two on average due to squelching is only about $M_{\rm H} \sim 9.3 \times 10^9\ M_\odot$ at $z = 0$ rather than $M_{\rm H} \sim 10^{10.5}$ $M_\odot$ used in Gnedin (2000) and Kravtsov et al. (2004b). This halo mass is much lower than the lowest-mass host halos considered in this work, and therefore simply turning off squelching provides a good approximation to implementing this lower filtering mass. We therefore turn squelching off before conducting our experiments with other aspects of the model.

Hot halo gas is assumed to be distributed in an isothermal sphere at the halo's virial temperature. Halo gas cools through collisionally excited atomic lines as described in S08, based on the model originally proposed in White & Frenk (1991). All cooled gas is added to the cold disk of the central galaxy. When halos become satellites, they are stripped of their hot gas and their ejected reservoir and are not allowed to accrete any more gas. The stripped gas is added to the central galaxy's hot gas halo. Gas in the ejected gas reservoir is allowed to re-accrete into the hot gas halo at a rate given by:

$$\dot{M}_{\rm ReIn} = \chi_{\rm ReIn} \left(\frac{M_{\rm eject}}{t_{\rm dyn}} \right) \tag{2.1}$$

Here $\dot{M}_{\rm ReIn}$ is the rate at which gas falls into the hot halo from the ejected gas reservoir, $M_{\rm eject}$ is the mass in the ejected gas reservoir, $t_{\rm dyn}$ is the central halo's dynamical timescale, and $\chi_{\rm ReIn}$ is the efficiency parameter with a default value of $\chi_{\rm ReIn}$= 0.1.

When halos merge, the ejected reservoirs from all but the largest progenitor are added to the hot gas reservoir of the new host halo.

2.2.2 Star formation

Stars form in a "normal" (disk) mode and in merger-driven starbursts. Heavy elements are generated with a fixed yield per stellar mass formed and recycled instantaneously. Details on the starburst treatment may be found in S08. These do not affect this work significantly since the star formation density due to bursts is about an order of magnitude below that due to normal star formation over most of the age of the universe (see Figure 14 in S08). The model assumes that both the cold gas and stars in the disk are distributed with radial exponential profiles with separate scale lengths related by a factor, $r_{\rm gas} = \chi_{\rm gas} r_\star$, with the fiducial value $\chi_{\rm gas} = 1.7$. The scale length of the gas disk is calculated using angular momentum conservation arguments (Mo et al., 1998; Somerville et al., 2008a) based on the halo spin parameter.

Normal star formation in the fiducial model follows a Kennicutt-Schmidt relation (Kennicutt, 1998):

$$\dot{\Sigma}_{\rm SFR} = \frac{A_{\rm K}}{\tau_\star} \Sigma_{\rm gas}^{N_{\rm K}} \tag{2.2}$$

Here, $\tau_\star$ is a dimensionless free parameter with a fiducial value of $\tau_\star = 1.5$ and $\Sigma_{\rm gas}$ is the surface density of the cold gas disk. The values of $A_{\rm K}$ and $N_{\rm K}$ are set by observations to be $A_{\rm K} = 0.167\ M_\odot\ {\rm yr}^{-1}{\rm kpc}^{-2}$ and $N_{\rm K} = 1.4$. At each time step, the

model applies the Kennicutt law to all cold gas with surface density greater than a fixed critical value, $\Sigma_{\rm crit} = 6\ M_\odot\ {\rm pc}^{-2}$.

In some cases, to interpret the effects of the modified recipes more easily, we use a constant efficiency star formation recipe instead of the Kennicutt law. For this, we let the star formation timescale be a free parameter and set

$$\dot{M}_\star = \frac{M_{\rm cold}}{\tau_{\rm CE}} \tag{2.3}$$

The default value of the timescale is $\tau_{\rm CE} = 10^9$ yr.

2.2.3 Stellar feedback

Massive stars and supernovae reheat some of the cold gas following star formation and deposit it either in the hot gas halo or in the ejected gas reservoir. The fraction of the reheated gas which is ejected is determined by the halo virial velocity. The parameter $V_{\rm eject}$ sets the transition from mostly ejected at $V_{\rm vir} < V_{\rm eject}$ to mostly retained in the hot halo at $V_{\rm vir} > V_{\rm eject}$. In the fiducial model, $V_{\rm eject}$= 130 km/s. The total mass of gas reheated is given by:

$$\dot{M}_{\rm RH} = \epsilon_{\rm SN} \left(\frac{V_{\rm circ}}{200\ {\rm km/s}} \right)^{-\alpha_{\rm RH}} \dot{M}_\star \tag{2.4}$$

where $V_{\rm circ}$ is the circular velocity of the disk, defined as the maximum rotation velocity of the dark matter halo, and $\alpha_{\rm RH}$ and $\epsilon_{\rm SN}$ are dimensionless free parameters. In the fiducial model, $\alpha_{\rm RH}$=2.2 and $\epsilon_{\rm SN}$=1.5.

2.2.4 Main free parameters

The parameters most relevant to the properties of low mass galaxies are the re-infall rate normalization $\chi_{\rm ReIn}$, the star formation normalization $\tau_\star$ and critical surface density $\Sigma_{\rm crit}$, and the stellar feedback parameters, power $\alpha_{\rm RH}$, normalization $\epsilon_{\rm SN}$, and ejection/retention transition velocity $V_{\rm eject}$. A summary of how these parameters enter into the recipes can be found in Section 2.2.1 for the re-infall parameter, Section 2.2.2 for star formation parameters, and Section 2.2.3 for the stellar feedback parameters. Complete descriptions can be found in S08.

Some of the fiducial model's parameters correspond to values that can be derived from observations or numerical simulations and are set to those values. Others are not directly measurable and are adjusted so that the simulated galaxy population matches certain sets of observations. The stellar feedback parameters were tuned to match the low mass end of the stellar mass function. The fiducial values are $\alpha_{\rm RH}$=2.2, $\epsilon_{\rm SN}$=1.5, and $V_{\rm eject}$ = 130 km/s. The value of $\chi_{\rm ReIn}$ is degenerate with the wind mass-loading parameters, so the fiducial model adopts $\chi_{\rm ReIn}$= 0.1, the minimal value that allows the model to fit both cluster baryon fractions and the mass function of $z = 0$ low mass galaxies. For normal star formation, the values of $N_{\rm K} = 1.4$ and $A_{\rm K} = 0.167$

$M_\odot$ yr^{-1}kpc^{-2} in the star formation law (Equation 2.2) are taken from observations (Kennicutt, 1998). The fiducial value of $\tau_\star$ is set to be 1.5 to match observed cold gas fractions. The value $\Sigma_{\rm crit} = 6\ M_\odot\ {\rm pc}^{-2}$ is consistent with direct observations and reproduces the observed turn-over in the relationship between star formation rate density and total gas density (Bigiel et al., 2008), as well as reproducing gas fractions in low mass galaxies.

2.3 Properties of the fiducial model

The fiducial model is tuned by hand to match a subset of $z = 0$ observations, the stellar mass function (SMF) in particular, and does fairly well at matching a larger set of $z = 0$ observations (Somerville et al., 2008b, 2012). However, as already discussed and shown in Fontanot et al. (2009) and Lu et al. (2014), it suffers from the usual set of dwarf galaxy problems. This can be seen in observables such as the SMF, cold gas fractions, specific star formation rate (sSFR), and metallicities. In this section, we show the predictions of our fiducial model for the set of properties which are most enlightening. These are $f_* \equiv M_\star/M_{\rm H}$ (Figure 2.1), the stellar mass function (SMF) (Figure 2.2), the cold gas fraction in disks (Figure 2.3), the specific star formation rate (sSFR), $\dot{M}_\star/M_\star$ (Figure 2.4), and the interstellar medium metallicity (Figure 2.5). These properties are shown with the scatter about the median: the "$\pm 1\sigma$ region" which contains 68% of the galaxies in the model. The reader should keep in mind that

all of the simulations run for this work have AGN feedback switched off, including the fiducial model. This means the high mass galaxies will not necessarily match observations. In addition, as we discuss above, the implementation of squelching in the fiducial model is most likely too aggressive so we also show the fiducial model without squelching in these figures in addition to the model with squelching.

2.3.1 Stellar mass function and $f_\star$

The fiducial model is tuned to approximately match the $z \sim 0$ observations of the SMF. However, to match the "kink" in the SMF precisely at low masses ($M_\star \lesssim 10^{9.5}$ $M_\odot$), we would need to adopt a more complicated scaling for the mass-loading factor than our single power-law (Lu et al., 2014). Our fiducial model lies within the error bars on the SMF observations of Baldry et al. (2008) for $M_\star \gtrsim 10^8$ $M_\odot$. We also compare to the observed SMFs from Baldry et al. (2012); Santini et al. (2012); Moustakas et al. (2013); Tomczak et al. (2014) and Marchesini et al. (2009) (Figure 2.2). In Figure 2.1, we compare to the $f_\star\,(M_{\rm halo})$ relation from Behroozi et al. (2013a), which we expect to match about as well as we match the SMF since $f_\star\,(M_{\rm halo})$ is derived from the SMF.

The fiducial model fits the observed $f_\star\,(M_{\rm halo})$ and SMF well over the range of masses of interest, $10^{10} M_\odot \lesssim M_{\rm H} \lesssim 10^{11.5} M_\odot$ at $z = 0$. The high mass end of the $f_\star$ relation shown in Figure 2.1 is high at $z = 0$ due to the absence of AGN feedback in these simulations. Note that the *deficit* of galaxies in the SMF at stellar masses

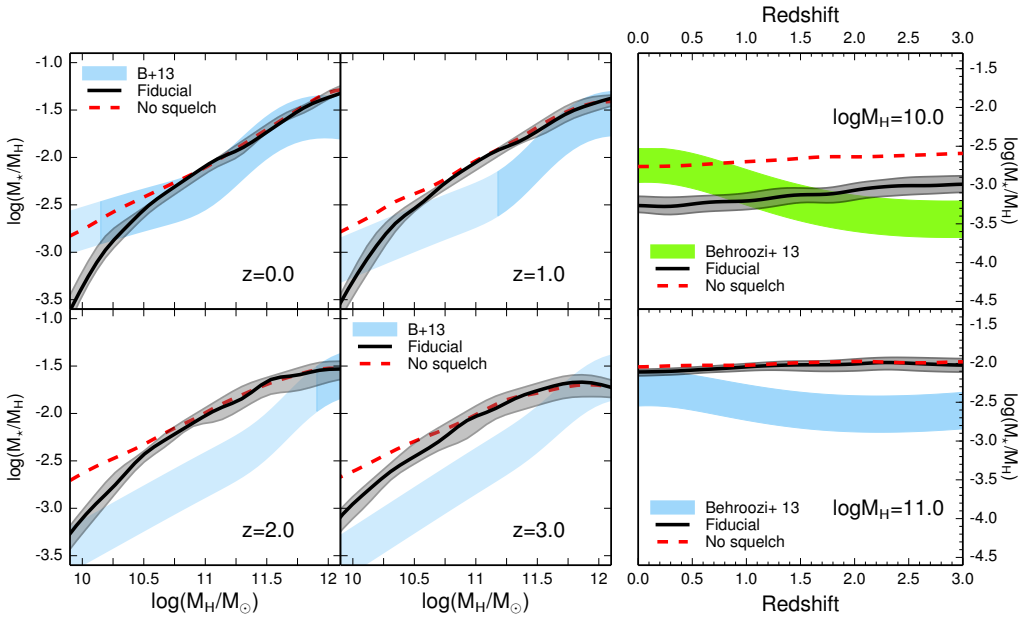

Figure 2.1: Ratio of stellar mass to halo mass ($f_\star$) in the fiducial model. In all panels, the fiducial model is shown in black with the $\pm1\sigma$ region shaded gray. The red dashed line shows the median of the fiducial model with photo-ionization squelching switched off (see text). **Left panel:** $f_\star$ as a function of halo mass shown for four redshifts. Empirical constraints on $f_\star$ from Behroozi et al. (2013a) are shown by their $\pm1\sigma$ region shaded blue where there are observational constraints and light blue where the relation is extrapolated. **Right panel:** $f_\star$ as a function of redshift for halo mass $M_{\rm H} = 10^{10}\ M_\odot$ in the top panel and halo mass $M_{\rm H} = 10^{11}\ M_\odot$ in the lower panel. Behroozi et al. (2013a) results are shown as shaded regions indicating $\pm1\sigma$ region.

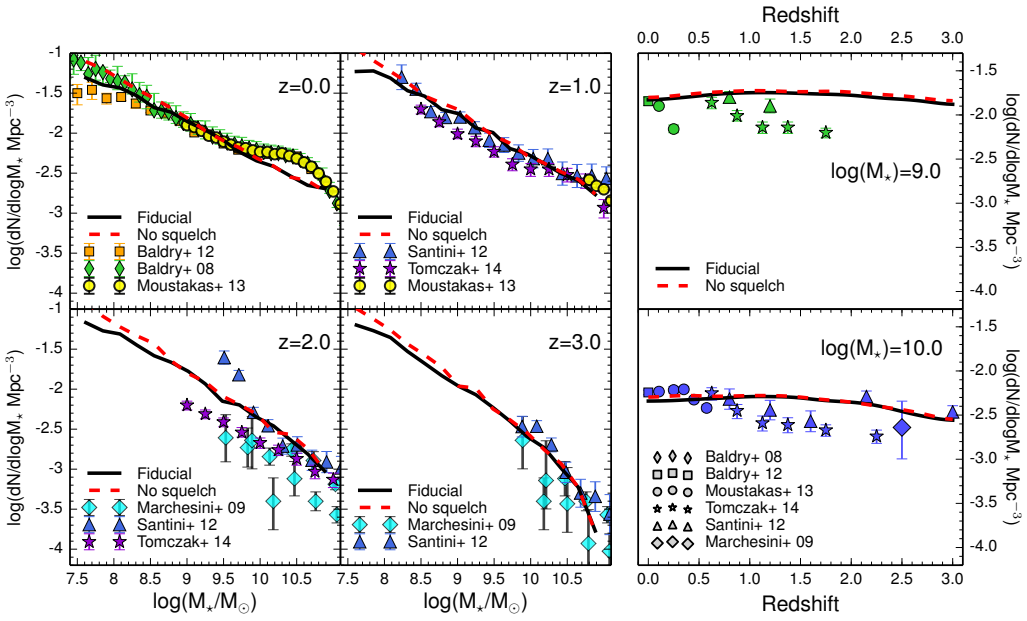

Figure 2.2: Stellar mass function for the fiducial model. In all panels, the fiducial model is shown in black and the red dashed line shows the fiducial model with photo-ionization squelching switched off (see text). **Left panel:** stellar mass functions for four redshifts. Colored points show observations from Baldry et al. (2008) as green diamonds, Baldry et al. (2012) as orange squares, Moustakas et al. (2013) as yellow circles, Santini et al. (2012) as dark blue triangles, Tomczak et al. (2014) as purple stars, and Marchesini et al. (2009) as wide cyan diamonds. **Right panel:** the number densities as a function of redshift for galaxies with $M_\star = 10^9\ M_\odot$ in the top panel and $M_\star = 10^{10}\ M_\odot$ in the lower panel. Data are shown as points with the same shape as in the left panel.

$M_\star \gtrsim 10^{10}\ M_\odot$ is also due to the absence of AGN feedback – some of these galaxies should arise from more massive halos, due to the "turnover" in $f_\star$ at larger halo masses (see e.g. S08). The fiducial model's sharp decrease in $f_\star$ at the lowest masses (below $M_{\rm H} \sim 10^{10.5}\ M_\odot$) is due to photo-ionization squelching of low mass halos as described in 2.2.1.

At higher redshift, both $f_\star$ and the SMF show an excess of stellar mass, increasingly so towards $z \sim 2$. Constraints on $f_\star$ for low mass galaxies show that for a fixed halo mass, the stellar mass increases over time, whereas the SAM predicts that stellar mass at a fixed halo mass decreases: the dark matter halos of modeled low mass galaxies grow slightly faster than the stellar mass. Additionally, the slope of the SAM's $f_\star\,(M_{\rm halo})$ relation becomes steeper from high redshift to low, indicating that at high redshift, the overall efficiency of star formation is not suppressed enough in the lower mass halos relative to the higher mass halos. The model's SMF shows an excess of all low mass galaxies towards higher redshift because the SAM galaxies at a particular stellar mass have lower halo mass due to their too-high overall star formation efficiency, and therefore reside in more abundant halos than the observed galaxies.

2.3.2 Cold gas fractions

At low redshift, direct estimates of cold gas content can be obtained from 21 cm emission which traces HI and CO emission which traces H_2. We compare with the

compilation of Peeples et al. (2014), which includes HI and H_2. At high redshift, $z \gtrsim 0.2$, direct estimates of H_2 content from CO observations are available for only a small number of relatively massive galaxies. Therefore, we also compare to the Popping et al. (2014a) work, which uses an empirical model to estimate gas fractions. The Popping et al. (2014a) work uses a subhalo abundance matching procedure to determine typical star formation rates as a function of halo mass and redshift. They invert these typical star formation rates with an empirical molecular hydrogen-based star formation law to find the gas mass in HI and H_2 assuming gas distributions and using a pressure-based recipe dictating the ratio of molecular to atomic hydrogen. We also plot estimates of the H_2 fraction for individual galaxies from Narayanan et al. (2012), which are obtained from a re-analysis of CO measurements with a more sophisticated model for the conversion of CO emission to H_2 mass than the standard single CO to total gas ratio.

Cold gas fractions in the fiducial model match well with observations at $z = 0$ (Figure 2.3), unsurprisingly as the model was tuned to match these data. However, at intermediate redshifts $0.5 < z < 1.5$, gas fractions are too low for galaxies with $M_\star \lesssim 10^{10} M_\odot$, as also noted in Popping et al. (2014b). This may be another symptom of the fact that these galaxies are forming stars too early. At higher redshifts, $z \gtrsim 2$, the fiducial model's cold gas fractions again match up with the predictions from the empirical model. It is important to note that the galaxies included in the cold gas fraction plots are selected to be disk galaxies (bulge stellar mass to total stellar mass

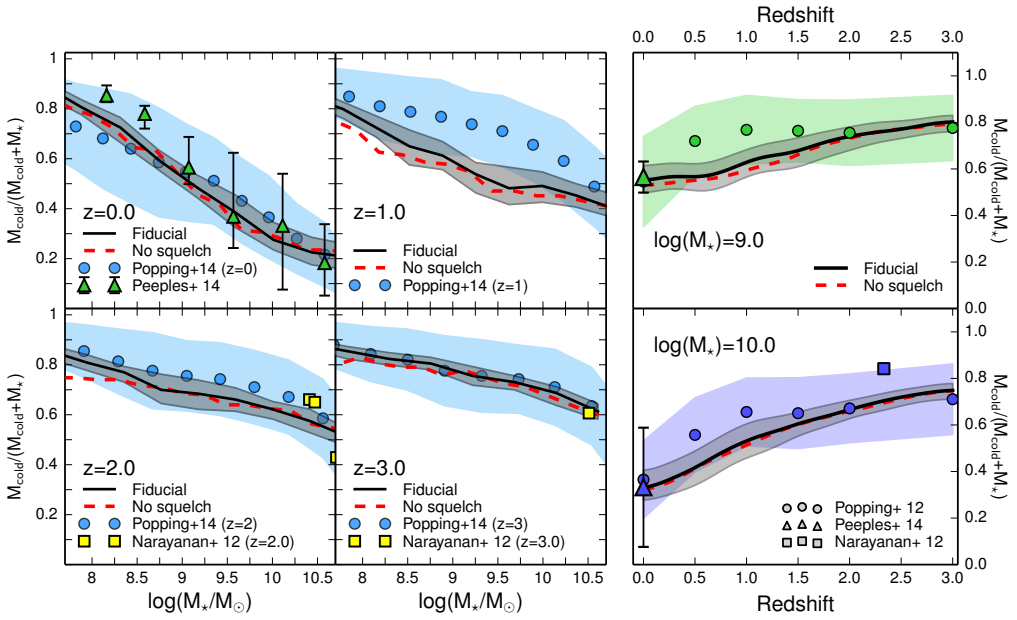

Figure 2.3: Cold gas fractions for the fiducial model. In all panels, the fiducial model is shown in black with the $\pm 1\sigma$ region shaded gray. The red dashed line shows the median of the fiducial model with photo-ionization squelching switched off (see text). We show only galaxies with nonzero gas fractions and bulge to total ratios B/T<0.4. **Left panel:** the cold gas fraction shown as a function of stellar mass at four redshifts. The Peeples et al. (2014) points, shown as green triangles in the $z = 0$ panel, are averages of a collection of data sets in stellar mass bins. We also show the indirect cold gas fraction estimates from the Popping et al. (2014a) empirical model as blue circles with the $\pm 1\sigma$ region shaded light blue and direct estimates of molecular gas fraction from Narayanan et al. (2012) as yellow squares. Note that the Narayanan et al. (2012) points are individual galaxies rather than binned results. See Section 2.3.2 for a more complete discussion of cold gas observations. **Right panel:** gas fractions as a function of redshift for galaxies with stellar mass $M_\star = 10^9\ M_\odot$ in the top panel and $M_\star = 10^{10}\ M_\odot$ in the lower panel. Data are shown as points with the same shape as in the left panel and the errors on the Popping et al. (2014a) gas fractions shown as colored shaded regions.

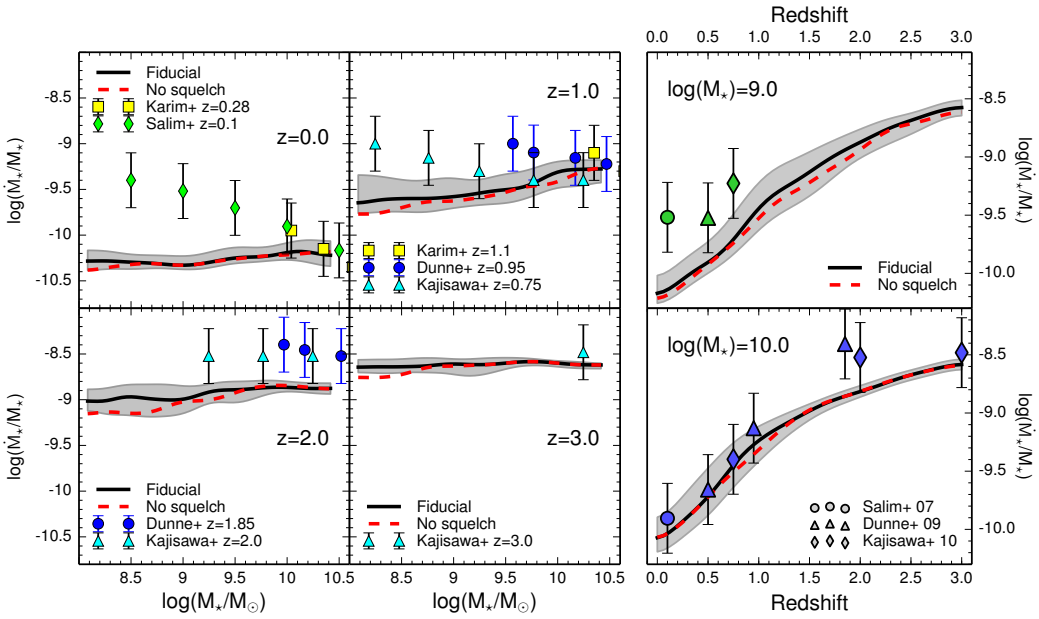

Figure 2.4: Specific star formation rates ($\dot{M}_\star/M_\star$) for the fiducial model. In all panels, the fiducial model is shown in black with the $\pm1\sigma$ region shaded gray. The red dashed line shows the median of the fiducial model with photo-ionization squelching switched off (see text). **Left panel:** specific star formation rates vs. stellar mass for four redshifts. Points show data from the sources given in the legends. Note that the errors on the sSFR data are not from the original works but from Behroozi et al. (2013a), calculated using many data sets to estimate any systematic errors unaccounted for in original sources. **Right panel:** sSFR as a function of redshift for $M_\star$= 10^9 $M_\odot$ in the top panel and $M_\star$= 10^{10} $M_\odot$ in the lower panel. The shapes of the data points denote the source.

ratio of less than 0.4) and have non-zero cold gas mass.

2.3.3 Specific star formation rates

Figure 2.4 shows the average specific star formation rate (sSFR) vs. stellar mass and redshift in the fiducial model. The "star forming sequence" in observations has a slightly negative slope: the lowest mass galaxies have somewhat higher sSFRs than

intermediate mass galaxies. In the fiducial model, sSFRs of low mass galaxies are too low and the SF sequence is flat or even has a positive instead of negative slope. The fiducial model does more or less match the observed increase in sSFR with increasing redshift, but the normalization is too low for low mass galaxies from $0 \lesssim z \lesssim 1$. We compare to observations from Salim et al. (2007); Dunne et al. (2009); Kajisawa et al. (2010); Karim et al. (2011).

2.3.4 Metallicity

Figure 2.5 shows the gas-phase metallicity as a function of redshift for three different stellar mass bins. The metallicity estimates at $z \sim 0$ are from Tremonti et al. (2004), obtained using photo-ionization and stellar population evolution models fit to SDSS spectroscopy. At $z \sim 1$, we use the estimates of Savaglio et al. (2005), derived from Gemini Deep Deep Survey spectra with the R_{23} method. At $z \sim 2$, we use the results of Erb et al. (2006) from Hα and NII in spectra of star-forming galaxies, and at $z \sim 3$, the results of Maiolino et al. (2008), using strong line diagnostics such as Hβ, OII, OIII, and NeIII. We note that the absolute normalization of the metallicity from different indicators is highly uncertain, which may impact the redshift evolution implied by the observations shown here (Kewley & Ellison, 2008). We also note that the chemical yield in our model ($y = 1.5$ in solar units) was chosen to match the *stellar* metallicity of Milky Way mass galaxies at $z \sim 0$ from observations (Gallazzi et al., 2005). The gas-phase mass-metallicity relation predicted by our models is a

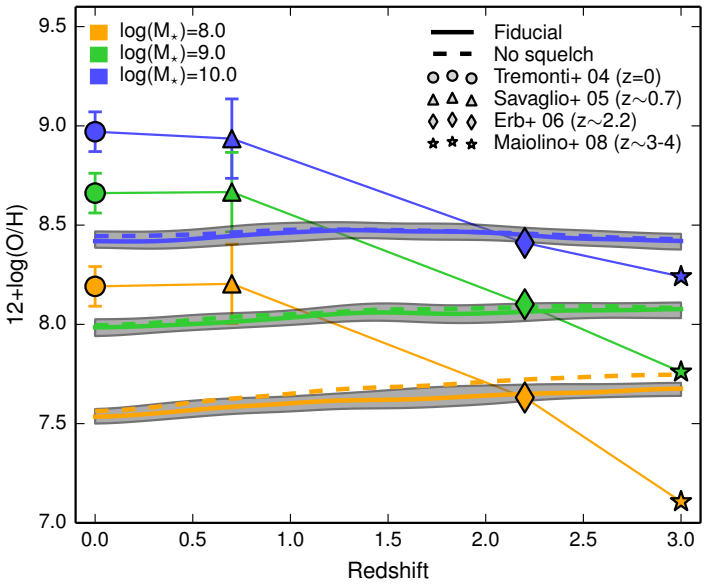

Figure 2.5: Gas phase metallicities for galaxies in the fiducial model for selected stellar masses as a function of redshift. Only galaxies with gas fractions greater than 0.2 are included. Metallicities are color coded according to the stellar mass bin they represent. Fiducial model curves are shown as thick lines with shaded gray regions giving $\pm 1\sigma$ and observations are shown as points whose shapes indicate which data set they represent. Dashed lines show the fiducial model with squelching switched off.

steeper function of stellar mass than the observed relations, and is a pure power-law in stellar mass, unlike observations which turn over at high mass. The fiducial model also builds up metals very early, predicting almost no evolution in the metallicity of gas in galaxies at fixed stellar mass, or even a slight decrease. This disagrees with the trend implied by the observations taken at face value, which suggest an increase of more than an order of magnitude in metallicity at fixed stellar mass since $z \sim 3$.

2.4 Exploration of existing parameter space

Before changing the model recipes, we examine how the fiducial model responds to parameter variations. We test this by running the model with all parameters set to the fiducial values except for one parameter, which is set to a value significantly higher or lower than the fiducial value. We examined the set of parameters most likely to affect star formation: the wind parameters, $\alpha_{\rm RH}$, $\epsilon_{\rm SN}$, and $V_{\rm eject}$; the star formation parameters, $\tau_\star$, $\chi_{\rm gas}$, and $\Sigma_{\rm crit}$; and the re-infall parameter $\chi_{\rm ReIn}$. Of these, only $\epsilon_{\rm SN}$, $\alpha_{\rm RH}$, $\tau_\star$ and $\chi_{\rm ReIn}$ had significant impact on low mass galaxy properties. Adjusting the stellar feedback parameters, $\epsilon_{\rm SN}$ and $\alpha_{\rm RH}$, strongly affects the ratio of stellar mass to halo mass, $f_\star$. Adjusting $\tau_\star$ mainly affects cold gas fractions and adjusting $\chi_{\rm ReIn}$ mainly affects low redshift star formation rates. Changing $V_{\rm eject}$ or $\Sigma_{\rm crit}$ has little effect on galaxy properties; changing $\chi_{\rm gas}$ has none.

We find that no fixed value of any of these parameters can alter the undesirable fiducial trends with redshift. In Figure 2.6, we show the redshift $z = 0$ $f_\star\,(M_{\rm halo})$, SMF, cold gas fraction, and sSFR for the fiducial model and variations in $\epsilon_{\rm SN}$, $\alpha_{\rm RH}$, $\tau_\star$, and $\chi_{\rm ReIn}$. Each column shows the fiducial model and a high and low value of a different parameter. Figure 2.7 shows $f_\star(z)$ for $M_{\rm halo}$=10^{10} $M_\odot$ halos and the cold gas fraction, sSFR, and ISM metallicity as a function of redshift for $M_\star$=10^9 $M_\odot$ galaxies for the same parameter variations.

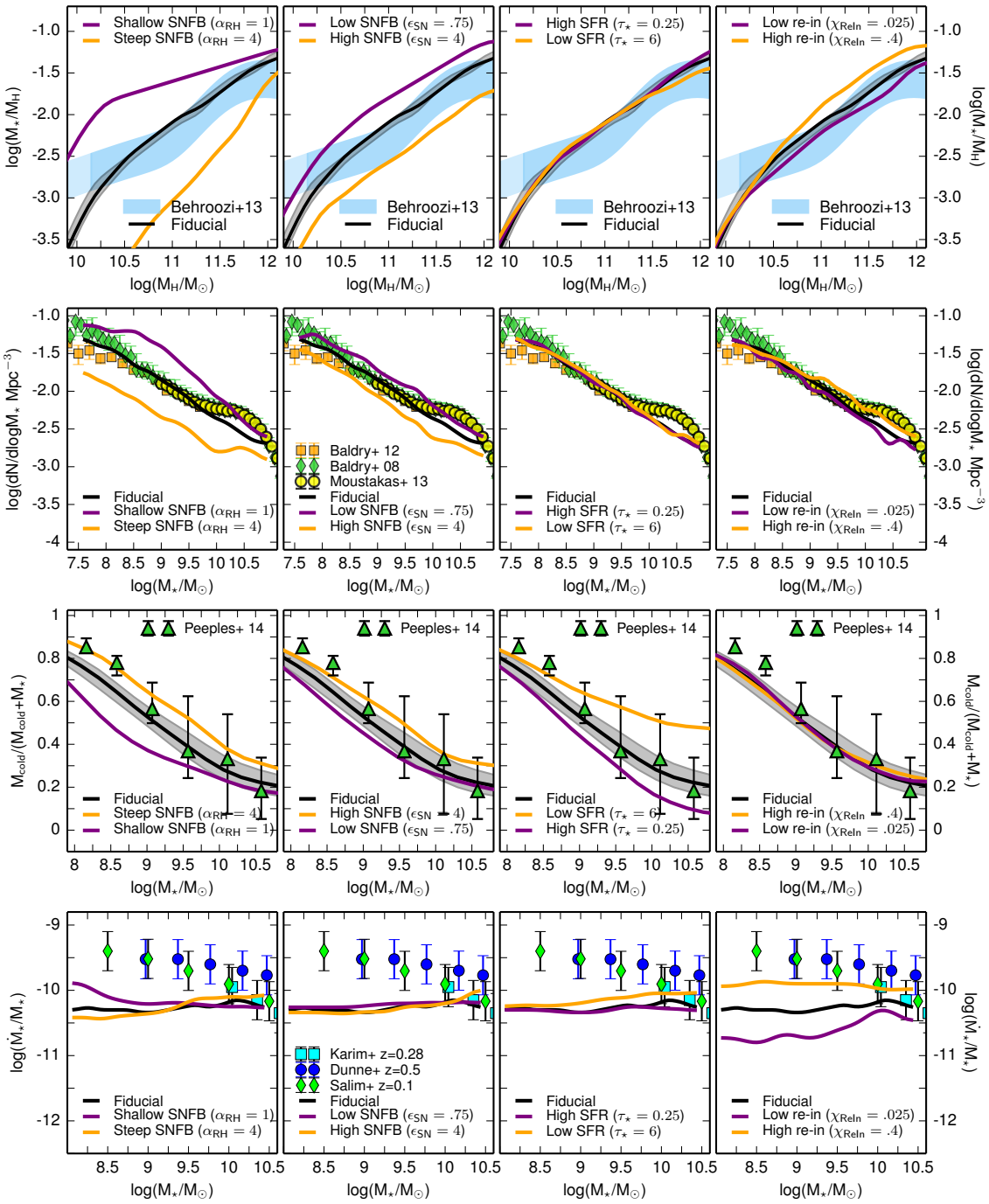

Figure 2.6: $f_\star$, SMF, cold gas fraction, and sSFR results at redshift $z = 0$ for high and low values of $\alpha_{\rm RH}$ in the left column, $\epsilon_{\rm SN}$ in the second column, $\tau_\star$ in the third column, and $\chi_{\rm ReIn}$ in the right-most column. The fiducial model is shown in black, the low parameter value is shown in purple, and the high parameter value is shown in yellow. Data are as noted in legends.

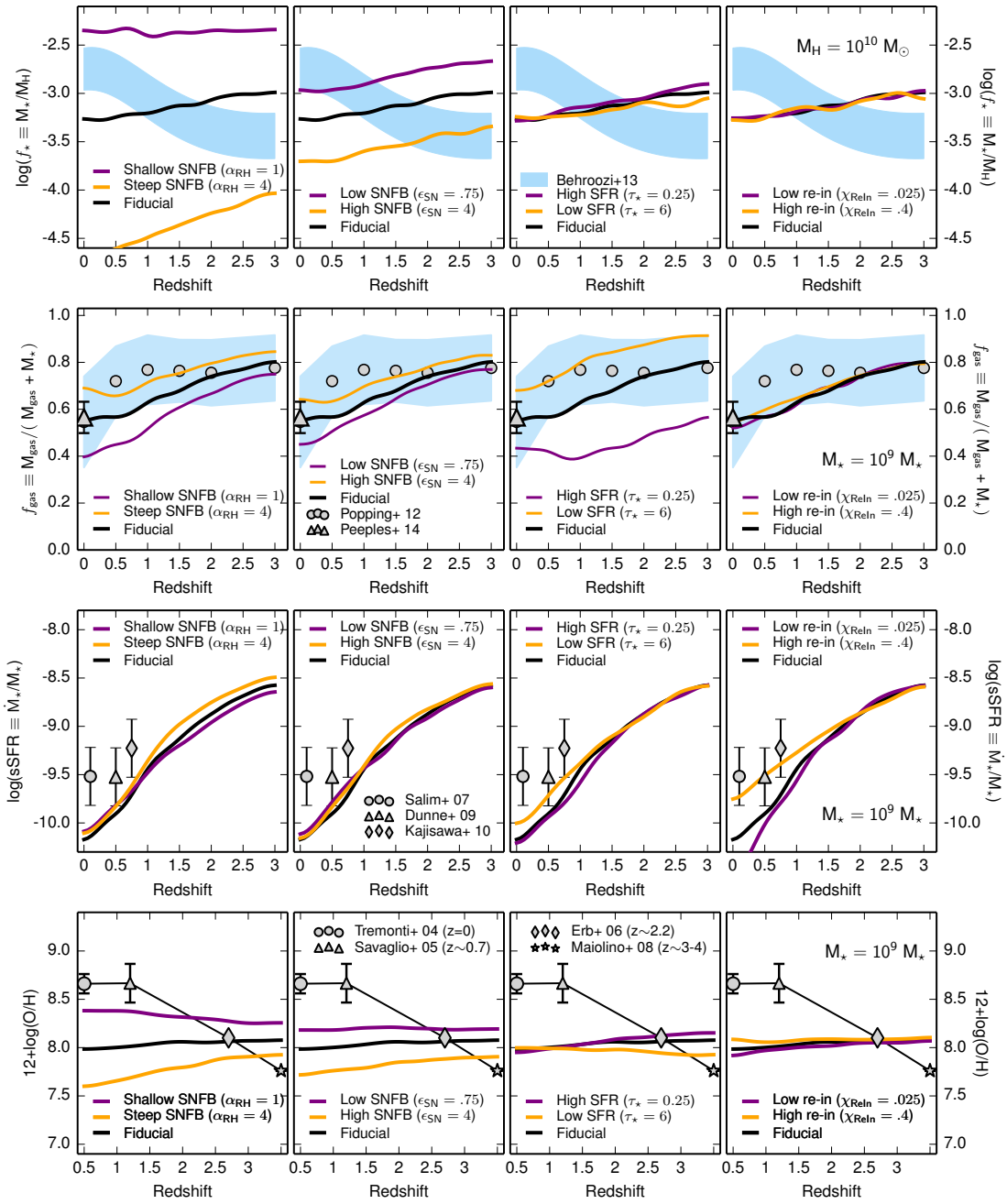

Figure 2.7: $f_\star$ as a function of redshift for halo mass $M_{\rm H} = 10^{10}\ M_\odot$ and cold gas fractions, sSFR, and ISM metallicity as a function of redshift for stellar mass $M_\star = 10^9\ M_\odot$ galaxies. We show models with low, fiducial, and high values of $\alpha_{\rm RH}$ in the left column, $\epsilon_{\rm SN}$ in the second column, $\tau_\star$ in the third column, and $\chi_{\rm ReIn}$ in the right-most column. Low parameter value models are shown in purple, the fiducial model is shown in black, and high parameter value models are shown in yellow. Data are as noted in legends.

2.4.1 Varying $V_{\rm eject}$ or $\Sigma_{\rm crit}$

The value of $V_{\rm eject}$ dictates the transition between ejecting and retaining gas that is reheated by stellar-driven winds as detailed in Section 2.2.3. Changing $V_{\rm eject}$ primarily affects intermediate mass halos with masses between $10^{11.5}$-$10^{12.5}$ $M_\odot$. These halos see a decrease in star formation when $V_{\rm eject}$ is increased because galaxies must wait for ejected gas to fall back into the halo again before forming more stars, which would not be the case for the fiducial value of $V_{\rm eject}$. This effect is minor.

The value of $\Sigma_{\rm crit}$ sets the critical surface density for star formation: only cold gas in parts of the disk with surface density higher than $\Sigma_{\rm crit}$ is considered available for star formation (see Section 2.2.2). Higher $\Sigma_{\rm crit}$ leads to somewhat lower star formation efficiency and somewhat higher cold gas fractions; less gas is available for star formation and the unavailable gas resides in the outer edges of the disk.

2.4.2 Varying $\epsilon_{\rm SN}$ or $\alpha_{\rm RH}$

The amount of gas reheated by stellar feedback is determined by Equation 2.4 and the values of $\epsilon_{\rm SN}$ and $\alpha_{\rm RH}$. The value of $\epsilon_{\rm SN}$ controls the normalization of the stellar feedback relation. As $\epsilon_{\rm SN}$ increases, winds become more efficient at removing gas from the cold disk. Galaxies form a few stars, eject a large amount of gas, then have to wait for the reheated gas to cool again before forming any more stars. The overall effect is that increasing $\epsilon_{\rm SN}$ decreases the total mass of stars formed independent of halo

mass: the shape of the $f_\star\,(M_{\rm halo})$ relation doesn't change but the overall star formation efficiency decreases. This is seen most clearly in the first row, second column of Figure 2.6. The cold gas fraction, $M_{\rm cold}/(M_{\rm cold}+M_\star)$, changes less than one might expect as $\epsilon_{\rm SN}$ increases because both the cold gas and stellar masses decrease. Specific star formation rates are also largely independent of $\epsilon_{\rm SN}$ because stellar masses and star formation rates react similarly to changes in $\epsilon_{\rm SN}$. These trends are illustrated in the second columns of Figs. 2.6 and 2.7.

The value of $\alpha_{\rm RH}$ determines how much more strongly low mass halos are affected by stellar feedback than high mass halos. Increasing $\alpha_{\rm RH}$ creates a steeper dependence of mass-loading on halo circular velocity. This suppresses star formation more strongly in low mass halos relative to high mass halos, resulting in a steeper dependence of $f_\star$ on halo mass and a reduced comoving number density of low mass galaxies relative to high mass galaxies. This is most evident in the redshift $z=0$ $f_\star\,(M_{\rm halo})$ relation as shown in the first row, first column of Figure 2.6. The slope of the sSFR-$M_\star$ relation depends weakly on $\alpha_{\rm RH}$, with larger values of $\alpha_{\rm RH}$ leading to lower values of sSFR in low mass galaxies, and therefore to flatter or more positive slopes in sSFR-$M_\star$. Cold gas fractions are also impacted, with larger values of $\alpha_{\rm RH}$ producing higher gas fractions in low mass galaxies because with higher reheating rates, less gas can turn into stars. The value of $\alpha_{\rm RH}$ also affects the slope of the mass-metallicity relation, and to a lesser extent, its evolution. Feedback ejects metals with the cold gas, so more feedback means more metals transported out of the disk. Larger values of $\alpha_{\rm RH}$

lead to a steeper mass-metallicity relation and a slightly larger decline in gas-phase metallicity at fixed stellar mass with cosmic time. These relations are shown in the first columns of Figs. 2.6 and 2.7.

2.4.3 Varying $\tau_\star$

Counterintuitively, changing the star formation timescale $\tau_\star$ has almost no impact on the $f_\star\left(M_{\rm halo}\right)$ relation or SMF at $z \lesssim 3$ as seen in the third columns of Figs. 2.6 and 2.7. Changing $\tau_\star$ mainly impacts gas fractions, particularly for high mass galaxies. This happens because as star formation efficiency decreases, gas mass builds up to compensate. Longer star formation timescales delay star formation, so the $f_\star\left(M_{\rm halo}\right)$ relation is low at high redshift, $z \gtrsim 6$. Note that $\tau_\star$ multiplies a timescale so higher $\tau_\star$ means lower star formation efficiencies and higher gas fractions. Lower SF efficiency (higher $\tau_\star$) therefore leads to a flatter relation between gas fraction and stellar mass since the gas supply in low mass galaxies is more modulated by the stellar feedback. For the most part, the slope of the gas fraction with redshift at fixed mass does not depend strongly on $\tau_\star$, nor does the slope of the sSFR-$M_\star$ relation or the redshift evolution of the sSFR at fixed mass.

2.4.4 Varying $\chi_{\rm ReIn}$

Modulating the re-infall timescale by varying $\chi_{\rm ReIn}$ mainly changes low redshift galaxy properties as shown in the right-most column of Figure 2.7. This is because re-infall timescales are long for all reasonable values of $\chi_{\rm ReIn}$, so most re-accretion occurs at late times. In the fiducial model, the re-infall timescale is constant with halo mass and increases with time. Higher $\chi_{\rm ReIn}$, meaning more efficient re-infall, increases the total stellar mass of all but the lowest mass galaxies, as shown in the right-most column of Figure 2.6. The lack of dependence on mass is due to the halo mass-independent increased availability of gas from re-infall: all galaxies have the same fractional increase or decrease in re-infall due to a change in $\chi_{\rm ReIn}$.

The lowest mass galaxies are unaffected by changes in $\chi_{\rm ReIn}$ primarily because of squelching. Squelched galaxies have much or all of the in-falling IGM diverted to the ejected reservoir, rather than it falling into the hot halo as in high mass galaxies. This significantly decreases the accessibility of this gas relative to high mass halos no matter the $\chi_{\rm ReIn}$. Contributing to this effect, low mass halos eject a large fraction of their stellar-driven winds and winds have a high mass-loading factor. Even with efficient re-infall, gas re-accreted onto low mass halos spends little time in the disk before being re-ejected, rendering the re-infall timescale largely irrelevant to squelched galaxies. If squelching is turned off, this is no longer the case and high $\chi_{\rm ReIn}$ leads to higher stellar masses in low mass halos.

2.5 Results with Modified Recipes

The model's response to variation in the current recipes' parameters informs how we should alter the recipes. For example, we have learned that the slope of the mass-loading dependence on halo mass, $\alpha_{\rm RH}$, appears to have the most leverage on $f_\star$, while star formation efficiency will have to change drastically to affect $f_\star$ due to the strongly self-regulated nature of star formation in the models. Note that the purpose of our experiments is to gain a qualitative understanding of which physical scenarios are most promising for solving all facets of the problem, as well as to gain insights into the requirements for a solution. As such, we do not attempt to obtain precise fits to the observations. In addition, we find that models without squelching do a better job of reproducing the normalization and evolution of low mass galaxies' $f_\star\,(M_{\rm halo})$, so we do not include squelching in the models presented below. This is not unreasonable given the more recent work on squelching than that considered in S08, which suggests that the filtering mass is much lower than the mass of the smallest host halos considered here (see Sec. 2.2.1). We also continue to omit AGN feedback. Altered models run with AGN feedback included show the same behavior at low masses as the models shown but obscure any effects of the alterations on high mass galaxies.

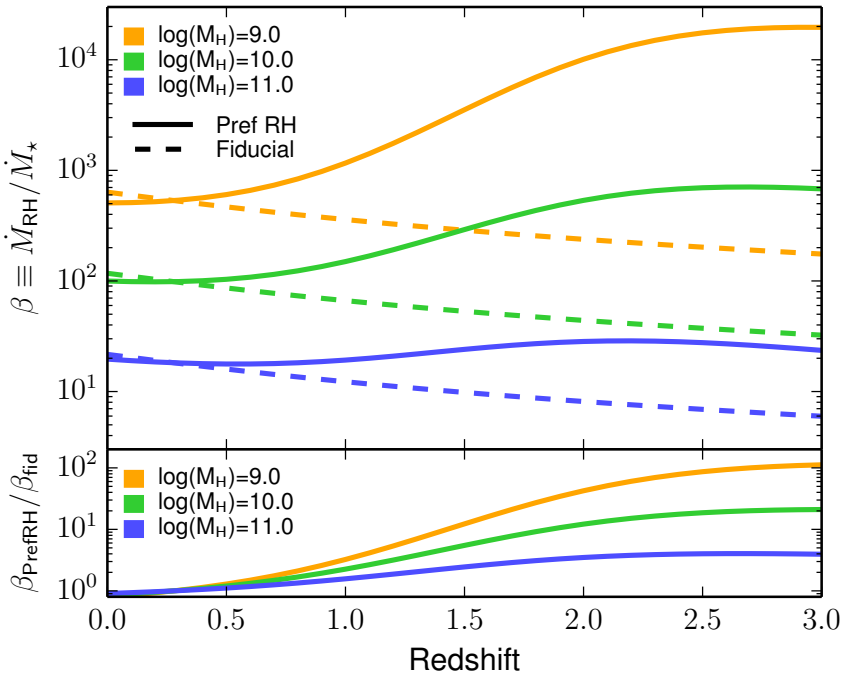

Figure 2.8: A comparison of the fiducial mass-loading factor $\beta_{\rm fid} \equiv \dot{M}_{\rm RH}/\dot{M}_\star$ to the preferential reheating mass-loading factor $\beta_{\rm prefRH}$. The **top panel** shows the values of β for three halo masses, solid lines for preferential reheating and dotted for fiducial. The **bottom panel** shows the ratio $\beta_{\rm prefRH}/\beta_{\rm fid}$ for the same three halo masses.

2.5.1 Preferential reheating: changing stellar feedback scalings

As we have seen, the value of $\alpha_{\rm RH}$ in the stellar feedback recipe (Equation 2.4) controls the slope of the low mass end of $f_\star$. The efficacy of stellar feedback, or mass-loading factor $\beta \equiv \dot{M}_{\rm RH}/\dot{M}_\star$, depends on the halo's maximum circular velocity and thus the halo's mass.[2] We expect β to be mass dependent because ejecting cold gas

[2]The conversion from halo mass to circular velocity is redshift dependent. At high redshift, the same circular velocity corresponds to a lower mass halo. For instance, $V_{\rm c} \sim 160$ km/s corresponds to a $\sim 10^{12}\ M_\odot$ halo at $z = 0$ or a $\sim 10^{11}\ M_\odot$ halo at $z = 3$. (Somerville & Primack, 1999)

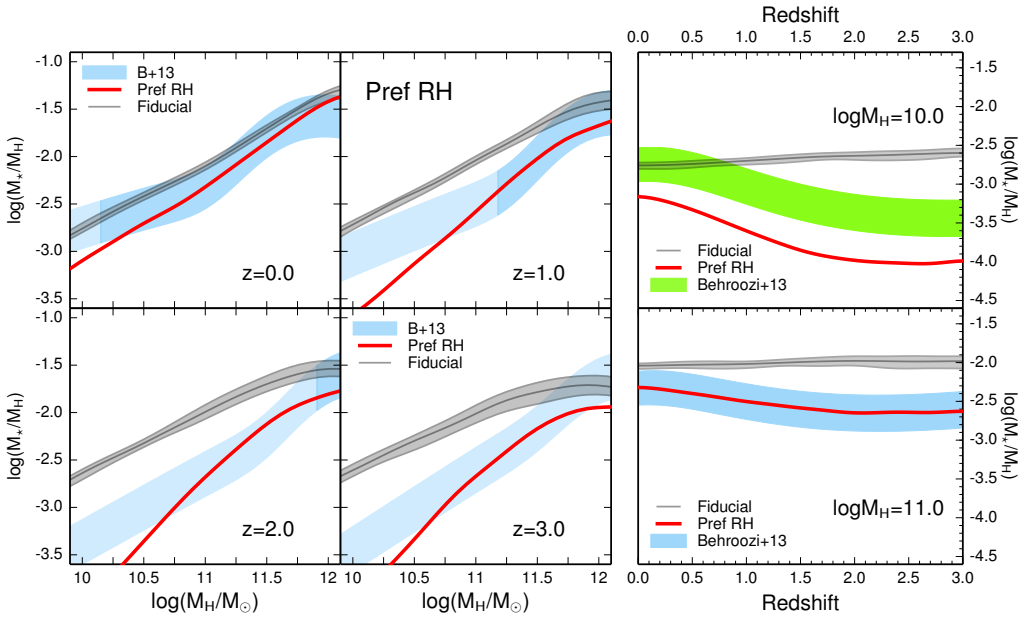

Figure 2.9: Ratio of stellar mass to halo mass, $f_\star$, for the preferential reheating model. In all panels, the preferential reheating model is shown in red and the median and $\pm1\sigma$ region of the fiducial model are shown in gray. **Left panel:** the $f_\star\,(M_{\rm halo})$ relation for four redshifts. **Right panel:** $f_\star$(z) for halo mass $M_{\rm H} = 10^{10}\ M_\odot$ in the top panel and halo mass $M_{\rm H} = 10^{11}\ M_\odot$ in the lower panel. Constraints from Behroozi et al. (2013a) (colored shaded regions) are as described in Figure 2.1.

from a galaxy is much easier in low mass halos than in high mass halos: a parcel of reheated gas has a much shallower potential well to climb out of in a low mass galaxy than it would in a high mass one. Because gas is reheated more efficiently in small halos, less star formation is required to reheat or eject the cold gas. The higher the power $\alpha_{\rm RH}$ of $1/{\rm V_{circ}}$ in Equation 2.4, the more drastic this difference between low- and high-mass galaxies becomes and the steeper the low-mass end of the $f_\star\,(M_{\rm halo})$ relation becomes.

The original form of the supernova reheating recipe (Equation 2.4), $\dot{M}_{\rm RH} \propto V_{\rm circ}^{-\alpha_{\rm RH}}\dot{M}_\star$, originates in simple energy or momentum conservation arguments. If

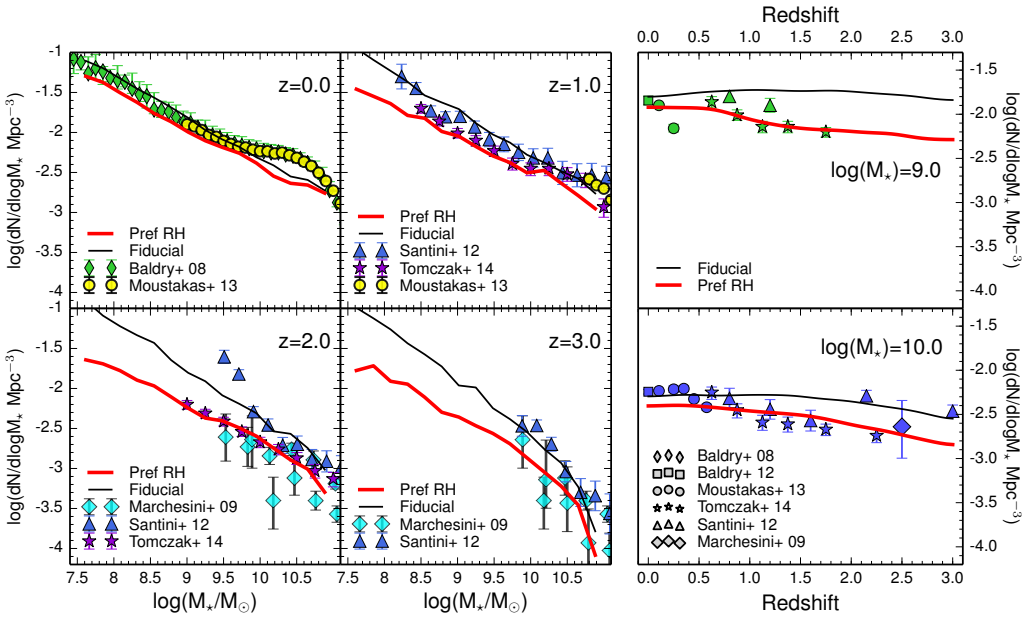

Figure 2.10: Stellar mass function for the preferential reheating model. In all panels, the preferential reheating model is shown in red and the fiducial model is shown in black. Data are as in Figure 2.2. **Left panel:** stellar mass functions for four redshifts. **Right panel:** number densities as a function of redshift for galaxies with $M_\star$= 10^9 $M_\odot$ in the top panel and $M_\star$= 10^{10} $M_\odot$ in the lower panel.

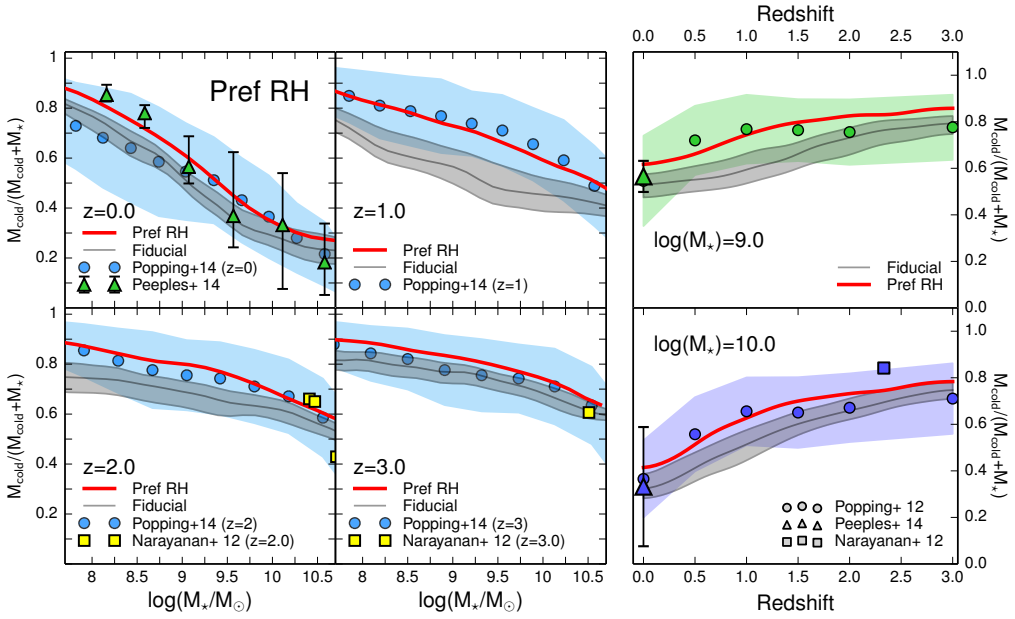

Figure 2.11: Cold gas fractions for the preferential reheating model. In all panels, the preferential reheating model is shown in red and the median and $\pm 1\sigma$ region of the fiducial model are shown in gray. Data are as in Figure 2.3. **Left panel:** cold gas fraction as a function of stellar mass for four redshifts. **Right panel:** cold gas fraction as a function of redshift for galaxies with stellar mass $M_\star = 10^9\ M_\odot$ in the top panel and $M_\star = 10^{10}\ M_\odot$ in the lower panel. In all panels, only galaxies with nonzero gas fraction and bulge to total ratio B/T<0.4 are included.

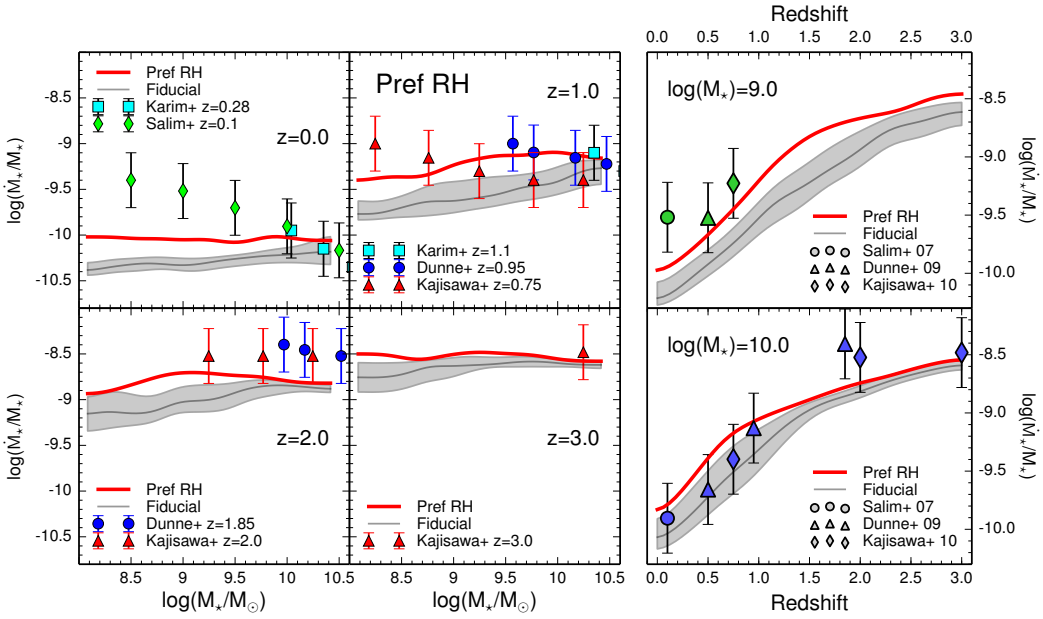

Figure 2.12: Specific star formation rates ($\dot{M}_\star/M_\star$) for the preferential reheating model. In all panels, the preferential reheating model is shown in red and the median and $\pm1\sigma$ region of the fiducial model are shown in gray. Data are as in Figure 2.4. **Left panel:** specific star formation rates as a function of stellar mass for four redshifts. **Right panel:** specific star formation rates as a function of redshift for $M_\star = 10^9\ M_\odot$ in the top panel and $M_\star = 10^{10}\ M_\odot$ in the lower panel.

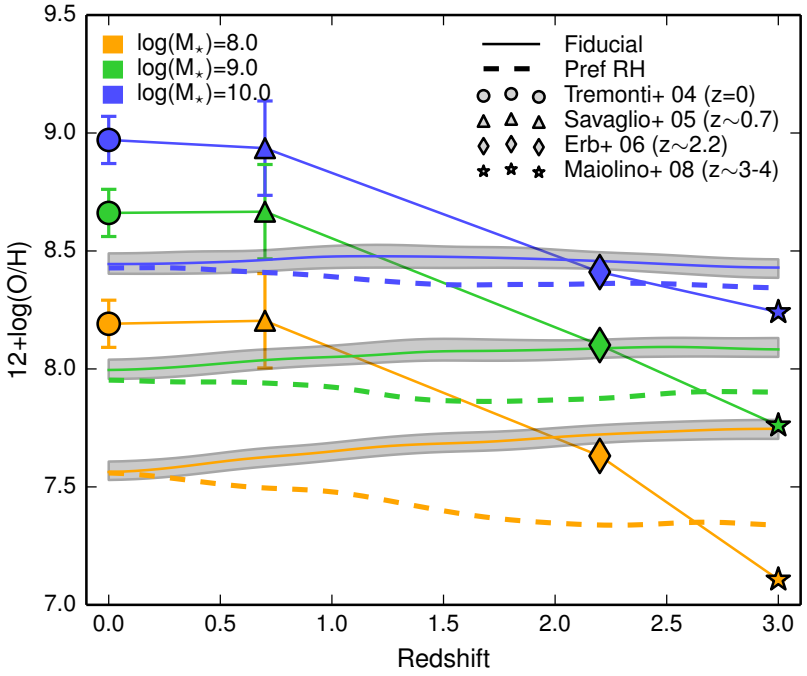

Figure 2.13: Gas phase metallicities for galaxies in the preferential reheating model for selected stellar masses as a function of redshift. Metallicities are color coded according to the stellar mass bin they represent. The thin solid lines and shaded gray regions show the fiducial model's median and $\pm 1\sigma$ region and the thick dashed lines show the preferential reheating model. Only galaxies with gas fractions greater than 0.2 are plotted and observations are shown as points whose shapes indicate which data set they represent.

each supernova produces energy $E_{\rm SN}$ and there are N supernovae per solar mass formed, the energy available to reheat gas will be some fraction of the total energy: $E_{\rm available} \propto E_{\rm SN} N \Delta M_\star$. If all reheated gas is brought to exactly escape velocity, the amount of gas that can be reheated is determined by $\Delta M_{\rm RH} v_{\rm esc}^2 = 2E_{\rm available}$, giving $\Delta M_{\rm RH} \propto \Delta M_\star / v_{\rm esc}^2 \propto \Delta M_\star / V_{\rm circ}^2$. The same argument made with momentum gives $\Delta M_{\rm RH} \propto \Delta M_\star / V_{\rm circ}$.

Our exploration of parameter space showed that no value of $\alpha_{\rm RH}$ that is redshift independent can fit the observed evolution of $f_\star$. In order to reproduce the observed trends, the slope of $f_\star\,(M_{\rm halo})$ must be steeper than the fiducial model, but only at high redshifts, meaning that the value of $\alpha_{\rm RH}$ should be high at high redshift and lower at low redshift. If $\alpha_{\rm RH}$ is left high, star formation is over-suppressed at low redshifts (see Figure 2.6 for a summary of the effects of constant high $\alpha_{\rm RH}$). We tried making $\alpha_{\rm RH}$ constant at low redshifts and rising linearly to high redshift, but this over-suppressed high redshift galaxies. This over-suppression suggested that $\alpha_{\rm RH}$ could not increase indefinitely towards high redshifts.

We also tried to tie $\alpha_{\rm RH}$ to ISM metallicity rather than giving it an explicit redshift dependence. It is plausible that the mass-loading factor depends on the metallicity of the gas being reheated. For example, it may be that higher metallicity implies faster cooling, which would leave less energy to drive winds and tend to make supernova reheating less efficient at lower redshifts. Unfortunately, one of the symptoms of the problem we are trying to solve is a mass-metallicity relation that evolves too

slowly and gives higher metallicity at high redshift than at low redshift, contrary to observations. The models based on metallicity behaved much like the fiducial model because the variation in metallicity and therefore $\alpha_{\rm RH}$ was minimal.

In order to fit the observed evolution of $f_\star$, we find that $\alpha_{\rm RH}$ must be very large at high redshift, $\alpha_{\rm RH}\sim$4-5, then decline to around $\alpha_{\rm RH}\sim$ 2 in a fairly narrow region around z$\sim$ 1.5, then stay approximately constant afterwards. We parametrize $\alpha_{\rm RH}(z)$ as a hyperbolic tangent.

$$\alpha_{\rm RH}(z) = A\tanh\left(B\left(z - z_{\rm trans}\right)\right) + C \tag{2.5}$$

The values of A and C are determined by the minimum $\alpha_{\rm RH}$ ($\alpha_{\rm min}$) and the maximum $\alpha_{\rm RH}$ ($\alpha_{\rm max}$). The value of B dictates the sharpness of the transition between the high and low $\alpha_{\rm RH}$; the higher the value of B, the more abrupt the transition. The model we show has $\alpha_{\rm min} = 2$, $\alpha_{\rm max} = 4.5$, $z_{\rm trans} = 1.5$, and $B = 1$. The mass-loading factor for this model is shown for three halo masses as a function of redshift in Figure 2.8.

This model reproduces several important trends in the evolution of $f_\star$ that the fiducial model does not. The slopes of the low mass end of the $f_\star\,(M_{\rm halo})$ relation at each redshift are much closer to the predictions from Behroozi et al. (2013a) (see Figure 2.9). The redshift evolution of $f_\star$ is also significantly closer to the Behroozi et al. (2013a) evolution. The $\rm M_H = 10^{11}\ M_\odot$ bin reproduces the Behroozi et al. (2013a) result almost exactly, while the $\rm M_H = 10^{10}\ M_\odot$ bin reproduces the shape but

not the normalization. However, the $\rm M_H = 10^{10}\ M_\odot$ curve in Behroozi et al. (2013a) is entirely extrapolated and should taken with a grain of salt. This improvement is also seen in the SMF (Figure 2.10), where there is no extrapolation. We also see improvement in the cold gas fractions. The cold gas fractions from the preferential reheating model are roughly parallel to the fiducial model but somewhat higher (see Figure 2.11). The net result is that the preferential reheating cold gas fractions follow the estimates from the Popping et al. (2014a) empirical model well at all redshifts, perhaps overestimating them slightly at high redshift.

The other low mass galaxy properties are altered in the right direction, but not by enough to be consistent with the observations. Specific star formation rates are somewhat increased at $z \sim 0$ but are still too low and too flat. However, the sSFRs at intermediate redshifts are now marginally consistent with the observations. By redshift $z \sim 3$, the fiducial model and the preferential reheating model have similar sSFRs (Figure 2.12). On a positive note, the preferential reheating model predicts that metallicities increase slightly towards the present day at fixed stellar mass, in better qualitative agreement with the observations, but the metallicity evolution is still too weak (Figure 2.13).

Recent ultra-high resolution numerical simulations that attempt to explicitly model the most important physical processes associated with stellar and supernova feedback suggest that the wind mass-loading factor does scale with galaxy $V_{\rm circ}$ in a manner that is similar to energy or momentum driven winds, but that there is significant

scatter in $\dot{M}_{\rm RH}/\dot{M}_\star$ at fixed $V_{\rm circ}$ (Hopkins et al., 2012). They also find that the mass-loading scales with other galaxy parameters, such as star formation rate and gas surface density, which could introduce an effective redshift dependence in the mass-loading factor. In addition, increasing attention has been paid recently to other possible mechanisms for driving large-scale galactic outflows, such as cosmic rays (e.g. Hanasz et al., 2013).

2.5.2 Direct suppression: changing the star formation efficiency

The appropriate alterations to the star formation recipe are somewhat less clear than those to the stellar reheating recipe. The Kennicutt law has no direct dependence on halo mass, only the surface density of the cold gas. To simplify the recipe, we replaced the Kennicutt law with a constant star formation efficiency law (Equation 2.3). The default constant star formation efficiency model produces results similar to the fiducial model, mainly differing in cold gas fraction predictions: the constant efficiency star formation recipe produces cold gas fractions far lower than the fiducial model at low redshift. To implement the direct star formation suppression, we multiply the constant star formation efficiency recipe by a factor, $f_{\rm DS}$. The inefficiency parameter $f_{\rm DS}$ can be made a function of galaxy mass and redshift and allows us to directly control the star formation rate. This has the same effect as making the star

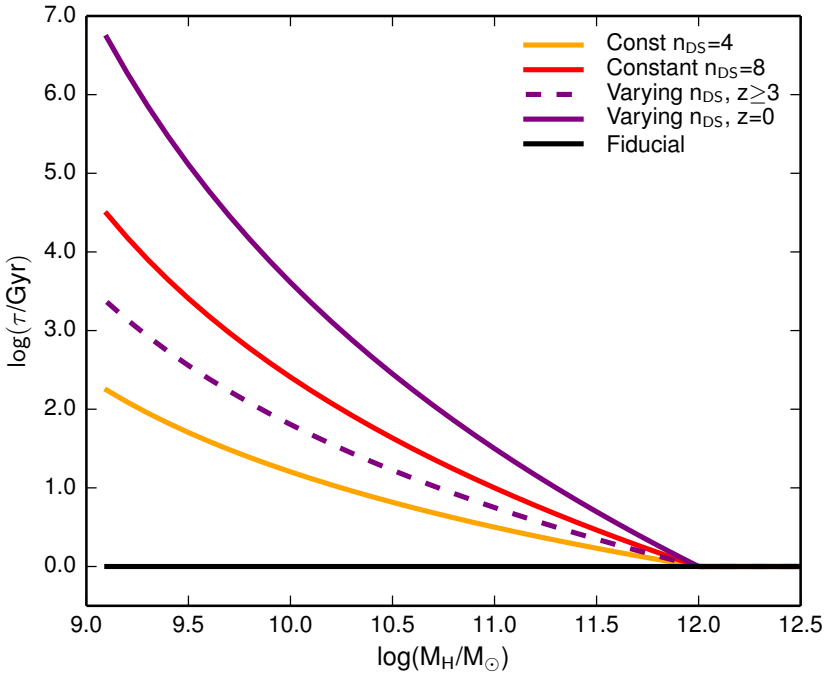

Figure 2.14: Star formation timescale, $\tau_{\rm DS}(M_{\rm H}, z) \equiv \tau_{\rm CE}/f_{\rm DS}$, for three variants of the direct suppression model. The two constant $n_{\rm DS}$ models are shown in yellow and red and the varying $n_{\rm DS}$ model is shown in purple with the $z = 0$ relation as a solid line and the $z = 3$ relation as a dashed line.

formation timescale a function of mass and redshift, $\tau_{\rm DS}(M_{\rm H}, z)$.

$$\dot{M}_\star = f_{\rm DS}(M_{\rm H}, z)\frac{M_{\rm cold}}{\tau_{\rm CE}} = \frac{M_{\rm cold}}{\tau_{\rm DS}(M_{\rm H}, z)} \tag{2.6}$$

The function $f_{\rm DS}$ effectively replaces the surface density threshold for star formation in our fiducial model.

The direct suppression factor $f_{\rm DS}$ should be unity above a certain halo mass, $M_{\rm H,trans}$, since high mass halos should remain unaffected, and halos with $M_{\rm halo} \lesssim 10^{11}$ $M_\odot$ should have low $f_{\rm DS}$ to prevent overproduction of stars. To parameterize this, we

set $f_{\rm DS}$=0 at $M_{\rm halo}\leq 10^8\ M_\odot$, $f_{\rm DS}$=1 at $M_{\rm halo}\geq M_{\rm H,trans}$, and a power law between with power $n_{\rm DS}$.

$$f_{\rm DS} = \begin{cases} 0 & M_{\rm H} \leq 10^8 M_\odot \\ \left(\frac{\log(M_{\rm H})-8}{\log(M_{\rm H,trans})-8}\right)^{n_{\rm DS}} & 10^8 M_\odot < M_{\rm H} < M_{\rm H,trans} \\ 1 & M_{\rm H} \geq M_{\rm H,trans} \end{cases} \tag{2.7}$$

We take $M_{\rm H,trans} = 10^{12}\ M_\odot$. Low mass halo properties are fairly insensitive to the choice of $M_{\rm H,trans}$. This relation is shown for the three models we present in terms of the direct suppression timescale $\tau_{\rm DS}(M_{\rm H}, z)$ rather than $f_{\rm DS}$ itself in Figure 2.14. A low constant $n_{\rm DS}$=4 follows the fiducial $f_\star$ closely at low redshifts with only a slight decrease in normalization towards redshift $z = 3$, as can be seen in the left panel of Figure 2.15. A higher constant $n_{\rm DS}$=8 also reproduces the $z = 0$ $f_\star\,(M_{\rm halo})$ relation and does somewhat better than the fiducial model at redshifts $z = 1$ and 2, though it is still outside the 1-σ uncertainty at $z \sim 1$. At $z = 1$ and $z = 2$, $n_{\rm DS}$=8 still overproduces stellar mass in halos of mass $M_{\rm halo}\cong 10^{11}\ M_\odot$ and at high redshifts, star formation is over-suppressed, producing a $z = 3$ $f_\star\,(M_{\rm halo})$ below observations. The $n_{\rm DS}$=8 model does reproduce the sense of the $M_{\rm halo}\cong 10^{10}\ M_\odot$ $f_\star$(z) relation. These same trends can be seen in the stellar mass functions in Figure 2.16. Increasing $n_{\rm DS}$ beyond $n_{\rm DS}$=8 would bring the redshift $z = 1$ and 2 $f_\star$ relations closer to observations, but would make the discrepancy at higher redshifts worse. Moreover, none of the

models with constant $n_{\rm DS}$ reproduce the observed cold gas fractions at $z = 0$ (Figure 2.17) or correctly predict the observed slope in the sSFR-$M_\star$ relation at $z = 0$ (Figure 2.18). The $n_{\rm DS}$=8 model does produce a rising metallicity over time for the lowest mass galaxies, but the metallicity evolution is still too weak (Figure 2.19).

In the limit of very high $n_{\rm DS}$, our model is reminiscent of the Bouché et al. (2010) model, but with the major difference that accretion itself is halted in the Bouché et al. (2010) model and only star formation is halted in ours. Our direct suppression model with $n_{\rm DS}$ very high is approximately a step function as is the Bouché et al. (2010) accretion floor, but with a transition mass of $M_{\rm halo}$=10^{12} $M_\odot$ instead of 10^{11} $M_\odot$. The step function fails in our model because we are only preventing star formation, not gas accretion, and as soon as a galaxy passes the threshold, it quickly forms enough stars to rejoin the fiducial $f_\star\,(M_{\rm halo})$.

In an attempt to bring the $f_\star\,(M_{\rm halo})$ relation at $z = 1$ and 2 into closer agreement with the observations, we try a model with constant $n_{\rm DS}$=6 at $z > 3$, then increase $n_{\rm DS}$ to $n_{\rm DS}$=12 linearly between $z = 3$ and $z = 0$. This model matches $f_\star$ at $z \sim 3$ acceptably and matches well at $z = 0$, but still over-predicts the $z = 1$ and $z = 2$ $f_\star$ relations. Our varying $n_{\rm DS}$ model over-predicts cold gas fractions for stellar masses $M_\star \lesssim 10^9$ $M_\odot$ at all redshifts and at stellar masses $M_\star \lesssim 10^{10}$ $M_\odot$ for $z \gtrsim 2$. It does produce a slightly negative sSFR slope at $z = 0$ but still does not match the observed normalization.

In terms of the star formation timescale, our models have a normal, constant star

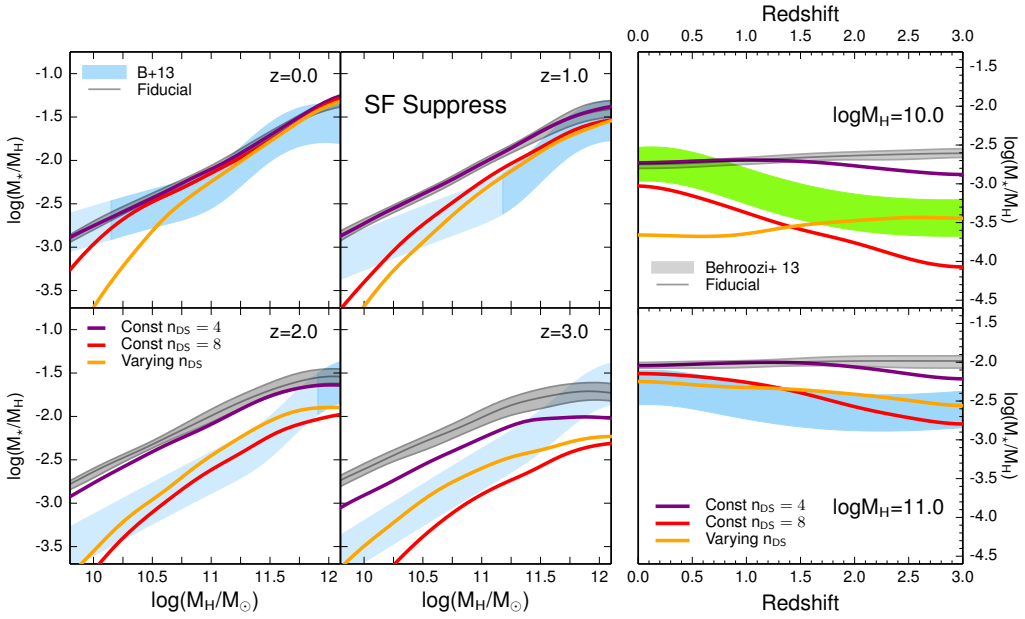

Figure 2.15: Ratio of stellar mass to halo mass, $f_\star$, for the three direct star formation suppression models. In all panels, the three direct suppression models are shown in yellow, red, and purple and the median and $\pm1\sigma$ region of the fiducial model are shown in gray. **Left panel:** the $f_\star\,(M_{\rm halo})$ relation for four redshifts. **Right panel:** $f_\star$(z) for halo mass $M_{\rm H} = 10^{10}\ M_\odot$ in the top panel and halo mass $M_{\rm H} = 10^{11}\ M_\odot$ in the lower panel. Empirical constraints (shaded colored regions) are as described in Figure 2.1.

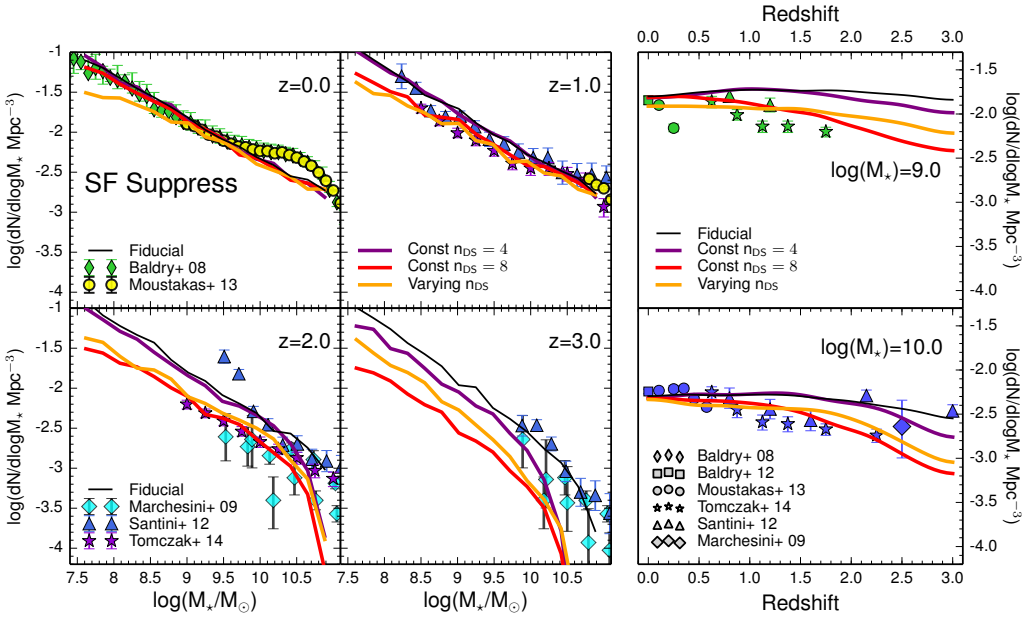

Figure 2.16: Stellar mass function for the direct star formation suppression model. In all panels, the direct suppression models are shown in yellow, red, and purple, and the fiducial model is shown in black. Data are as in Figure 2.2. **Left panel:** stellar mass functions for four redshifts. **Right panel:** number densities as a function of redshift for galaxies with $M_\star$= 10^9 $M_\odot$ in the top panel and $M_\star$= 10^{10} $M_\odot$ in the lower panel.

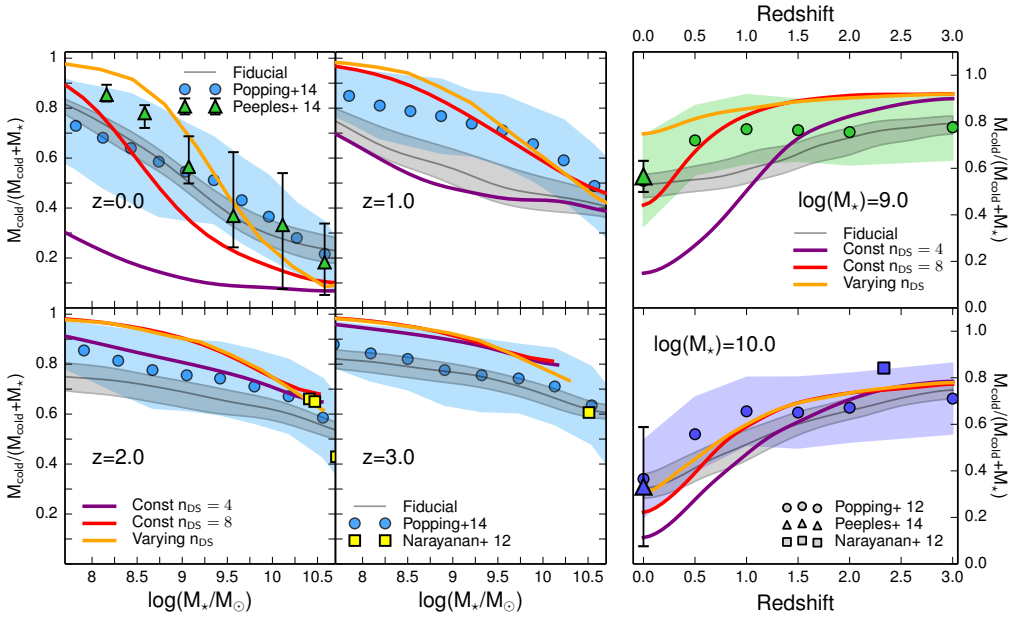

Figure 2.17: Cold gas fractions for the three direct suppression models. In all panels, the direct suppression models are shown in yellow, red, and purple, and the median and $\pm1\sigma$ region of the fiducial model are shown in gray. Data are as in Figure 2.3. **Left panel:** cold gas fractions as a function of stellar mass for four redshifts. **Right panel:** cold gas fraction as a function of redshift for galaxies with stellar mass $M_\star$= 10^9 $M_\odot$ in the top panel and $M_\star$= 10^{10} $M_\odot$ in the lower panel. Only model galaxies with nonzero gas fraction and bulge to total ratio B/T<0.4 are included.

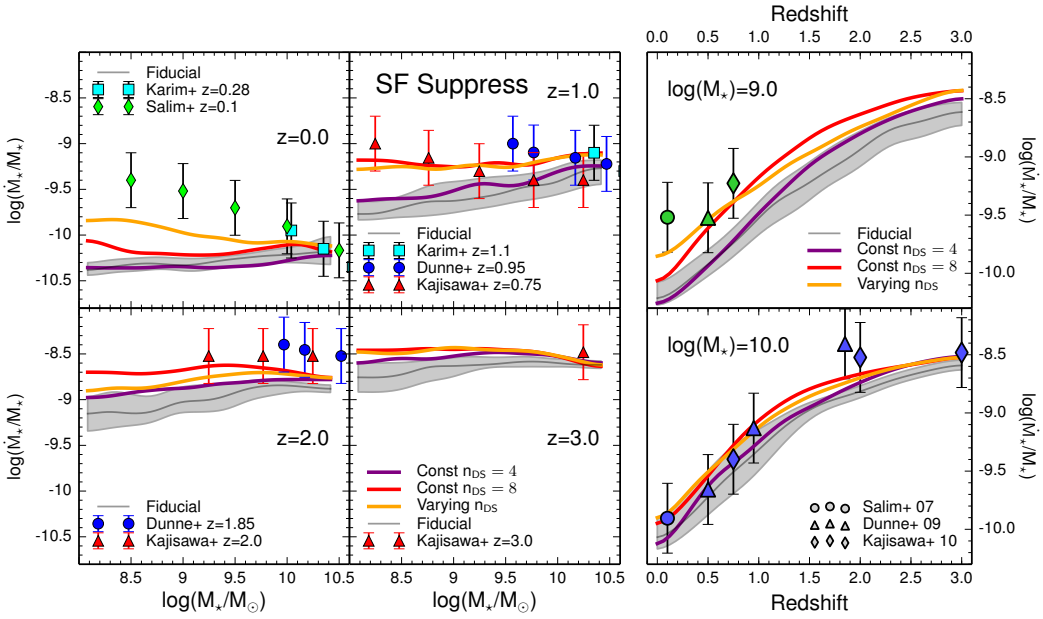

Figure 2.18: Specific star formation rates for the three direct suppression models. In all panels, the direct suppression models are shown in yellow, red, and purple, and the median and $\pm1\sigma$ region of the fiducial model are shown in gray. Data are as in Figure 2.4. **Left panel:** sSFRs as a function of stellar mass at four redshifts. **Right panel:** sSFR as a function of redshift for $M_\star = 10^9\ M_\odot$ in the top panel and $M_\star = 10^{10}\ M_\odot$ in the lower panel.

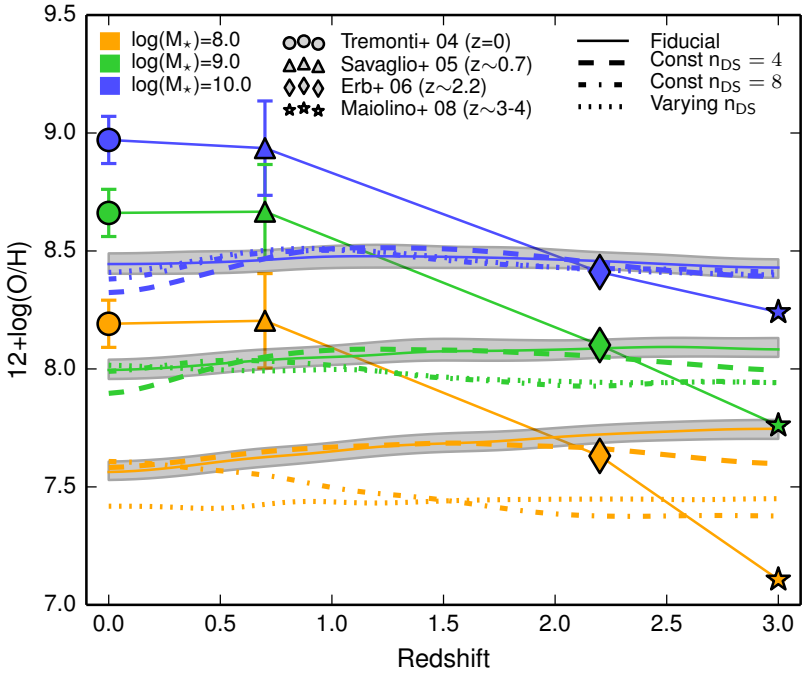

Figure 2.19: Gas phase metallicities in the three direct suppression models for selected stellar masses as a function of redshift. Metallicities are color coded according to the stellar mass bin they represent. The thin solid lines and shaded gray regions show the fiducial model's median and $\pm 1\sigma$ region and the thick dashed, dotted, and dot-dashed lines show the direct suppression models. Only galaxies with gas fractions greater than 0.2 are plotted and observations are shown as points whose shapes indicate which data set they represent.

formation timescale above the transition halo mass $M_{\rm H} \cong 10^{12}\ M_\odot$ and transition quickly to a very long star formation timescale below (see Figure 2.14). By adjusting $n_{\rm DS}$, we control how quickly the star formation timescale increases below $M_{\rm H} \cong 10^{12}\ M_\odot$ and thus how suppressed star formation is in low mass halos. The way in which the model with varying $n_{\rm DS}$ failed suggests that monotonically increasing how steeply the star formation timescale rises below the transition mass is insufficient. The transition to very long star formation timescales would most likely need to be extremely quick between $z = 3$ and $z = 1$ to match $f_\star$ at redshifts $z = 1$ and 2, but must ease off towards $z = 0$ in order not to over-suppress star formation at $z = 0$. A successful direct suppression model would likely add at least four new free parameters and the physical scenario that could cause this sort of behavior is not obvious. The failure of the direct suppression model highlights the resilience of the low mass galaxies' star formation histories against changes in the star formation efficiency, and suggests that the solution is unlikely to consist solely of adjustments to the star formation efficiency.

2.5.3 Parking lot: changing gas accretion rates

Every halo has three reservoirs of gas: cold ISM gas in galaxies, hot halo gas (ICM), and "ejected" gas, which may be associated with the circum-galactic medium (CGM) or IGM. Halos grow by accreting "diffuse" material that has never been in halos, as well as by subsuming material from all of the progenitor halos. One must

decide how to combine these different reservoirs. In the Santa Cruz SAM, all galaxies keep their cold gas reservoirs and the hot gas from halos that become satellites is assumed to be instantaneously subsumed into the hot gas reservoir of the new halo. The ejected gas reservoir from the largest progenitor halo becomes the ejected gas reservoir for the new halo, and the ejected gas reservoirs from the other (minor) progenitors are deposited into the *hot gas reservoir* of the new central halo. The ejected gas reservoirs also include IGM gas that was prevented from accreting by the photo-ionizing background; for the non-largest progenitors this is also subsumed into the new hot gas reservoir of the larger halo.

We found that, within the usual set of assumptions of our fiducial model, simply changing the functional form of the re-infall timescale (Equation 2.1) did not solve the dwarf galaxy problems we are trying to address here. We discuss reasons for this, and possible reasons for differences between our results and those of Henriques et al. (2013), in Section 2.6. Briefly, we find that the significance of "re-accreted" gas to the total gas supply is quite sensitive to details of the bookkeeping for these different gas reservoirs when halos merge together. The SAM used in the H13 model takes gas stripped from the ejected reservoir of an in-falling satellite and deposits it over time in the ejected reservoir of the central, whereas the fiducial Santa Cruz model instantaneously deposits all the gas from the ejected reservoir of the satellite into the hot gas reservoir of the new central. This difference means that the H13 model's ejected reservoir handles a higher fraction of the galaxy's gas than the Santa Cruz

model's and therefore changing the re-infall timescale in the H13 model has a larger effect than in the Santa Cruz model.

In the parking lot model, we divert some of the gas that would normally be added directly to the hot gas reservoir and instead store it along with the ejected gas. This reservoir of ejected and diverted gas becomes our parking lot. We then adopt various scalings for the timescale on which this parking lot gas can accrete into the halo. With the addition of the diverted gas, changing the rate of infall from this parking lot reservoir can affect the evolution of galaxies' stellar masses at higher redshifts.

Before we choose how to alter the accretion timescale for the parking lot gas, we must choose which gas is routed through the parking lot. We found that when we diverted all the accreted gas to the parking lot, our models produced an incorrect evolution similar to the fiducial model with star formation happening too early in low mass galaxies and too late in high mass galaxies. It may be the case that if we made the parking lot accretion timescale a complex function of halo mass and redshift, such models could be made to work, however, this is beyond the scope of this work. We found, though, that if we divert only the hot and ejected gas reservoirs from the minor progenitors following halo mergers, this has little effect on accretion at high redshift (where it is dominated by accretion from the IGM), but delays lower redshift accretion as required. Considering that numerical simulations find that satellites' dark matter halos begin being stripped at $5R_{\rm vir}$ (Behroozi et al., 2014), it is perhaps not unreasonable to think that the associated hot diffuse gas might also be stripped

and heated by the ejected reservoir.

The infall timescale must depend on halo mass in order to create a differential between low mass and high mass halos. We let the timescale be proportional to the virial mass to a power:

$$\dot{M}_{\rm ReIn} = M_{\rm PL}/\tau_{\rm PL} \tag{2.8}$$

$$\tau_{\rm PL} = \gamma_{\rm PL}\left(\frac{M_{0,\rm PL}}{M_{\rm vir}}\right)^{\alpha_{\rm PL}} \tag{2.9}$$

where we choose $M_{0,\rm PL} = 10^{10}\ M_\odot$. Oppenheimer et al. (2010) find that in their hydrodynamic simulations, the gas recycling timescale (which in their case is the time between gas ejection and re-infall into the ISM) scales as $\alpha_{\rm PL}$=0.5 for momentum-driven winds or $\alpha_{\rm PL}$=1.5 for energy-driven, constant velocity winds. Note that our timescale is that for reaccretion only, not the timescale for the full cycle of ejection and reaccretion as in Oppenheimer et al. (2010).

We test all three values of $\alpha_{\rm PL}$ with $\gamma_{\rm PL}$=10^{11} yr and $M_{0,\rm PL} = 10^{10}\ M_\odot$. The re-infall timescales for these three models as a function of halo mass are shown in Figure 2.20. The results are insensitive to the exact values chosen for $\gamma_{\rm PL}$ and $M_{0,\rm PL}$. Increasing $M_{0,\rm PL}$ by two orders of magnitude somewhat decreases the normalization of $f_\star$ for intermediate mass halos and changing $\gamma_{\rm PL}$ by an order of magnitude changes the normalization of $f_\star$ by less than half a dex. Other properties are essentially unaffected. The $\alpha_{\rm PL}$=1 model is able to produce a gently rising value of $f_\star$ at $M_{\rm H} \geq 10^{11}\ M_\odot$,

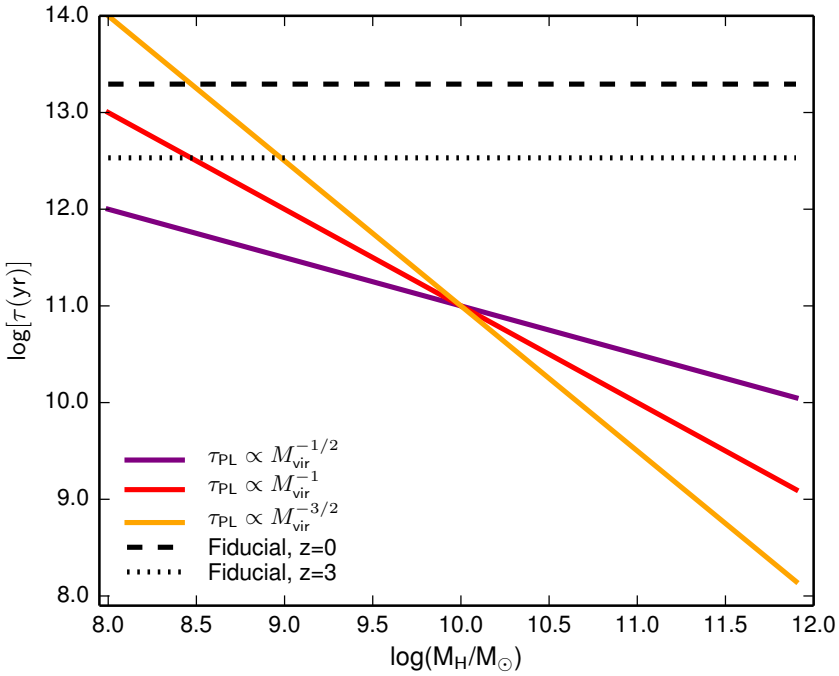

Figure 2.20: Re-infall timescales as a function of halo mass for the three parking lot models as well as the fiducial model. The fiducial model's infall timescale depends on redshift because it is a function of the dynamical time of the halo at the virial radius, which changes with redshift.

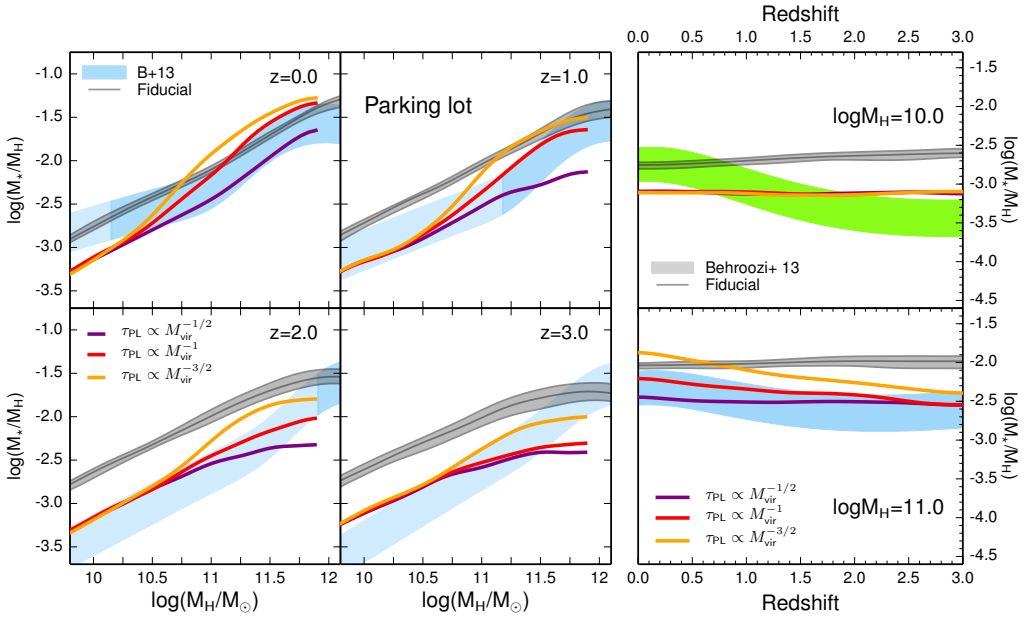

Figure 2.21: Ratio of stellar mass to halo mass, $f_\star$, for the three parking lot models. In all panels, the parking lot models are shown in yellow, red, and purple, and the median and $\pm 1\sigma$ region of the fiducial model are shown in gray. **Left panel:** $f_\star\,(M_{\rm halo})$ relation for four redshifts. **Right panel:** $f_\star$(z) for halo mass $M_{\rm H} = 10^{10}\ M_\odot$ in the top panel and halo mass $M_{\rm H} = 10^{11}\ M_\odot$ in the lower panel. Empirical constraints (shaded colored regions) are as described in Figure 2.1.

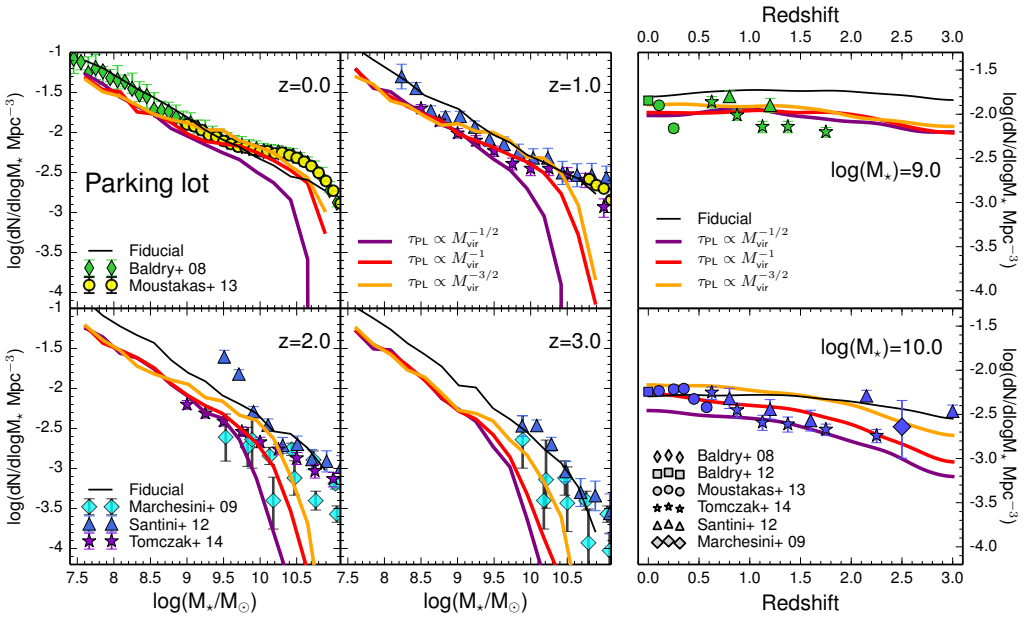

Figure 2.22: Stellar mass functions for the parking lot models. In all panels, the parking lot models are shown in yellow, red, and purple, and the fiducial model is shown in black. Data are as in Figure 2.2. **Left panel:** stellar mass functions for four redshifts. **Right panel:** number densities as a function of redshift for galaxies with $M_\star = 10^9\ M_\odot$ in the top panel and $M_\star = 10^{10}\ M_\odot$ in the lower panel.

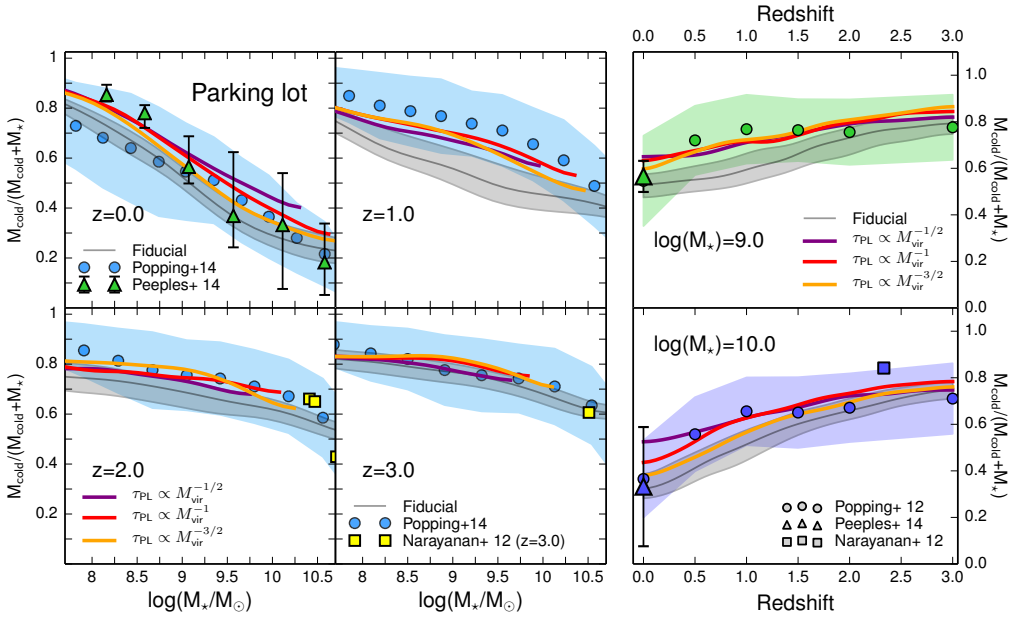

Figure 2.23: Cold gas fractions for the parking lot models. In all panels, the parking lot models are shown in yellow, red, and purple, and the median and $\pm1\sigma$ region of the fiducial model are shown in gray. Data are as in Figure 2.3. **Left panel:** gas fraction as a function of stellar mass for four redshifts. **Right panel:** gas fraction as a function of redshift for galaxies with stellar mass $M_\star = 10^9\ M_\odot$ in the top panel and $M_\star = 10^{10}\ M_\odot$ in the lower panel. Only galaxies with nonzero gas fractions and bulge to total ratios B/T<0.4 are shown.

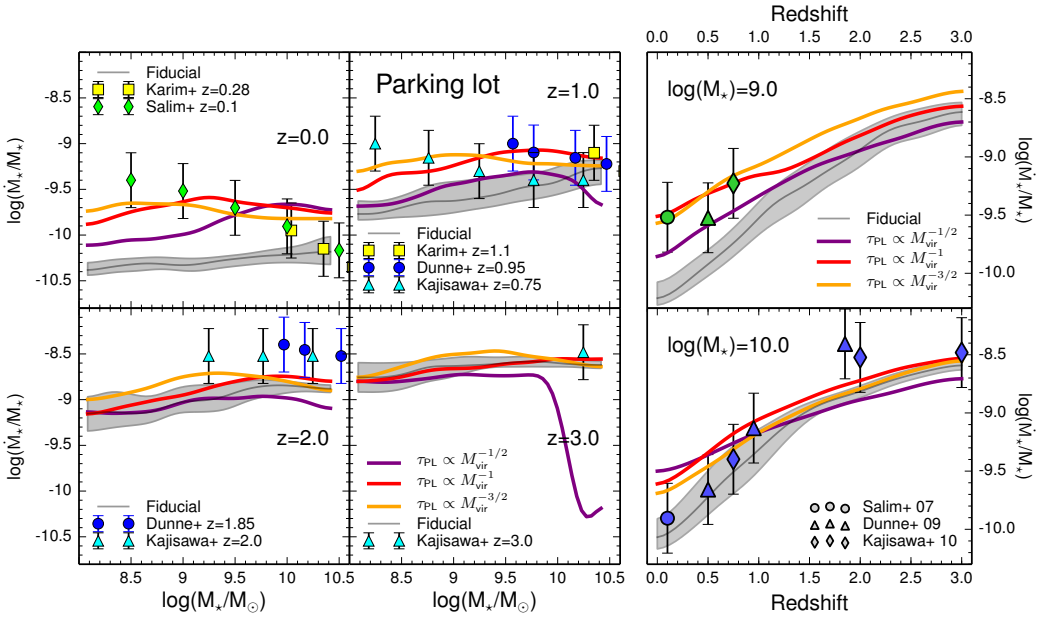

Figure 2.24: Specific star formation rates for the three parking lot models. In all panels, the parking lot models are shown in yellow, red, and purple, and the median and $\pm 1\sigma$ region of the fiducial model are shown in gray. Data are as in Figure 2.4. **Left panel:** sSFR as a function of stellar mass for four redshifts. **Right panel:** sSFR as a function of redshift for $M_\star = 10^9\ M_\odot$ in the top panel and $M_\star = 10^{10}\ M_\odot$ in the lower panel.

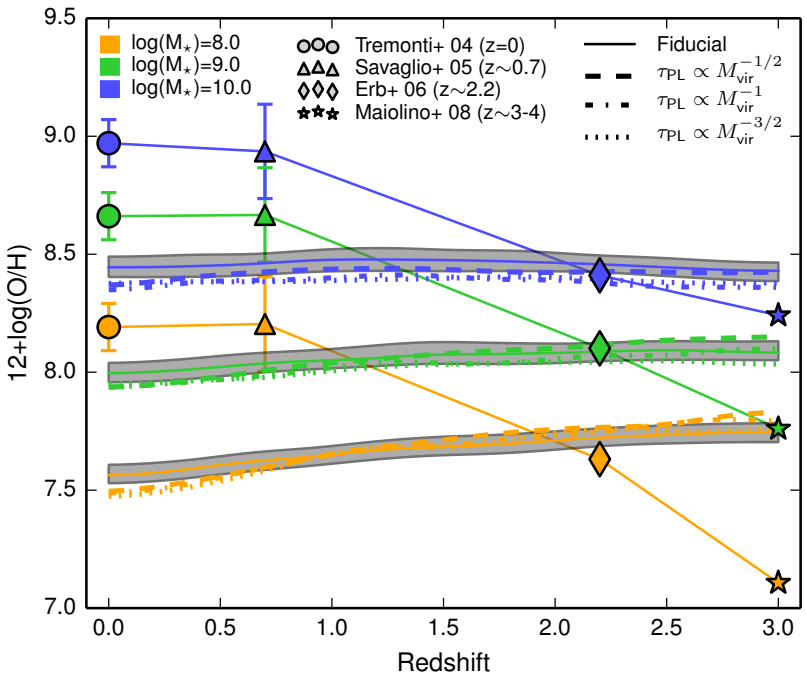

Figure 2.25: Gas phase metallicities for the three parking lot models for selected stellar masses as a function of redshift. Metallicities are color coded according to the stellar mass bin they represent. The fiducial model is shown with thin solid lines and the three parking lot models are shown as dashed, dot-dashed, and dotted lines. Only galaxies with gas fractions greater than 0.2 are plotted and observations are shown as points whose shapes indicate which data set they represent, as in Figure 2.5.

with a similar slope to the Behroozi et al. (2013a) results, but $f_\star$ at $M_{\rm H} \geq 10^{10}$ $M_\odot$ remains flat (Figure 2.21). In addition, the parking lot models appear to over-suppress star formation in halos with $M_{\rm H} \geq 10^{11.5}$ $M_\odot$ at $z = 2$ and $z = 3$. This problem would only be exacerbated by turning AGN feedback back on. In order to improve the $f_\star$ results further, it appears that it would be necessary to introduce a more complicated redshift and halo mass dependence for $\tau_{\rm PL}$. We note that in the results shown here, there is no suppression of gas infall or evaporation of cold gas by the photo-ionizing background included in our models. This is important at the lowest halo masses considered ($M_{\rm H} \lesssim 10^{10}$).

Predicted cold gas fractions are slightly higher at high redshift (see Figure 2.23), matching the Popping et al. (2014a) well at most redshifts. The $z = 1$ gas fractions remain somewhat low but are within the $\pm 1\sigma$ errors of the empirical model. The low mass slope of the sSFR vs. stellar mass relation is significantly improved, now lying within the observational error bars except at the lowest masses for $z \lesssim 1$ (Figure 2.24). The ISM metallicity evolution remains very similar to that in the fiducial model (see Figure 2.25).

2.6 Comparison with the results of Henriques et al. (2013)

Henriques et al. (2013, H13) also addressed the problems models have with repro-

ducing low mass galaxy properties in a way similar to our parking lot model. They made use of Monte Carlo Markov Chains (MCMC) coupled with the Guo et al. (2011) semi-analytic model, and found that no single set of parameters could simultaneously reproduce the abundances of low mass galaxies at all redshifts. They found, however, that changing the halo mass and time dependence of the timescale for the re-infall of ejected gas significantly improved the agreement between their model and the B- and K-band luminosity function from $z \sim 0$–3 as well as the stellar mass function. Specifically, they proposed the revised scaling:

$$\dot{M}_{\rm ReIn} = \left(\frac{M_{\rm eject}}{t_{\rm ReIn}}\right) \tag{2.10}$$

with

$$t_{\rm ReIn} = -\gamma_{\rm ReIn}\left(\frac{10^{10}M_\odot}{M_{\rm H}}\right) \tag{2.11}$$

where the constant $\gamma_{\rm ReIn}$ has dimensions of time. The re-infall timescale is now an explicit function of halo mass but not of time or redshift, while previously it was a function of redshift but not explicitly of halo mass. The previous form, Equation 2.1, depends on the halo dynamical time, which is independent of halo mass but depends on cosmic time; halos that form at high redshift are denser and have a smaller dynamical time for a given mass. Low mass halos now take longer to re-accrete their ejected gas (see Figure 2.20). As pointed out by H13, this is in qualitative agreement with the wind return scalings found in some numerical hydrodynamic simulations

(e.g. Oppenheimer et al., 2010).

We implemented the revised re-accretion timescale functional form above in our fiducial SAM by simply replacing Equation 2.1 with Equations 2.10 and 2.11, but found that this did not improve our predictions for $f_\star$ or the comoving number density of low mass galaxies; instead, it had very little effect on these quantities. The results are shown in Figure 2.26 and Figure 2.27, labeled 'Ejected $\rightarrow$ hot' (the reason for this label will be explained presently). In order to understand why our model behaves differently, we conducted several experiments. We found that we could get behavior similar to that reported by H13 by changing the bookkeeping for the ejected gas reservoirs of non-largest progenitors following halo mergers. In our fiducial model, as published in S08, S12 and elsewhere, when halos merge the gas in the ejected reservoir of the largest progenitor halo becomes the ejected reservoir of the new halo and the ejected reservoirs of all other halos are deposited in the *hot gas* reservoir of the new halo. In addition, all the gas in the hot reservoirs of the non-largest progenitors is assumed to be instantaneously stripped and added to the hot gas reservoir of the new host halo, where it is only allowed to accrete onto the central galaxy from then on. The hot and ejected gas in these non-largest progenitor halos is a significant component of the total accretion budget, particularly at late times.

In the H13 models, both the hot and ejected gas from non-largest progenitors remains bound to the halos even after they become satellites in the new halo. These hot and ejected reservoirs are then stripped from the satellites on timescales dictated

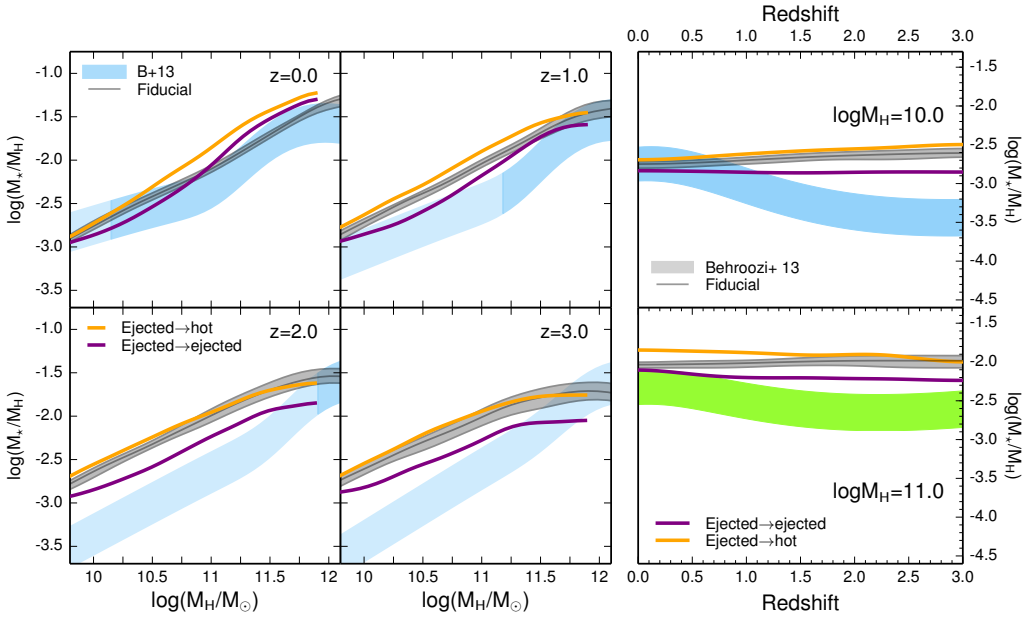

Figure 2.26: Ratio of stellar mass to halo mass, $f_\star$, for our implementation of the H13 model with in-falling satellites' gas handled in two ways. In all panels, the fiducial model's median and $\pm1\sigma$ region are shown in gray and our H13-like models are shown in yellow for the default handling of satellites' ejected reservoirs and purple for gas in satellites' ejected reservoirs being deposited in the central's ejected reservoir. **Left panel:** $f_\star\,(M_{\rm halo})$ relation for four redshifts. **Right panel:** $f_\star$(z) for halo mass $M_{\rm H} = 10^{10}\ M_\odot$ in the top panel and halo mass $M_{\rm H} = 10^{11}\ M_\odot$ in the lower panel. Empirical constraints (shaded colored regions) are as described in Figure 2.1.

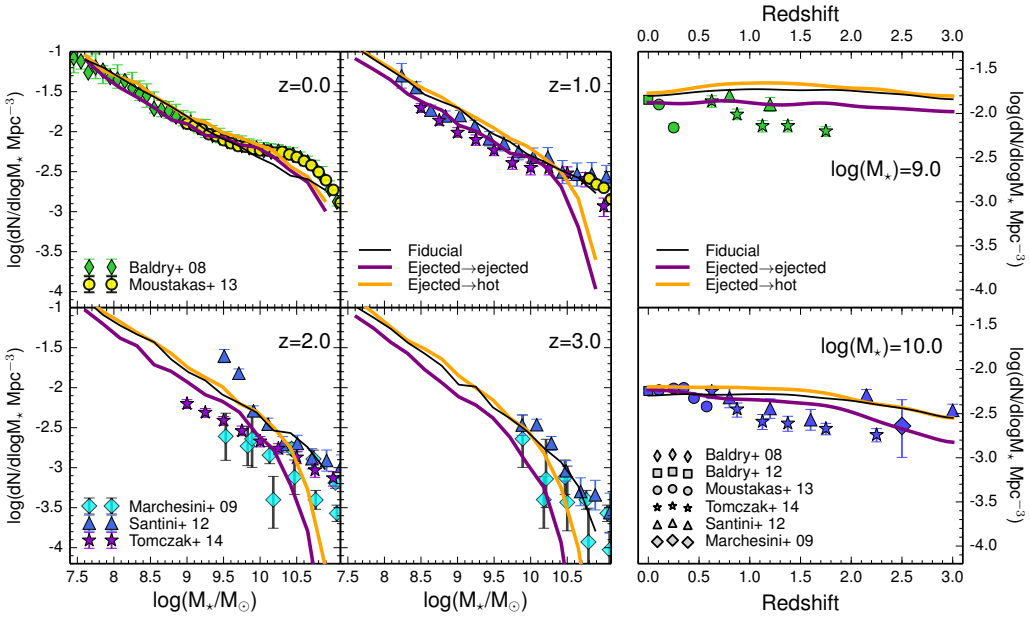

Figure 2.27: Stellar mass functions for our implementation of the H13 model with satellite gas handled two different ways. In all panels, the fiducial model is shown in black and our H13-like models are shown in yellow for the default handling of satellites' ejected reservoirs and purple for gas in satellites' ejected reservoirs being deposited in the central's ejected reservoir. **Left panel:** stellar mass function for four redshifts. **Right panel:** galaxy number density as a function of redshift for galaxies with $M_\star = 10^9\ M_\odot$ in the top panel and $M_\star = 10^{10}\ M_\odot$ in the lower panel. Data are as described in Figure 2.2.

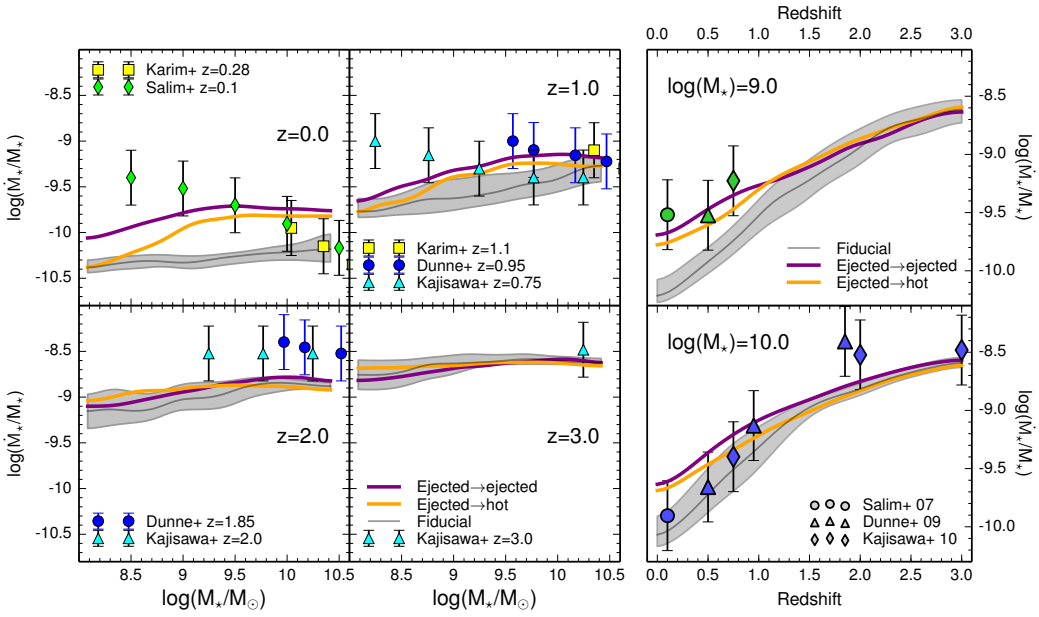

Figure 2.28: Specific star formation rates for our implementation of the H13 model with satellite gas treated two different ways. In all panels, the fiducial model's median and $\pm 1\sigma$ region are shown in gray and our H13-like models are shown in yellow for the default handling of satellites' ejected reservoirs and purple for gas in satellites' ejected reservoirs being deposited in the central's ejected reservoir. **Left panel:** sSFR as a function of stellar mass for four redshifts. **Right panel:** sSFR as a function of redshift for $M_\star = 10^9\ M_\odot$ in the top panel and $M_\star = 10^{10}\ M_\odot$ in the lower panel. Data are as described in Figure 2.4.

by tidal and ram pressure stripping. The stripped gas from the satellites' hot reservoir is added to the central's hot reservoir, and the stripped gas from the ejected reservoir is added to the central's ejected reservoir (B. Henriques 2014, private communication; see also Guo et al. 2011). When we made the alternate assumption that the ejected reservoirs are added to the new host's ejected reservoir when halos become satellites, as well as adopting the revised reaccretion timescale, we find that the comoving number density of galaxies with stellar masses $M_\star \sim 10^9$–10^{10} $M_\odot$ decreases relative to our fiducial model by about 0.25 dex at $z \sim 1$–2, consistent with the findings of H13 (see Figure 2.27, 'Ejected $\rightarrow$ ejected'). In this model, we find that $f_\star$ is roughly flat from $z \sim 3$ to 0 at a halo mass of $M_H \sim 10^{11}$, and is still decreasing (rather than increasing) at lower halo mass $M_H \sim 10^{10}$ $M_\odot$. This is also consistent with the results shown by H13, in which the SMF in their modified model is changed only over a limited range in stellar mass, and steepens again to match the unmodified slope at masses $M_\star \lesssim 10^9$ $M_\odot$.

H13 do not show the sSFR as a function of stellar mass, but they do show that the peak in sSFR in the stellar mass range 10^9 $M_\odot < M_\star < 10^{9.5}$ $M_\odot$ shifts to higher sSFR, in better agreement with observations. This is consistent with the results from our "H13-like" model; however, we find that the sSFR decreases again at $M_\star \lesssim 10^9$ $M_\odot$, in conflict with observations of nearby galaxies (see Figure 2.28). H13 do not show predictions for cold gas fractions nor the evolution of the mass-metallicity relation in their model. We find that the cold gas fractions at $z \sim 0.5$–1 and $M_\star \gtrsim 10^8$ $M_\odot$ are

about 20% higher in our H13-like model, and that the mass-metallicity evolution is not significantly different from the fiducial model.

2.7 Conclusions

The overarching theme of our study is that the interplay between gas accretion, feedback, and star formation as commonly implemented in ΛCDM models of galaxy formation results in a remarkable tendency to produce the "upsizing" behavior seen in the fiducial model. Models find that the $f_\star$ and number density of low mass galaxies is approximately constant or even *decreases* instead of following the increase with cosmic time implied by observations. This is probably due to the failure of "sub-grid" recipes for star formation and stellar feedback to break the characteristic self-similarity of halos' gas and dark matter accretion histories. It has been clear for some time that some modification needs to be made to the sub-grid recipes in order to solve the cluster of problems that constitutes the "dwarf galaxy conundrum" presented here, assuming that the basic framework is correct. However, it has remained unclear which set of physical recipes needs to be modified or in what way.

In order to try to gain insight into this puzzle, we have considered a broader set of complementary observables than have been presented in most previous studies. In addition, we have considered three very physically different classes of solution. Some previous works (e.g. Lu et al., 2015) have distinguished between "ejective"

feedback versus "preventative" feedback. Ejective feedback prevents star formation by ejecting cold gas and making it unavailable for forming stars, whereas preventative feedback prevents hot or in-falling gas from cooling and becoming available for star formation. All of our models use ejective feedback, though the parking lot model could be interpreted as having both ejective and preventative feedback. We show that the different classes of solution, when tuned to match the qualitative behavior of $f_\star$, make different predictions for other observables. For example, the direct suppression model produced a larger change in galaxy cold gas fractions at high redshift than other models, while the parking lot model produced a greater change in the low mass slope of the sSFR-$M_\star$ relationship. Interestingly, *none* of the scenarios that we studied were able to reproduce the observed trend of strongly increasing gas phase metallicities at fixed stellar mass with cosmic time, suggesting that this problem may have a different origin and solution if the metallicity trend with redshift is to be believed. Additionally, the fiducial implementation of squelching as in S08 and S12 used in the altered recipes can decrease or reverse the corrected "sub-grid" recipes' trend of increasing $f_\star$ with time.

Given the freedom that we allowed ourselves in parameterizing the empirical recipes, it is perhaps not too surprising that we were able to find solutions that qualitatively reproduced the increasing trend of $f_\star$ and comoving number density of low mass galaxies with cosmic time for all three scenarios (see Figure 2.29 for a summary of all the scenarios, using the directly observable metric of galaxy number

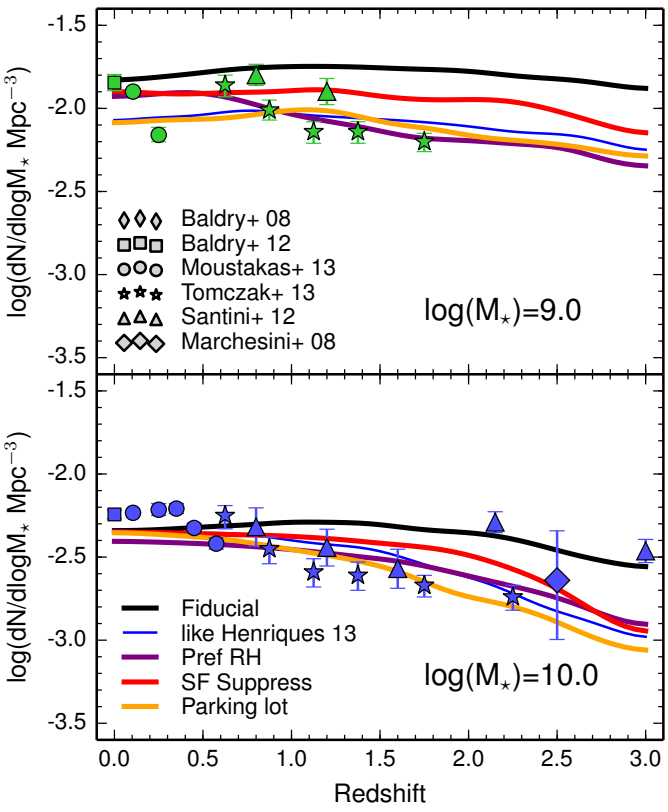

Figure 2.29: Galaxy number densities as a function of redshift for galaxies with $M_\star = 10^9\ M_\odot$ in the top panel and $M_\star = 10^{10}\ M_\odot$ in the lower panel. The fiducial model is shown in black, the "H13-like" version of our SAM described in Appendix 2.6 in blue, and the "best" versions of each modified scenario are shown with preferential reheating in purple, direct suppression with varying $n_{\rm DS}$ in red, and parking lot with $\tau_{\rm PL} \propto M_{\rm vir}^{-1}$ in yellow. Observations are shown as points whose shapes indicate which data set they represent. Data are as in Figure 2.2.

density as a function of redshift). What is then interesting is to try to assess how physically plausible the required scalings are. The preferential reheating model gave perhaps the best results overall, but requires a fairly extreme change in the slope of the mass-loading factor, $\alpha_{\rm RH}$, from $\alpha_{\rm RH}\sim$ 4.5 at high redshift to $\alpha_{\rm RH}\sim$ 2 at low redshift. While there are physical reasons to think that this scaling might have an effective redshift dependence, as discussed above, it is unclear whether such a strong evolution in the scaling can find a physical basis. The direct suppression model requires an even more extreme scaling — the star formation efficiency or timescale must vary with halo mass as a power-law with a slope of ~ 8 (almost a step function). This would seem to be already ruled out by direct observations of star formation efficiencies in nearby galaxies, which do not vary by orders of magnitude (e.g. Bigiel et al., 2008). We therefore disfavor the direct suppression scenario as the primary solution to the dwarf galaxy problem. The parking lot model was not quite as successful as the preferential reheating model, but it did push the qualitative behavior in the right direction, and the variations in the recipes are easily within the uncertainties in our knowledge of the relevant physical processes. Our parking lot model is very similar in spirit to the H13 model, which by modifying the re-infall time for ejected gas was also quite successful at solving many of the problems we have highlighted here. However, we have pointed out that somewhat arbitrary choices in how ejected gas is handled in SAMs can have a large effect on the results. Although here we have only considered solutions driven by one of the three physical scenarios, it is entirely

possible that more than one of the kinds of variations we considered are important. In particular, modified scalings for the mass-loading factor and the re-accretion time of ejected gas are likely to be interconnected through the detailed microphysics of stellar-driven winds.

It is also important to consider the possibility that some or all of the observational data that have been used as constraints are not correct. There are currently differences in galaxy stellar mass function normalization that are comparable to the level of discrepancy that we are discussing here, which is only factors of a few and not orders of magnitude. Uncertainties on this level can arise from field-to-field variance and systematic uncertainties in stellar mass estimates. These will improve in the next few years as large areas are surveyed to the depth necessary to probe these low mass objects out to redshifts of $z \sim 1$–2. Similarly, direct estimates of cold gas fractions in low mass galaxies at high redshift are currently unfeasible, but this will change in the near future as the next generation of radio telescopes comes online. However, even with uncertainty in the observations we compare to, the fundamental disagreement in star formation histories remains. Present-day low mass galaxies are bluer and more star-forming than models predict and these adjusted models are a step in the right direction.

In summary, in this chapter we investigated three classes of empirical solution to the "dwarf galaxy conundrum," the mismatch of observed and predicted star formation histories for galaxies forming in low mass dark matter halos. The three scenarios

involve (1) changing the halo mass dependence of the mass outflow rate of stellar–driven winds as a function of redshift, (2) changing the star formation efficiency as a function of halo mass and redshift, and (3) trapping accreting gas in a "parking lot" reservoir with a halo mass-dependent infall timescale. We compared the predictions of the three scenarios to observational estimates of the ratio of stellar mass to halo mass, SMF, sSFR, metallicity, and cold gas fractions from $z \sim 0$–3 and we find that:

- All three scenarios are able to qualitatively reproduce the rising behavior of $f_\star$ and the comoving number density of low mass galaxies when we allow the parameterizations to be arbitrary functions of both halo mass and redshift, provided we do not include photo-ionization squelching. The three adjusted scenarios make different predictions for other observables such as cold gas fractions and sSFRs, which may help to discriminate between them.

- In the preferential reheating model, we altered the way in which the mass-loading of stellar-driven winds scaled with mass and redshift. This required a fairly dramatic change in the mass-loading factor's power law dependence on circular velocity as a function of time. Our model starts from $\alpha_{\rm RH}$=4.5 at $z > 2$ and transitions to $\alpha_{\rm RH}$=2 at $z < 1$, compared with a constant value of $\alpha_{\rm RH}$=1–2 for conventional momentum- or energy-driven winds. Although it is expected that wind scalings may deviate from the simple energy- or momentum-driven case, it is not clear whether physical processes can lead to such a large slope or effective redshift evolution.

- Direct suppression of star formation via explicit manipulation of the star formation timescale requires an aggressive suppression factor and a complicated redshift dependence. We expect that such strong variation in the star formation efficiency will be ruled out by direct observations. The direct suppression scenario is less tractable than might be expected because of the strongly self-regulated nature of star formation in the present paradigm. We therefore disfavor this class of solution relative to the other two.

- In the parking lot model, gas is held temporarily in a reservoir outside the galaxy and allowed to accrete on a specified timescale. This required fairly minor alteration to the standard scalings assumed in SAMs, especially relative to the very large uncertainties in our current understanding and parameterization of this process. Gas that has been heated either by gravitational interaction with other halos or by a global or local radiation field may have longer accretion times than expected in the standard picture of cosmological accretion. The SAMs predict, in agreement with results from recent numerical simulations, that this "pre-heated" gas may comprise a very significant component of the accretion.

- The predicted evolution of low mass galaxies in SAMs is quite sensitive to details of the bookkeeping for the hot and ejected gas reservoirs following halo mergers, as well as (at the lowest masses) to the modeling of accretion suppres-

sion and photo-evaporation by an ionizing background. This may explain why the proposed solution of H13 is not effective when implemented in some other SAM codes, including the fiducial Santa Cruz code.

Chapter 3

Calculating correlation functions

3.1 Introduction

As we have seen in Chapter 2, our theories concerning galaxy formation are not entirely well constrained by existing observations. Models of galaxy formation depend particularly heavily on the relationship between a galaxy's stellar mass and halo mass, $M_\star\left(M_{\rm halo}\right)$, to determine star formation and supernova feedback parameters. Almost all of the measurements of the $M_\star\left(M_{\rm halo}\right)$ relation are done with abundance matching. In its most basic incarnation, abundance matching takes a stellar mass function and a halo mass function and assigns the most massive galaxies to the most massive halos, working down to the least massive. Abundance matching measurements have allowed us to make large strides in understanding galaxy formation, but independent estimates of $M_\star\left(M_{\rm halo}\right)$ would be helpful both to verify abundance matching results

and to provide an independent constraint. We aim to provide this constraint by using correlation functions on galaxies in the Cosmic Assembly Near-infrared Deep Extragalactic Legacy Survey (CANDELS) fields to estimate dark matter halo masses in bins of stellar mass and redshift. To do this, we must first measure the correlation functions. In this chapter, we discuss and justify the choices we make when calculating the correlation functions for the CANDELS fields.

3.1.1 What is a correlation function?

The correlation functions that we will be considering, two-point galaxy autocorrelation functions, are a statistical measure that answer the question, "What is the probability of finding two galaxies separated by a distance d in excess of the probability of finding two points from a random distribution at that separation?" As the reader may have guessed from the number of adjectives, two-point autocorrelation functions are a particular kind of correlation function. Generally speaking, correlation functions are a measure of how strongly linked the values of two distributions are at a given separation in space and/or time. Correlation functions in general can be used on any number of points: "What is the probability of finding Objects 1, 2, ... N in this particular configuration?" Two-point correlation functions specifically examine separations between two points: "What is the probability of finding Object 1 at a certain distance from Object 2?" Galaxy correlation functions involving more than two objects do contain information that can be used as cosmological constraints,

but mass measurements using the technique we describe in Chapter 4 require only two-point correlation functions.

Autocorrelation functions compare a distribution to itself. One could imagine asking the question, "What is the probability of finding a galaxy of mass $M \pm \Delta M$ at a certain distance from a quasar in excess of random?" but this a cross-correlation rather than an autocorrelation. Galaxy autocorrelation functions ask, "What is the probability of finding two galaxies, both from Population A, a certain distance apart in excess of random?" For instance, the population could be galaxies of a certain stellar mass or color. For simplicity, we use the term "correlation function" to mean the two-point autocorrelation function because they are the only kind we consider in this work.

The separations between objects in correlation functions can be calculated in either two or three dimensions. The angular correlation function, $w(\theta)$, where the distance is the angular separation on the sky, is defined by the equation

$$dP = N\left[1 + w(\theta)\right] d\Omega \tag{3.1}$$

where θ is an angular separation, dP is the probability of a galaxy in the solid angle element $d\Omega$ and N is the average surface density of galaxies in the population under consideration over the entire sky. The real-space correlation function, $\xi(r)$, where

the distance is the physical separation, is defined as

$$dP = n\left[1 + \xi\left(r\right)\right] dV \tag{3.2}$$

where r is a physical distance, dP is the probability of finding a galaxy in the volume element dV, and n is the average volume density of galaxies in the population under consideration in the universe.

3.1.2 General properties of correlation functions

The simplest correlation function is that of randomly placed points. Because correlations are defined in excess of random, a random field has a correlation function that is zero at all separations. Any sample of objects that has a non-random distribution will have a correlation function that is not zero on at least some scales. When the correlation function is positive, the objects are more clustered than a random sample at that scale (correlated). When the correlation function is negative, the objects are less clustered than a random sample at that scale (anti-correlated). It is important to note that the *galaxy* correlation function must integrate to zero. The probability dP in Equations 3.1 and 3.2 must integrate to the number of galaxies, which means that the contribution of $w\left(\theta\right)$ or $\xi\left(r\right)$ must be zero.

Correlation functions of galaxy populations can be broken into two portions: the one-halo term and the two-halo term. The one-halo term is the contribution from

galaxies within the same halo. This means central-satellite pairs or pairs of satellites in the same halo. The one-halo term only contributes at small separations, the scale of clusters or less ($\lesssim 1$ comoving Mpc). The two-halo term is the contribution from galaxies in different halos and stretches out to much larger separations. Figure 3.1 shows clustering results from Kravtsov et al. (2004a), who use a halo occupation distribution to populate halos from an N-body simulation (see Section 1.5.2). Note the upturn at small separations- this is the one-halo term. They show the one- and two-halo terms individually as the dashed and dot-dashed lines respectively. At separations larger than about 0.3 comoving h^{-1}Mpc, the correlation function is approximately a power law.

Most galaxy autocorrelation functions take roughly this form. The exceptions would be galaxy populations that never share a halo, such as brightest cluster galaxies. In correlation functions that do have a one-halo term, the scale of the transition from the steeper one-halo term to the shallower two-halo term increases slightly towards lower redshift (Kravtsov et al., 2004a). This is due to cluster growth: as groups of galaxies get larger, the maximum separation between galaxies in the same halo increases. Kravtsov et al. (2004a) also find that the transition between the two terms is sharper at higher redshifts because at low redshifts, large, rare galaxy clusters add a small amount of signal at the transition between the one- and two-halo terms. Large clusters are not present at high redshift, so the transition remains sharp.

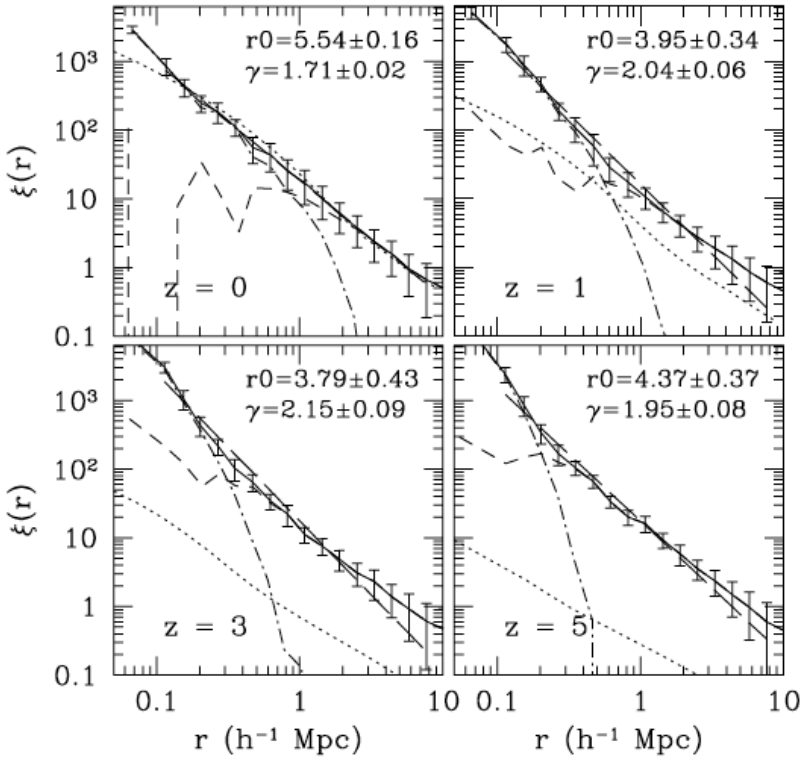

Figure 3.1: Figure 8 from Kravtsov et al. (2004a). Real-space correlation functions from their HOD model at four redshifts shown as solid lines with error bars. The one- and two-halo term decomposition is shown in the dot-dashed and dashed lines. The dark matter correlation functions are shown with dotted lines for comparison. Distances are in comoving h^{-1}Mpc.

3.1.3 Correlation function ingredients

The conceptual definition of an angular correlation function is Equation 3.1. However, the correlation function $w(\theta)$ cannot be calculated directly from Equation 3.1 because the probability dP is not known. Calculating $w(\theta)$ from a list of galaxy positions requires an estimation of the correlation function, an estimation of the errors on the correlation function, and, depending on the survey, a method for combining multiple fields.

Estimates of the correlation function are constructed from a set of galaxy positions and a set of randomly distributed points. The building blocks of correlation function estimators are histograms of the separations between all possible pairs of objects. For instance, the simplest estimator is the ratio between galaxy-galaxy pairs and random-random pairs. In this case, the numerator is the histogram of separations between all pairs of galaxies and the denominator is the histogram of separations between all pairs of randomly placed points. Errors on the correlation function are generally calculated using some re-sampling of the data. A re-sampling scheme allows multiple estimates of what independent observations of the underlying population would look like, provided the galaxies are an unbiased subset of the underlying population. Once the correlation function is estimated, it must be corrected for cosmic variance: the correlation function amplitude is connected to the average surface density of galaxies on the sky and most surveys do not observe the entire sky.

In this chapter, we examine and compare the methods used to generate random

distributions, choose bins in separation, estimate $w(\theta)$, estimate the offset due to cosmic variance, compute error bars, and combine multiple fields. These details can be important and are not often discussed in the literature. We show several examples of correlation functions to illustrate the differences between different options. Unless otherwise stated, the correlation functions shown in this chapter are calculated from a halo catalog from the Bolshoi-Planck simulation (Klypin et al., 2016), with the outline of the GOODS-N CANDELS exposures. The example correlation functions include halos between redshifts $1.75 < z < 2.25$ with mass greater than $M_{\rm halo} > 10^{10}$ $M_{\odot}$. For more information on the simulated catalogs, see Section 3.2.2.

3.2 The data

In this work, we use three main data sets for our analysis. The first is data from the Cosmic Assembly Near-infrared Deep Extragalactic Legacy Survey (CANDELS). The CANDELS survey consists of 906 orbits of Hubble observations directed at sections of the Great Observatories Origins Deep Survey (GOODS) in GOODS-N and GOODS-S, the Extended Groth Strip (EGS), the Cosmological Evolution Survey (COSMOS), and the Ultra-Deep Survey (UDS) fields (Grogin et al., 2011). These Hubble data are augmented by the large body of archival data available in those fields. The CANDELS data have been processed to catalogs which include photometry, photometric redshifts, and masses (Galametz et al., 2013; Guo et al., 2013; Dahlen et al., 2013;

Mobasher et al., 2015). The second data set we use is from the Behroozi et al. (2013a) sub-halo abundance matching (SHAM) procedure performed on the Bolshoi-Planck simulations (Klypin et al., 2016). These catalogs contain halo properties from the simulation and stellar masses determined by the SHAM procedure. The third data set consists of catalogs from the Santa Cruz semi-analytic model (Somerville et al., 2008b, 2012) run on the same light cones as the SHAM.

3.2.1 CANDELS survey

The CANDELS survey was designed to explore galaxy formation and evolution from redshifts $z \approx 8$ to 1.5 with a "wedding cake" observation strategy, where the survey includes several exposure depths with progressively longer exposures over progressively smaller areas. The widest exposures, CANDELS/Wide, cover the entire 800 arcmin^2 survey area in all five fields to a limiting magnitude of $\sim$27 in the H-band. Deeper exposures, CANDELS/Deep, cover $\sim$125 arcmin^2 in GOODS-N and GOODS-S to a limiting magnitude of 27.7 in the H-band. The preexisting Hubble Ultra-Deep Field (HUDF) observations serve as the third and deepest tier of the survey. (Grogin et al., 2011)

3.2.1.1 CANDELS Photometry

The photometric catalogs for the CANDELS survey include HST data collected by the survey, Early Release Science (ERS) and archival Hubble imaging including

the HUDF, and pre-existing observations of the areas covering wavelengths from the UV to the IR from various telescopes. Data reduction and mosaic assembly for the CANDELS images are described in Koekemoer et al. (2011). Photometry was extracted from the mosaics using a combination of Source Extractor (SExtractor) (Bertin & Arnouts, 1996) and the template fitting software TFIT (Laidler et al., 2007). First, SExtractor was run twice on the H-band imagery, once in a "cold" mode optimized to detect bright, large objects and once in a "hot" mode optimized to detect small, faint objects. The cold mode tends to miss small, faint objects, but the hot mode tends to over-deblend large objects. The hot and cold catalogs were merged by throwing out all hot mode detections that overlapped with cold mode detections, then combining the two catalogs. This allows for detection of faint objects without over-deblending larger objects. HST photometry from bands other than the H band was obtained by running SExtractor in dual mode with the H-band detections as priors for the other bands. (Galametz et al., 2013; Guo et al., 2013)

Photometry from archival data measured with other instruments was extracted with TFIT (Laidler et al., 2007). TFIT uses the spatial position and shape of objects detected in the high-resolution HST imagery to generate a template for the low-resolution images. The fluxes for each object in the low-resolution image are determined by smoothing the template to match the lower-resolution images and finding the best fit flux for each object. This allows for different point spread functions (PSFs) and resolutions in different bands while still using all the available information on po-

sition and surface brightness profiles from the high-resolution Hubble imagery. TFIT performs significantly better than SExtractor at reproducing simulated photometry in such situations (Lee et al., 2012).

3.2.1.2 CANDELS Redshifts

Some of the galaxies in the CANDELS fields have pre-existing spectroscopy, but the majority do not. Because of this, we will be relying on photometric redshifts for the majority of the objects we examine. As part of the public release of the CANDELS data, Dahlen et al. (2013) examined the reliability of photometric redshifts computed with various codes and methods. Eleven teams within CANDELS ran their SED fitting methods of choice to determine the photometric redshifts of a selection of galaxies with known spectroscopic redshifts within the CANDELS fields. Dahlen et al. (2013) find that no single code does *significantly* better than any other single code. Some codes were *slightly* better than the others. These codes included emission lines in the SED fitting templates and adjusted the templates based on a training set. The median of all of the different codes' results performed better than any single code, so we use the median redshifts as our photometric redshifts. Where they are available, we will be using high-quality spectroscopic redshifts instead of photometric redshifts.

3.2.1.3 CANDELS Stellar masses

The CANDELS catalogs also contain SED-fit galaxy properties including stellar masses. Mobasher et al. (2015) studied the dependence of inferred stellar masses on SED fitting code, SED templates, free parameters, and galaxy properties. They perform tests on mock catalogs with known stellar masses and observed CANDELS galaxies to quantify the error and bias from the SED fitting and conclude that the best estimate of the stellar mass is the median of the different methods. They caution that since the different methods are doing inherently different things, the median of the codes' results is not necessarily a statistically robust quantity: a different set of codes could produce different results. The set of codes used in the CANDELS catalogs has been tested and the median is more accurate than the individual codes, so we use the median for the stellar mass estimate. When using the same initial mass functions and Bruzual & Charlot (2003) templates, stellar masses for CANDELS-like data are relatively unbiased (< 0.05 dex) and have a scatter of $\lesssim 0.3$ dex for signal to noise ratios S/N> 10. (Mobasher et al., 2015)

3.2.2 SHAMs

For many of our methods tests, we use catalogs of simulated dark matter halos with stellar masses from SubHalo Abundance Matching (SHAM). We will call these catalogs the "SHAMs." The SHAMs are light cones created by Peter Behroozi from

the Bolshoi-Planck dark matter simulation (Klypin et al., 2016) with the Robust Overdensity Calculation using K-Space Topologically Adaptive Refinement (ROCKSTAR) halo finder (Behroozi et al., 2013b) and stellar masses for each halo generated with with the Behroozi et al. (2013a) subhalo abundance matching routine.

The Bolshoi-Planck simulation was run using an Adaptive-Refinement-Tree (ART) code (Kravtsov et al., 1997; Gottloeber & Klypin, 2008) with cosmology consistent with the Planck 2015 results: $h = 0.678$, $\Omega_M = 0.307$, tilt $n = 0.96$, $\sigma_8 = 0.823$, and $\Omega_{\rm baryon} = 0.048$. The simulation volume is 250 h^{-1}Mpc with 2048^3 particles with a mass resolution of $1.5 \times 10^8 h^{-1}\ M_\odot$ (Klypin et al., 2016). The code resolves halos down to a circular velocity of 50 km/s Rodriguez-Puebla et al. (2016). The halo catalogs that we use are extracted from the Bolshoi-Planck simulation with the ROCKSTAR halo finder (Behroozi et al., 2013b). ROCKSTAR uses spatial, velocity, and time information to robustly identify halos using a friends-of-friends algorithm. ROCKSTAR produces a halo catalog for each output redshift. These snapshots are then combined into a light cone, as in Hayward et al. (2013).

3.2.3 SAMs

The third data set we use is similar to the SHAMs but with galaxy properties generated by the Santa Cruz Semi-Analytic Model (SAM) (Somerville et al., 2008b, 2012). We call these catalogs the SAMs. The SAMs are run on the same dark matter halos as the SHAM described in Section 3.2.2. We discuss the Santa Cruz

semi-analytic model in depth in Section 2.2.

Semi-analytic models in general are collections of analytic recipes that describe the bulk behavior of galaxies in the context of theoretical or simulated dark matter evolution. Semi-analytic models are orders of magnitude faster than full hydrodynamic simulations but are closer to the underlying physics than abundance matching routines. They take the dark matter evolution as input, then numerically integrate their set of analytic recipes to produce galaxy properties for each halo. These properties include stellar mass, stellar age, metallicity gas mass, and photometry. Photometry is generated using spectral energy distributions for simple stellar populations combined with the star formation history of the simulated galaxy.

Semi-analytic models have known limitations (see Section 2.1) but for the most part are no better or worse at predicting observed stellar mass functions than hydrodynamic models. This is in large part because they use similar recipes to regulate star formation. The advantage of testing our methods with the SAMs in addition to with the SHAMs is twofold. First, the SHAMs have no photometric information. With the SAMs, we have the same halo information as in the SHAMs but we can select galaxies using the same criteria as we do on the data, including magnitude cuts. Second, we can assess the semi-analytic model performance by comparing the clustering properties of the model to reality.

One difficulty that the SAMs face which SHAMs or hydrodynamic simulations do not is the positioning of satellite galaxies. The SAM does not track subhalo positions,

so when two galaxy/halo systems merge, all the satellites must be assigned positions in the halo. These positions are characterized by a distance from the center and random phase. The random phase doesn't play a role in the evolution of the satellite galaxy; it only matters when assigning galaxy positions on the sky. From their initial positions, the satellites' "orbits" decay, following a variant of the Chandrasekhar formula (Boylan-Kolchin et al., 2008). As they fall in, they are stripped and eventually may merge with the central galaxy.

The initial placement of SAM satellites can strongly affect clustering. The original recipe in Somerville et al. (2008b) and Somerville et al. (2012) was to place all new satellites at the virial radius of the central halo with a random phase. This is clearly unphysical and creates a large spike in the histogram of separations between centrals and satellites. An alternative approach would be to blur the initial satellite radius. This is easily done by scattering satellites about the virial radius by a ΔR drawn from a normal distribution with some width σ_R. This doesn't account for the fact that many of the galaxies falling into the new central halo started out physically associated to one another. An even better system would be to use the existing information about galaxies' relative positions. We can place each infalling central at about the virial radius and preserve the satellites' positions relative to the central. This serves to smooth out the distribution of central-satellite separations and more accurately reflect how galaxies are likely to be clustered.

3.3 Estimators

Correlation function estimators are the methods by which galaxy positions are turned into estimates of $w(\theta)$ or $\xi(r)$. As discussed in Section 3.1.3, the conceptual definitions of the correlation functions, Equations 3.1 and 3.2, define the correlation functions but do not allow for their calculation. Instead, we use the separations between pairs of galaxies, between galaxies and random points, and between pairs of random points to estimate the correlation function.[1] Throughout this work, we use D to represent the positions of galaxies (data) and R to represent the positions of randomly placed points. The building blocks of correlation function estimators are DD, a histogram of separations between all possible galaxy-galaxy pairs; DR, a histogram of separations between all possible galaxy-random pairs; and RR, a histogram of separations between all possible random-random pairs.

Variance in correlation function estimators is unavoidable because galaxy catalogs are finite. The smallest variance that an estimator could have is Poisson variance in which the variance in a bin of counts is equal to the average number of counts in that bin. Note that the variance on the correlation function stems from but is not equal to the variance of counts in a bin: see Landy & Szalay (1993) Equations 43, 46, and 48. The smaller the sample, the larger the variance around the true value of the correlation function. Some combinations of DD, DR, and RR are biased relative to

[1] See Section 3.4 for a description of how the random points are placed.

the true correlation function,[2] so the estimator must be chosen with care and checked for bias. An ideal estimator would have no bias and Poisson variance. In this section, we review several of the most common estimators.

The simplest estimator is

$$1 + w(\theta) = \frac{DD}{RR}\frac{n_r^2}{n_d^2} = f^2\frac{DD}{RR} \tag{3.3}$$

Here, n_r is the number of points in the random catalog and n_d is the number of points in the data catalog. We will call this estimator the "standard" estimator. The factor $f \equiv n_r/n_d$ is the normalization factor in case the random catalog and the data catalog have different numbers of objects in them. Using this normalization is the same as assuming that the galaxy density observed represents the universal average number density. Landy & Szalay (1993, LS93) showed that the standard estimator is unbiased but has variance larger than the Poisson variance. As an alternative to the standard estimator, LS93 proposed the estimator

$$1 + w(\theta) = \frac{f^2 DD - 2fDR + RR}{RR} \tag{3.4}$$

The Landy-Szalay estimator is unbiased and has Poisson variance when $w(\theta)$ is small.

[2]The ratio of the expectation values of two random numbers is always less than or equal to the expectation value of the ratio: $E(x)/E(y) \leq E(x/y)$ (Jensen's inequality). RR can be evaluated to arbitrary precision with a sufficiently large random sample, but DD and DR cannot because the galaxies observed are all that are available. Thus, estimators like DD/DR are ratios of random numbers and are biased.

More recently, Vargas-Magaña et al. (2013) examined the variance of the Landy-Szalay estimator for $\xi(r)$ when the correlation function was not small. The Landy-Szalay estimator does not have minimal variance with non-negligible correlations but remains unbiased. Vargas-Magaña et al. (2013) propose a method for optimizing an estimator based on the correlation function itself using a linear combination of ratios such as $\frac{DD}{RR}$, $\frac{DD}{DR}$, and $\frac{DD \times RR}{DR^2}$. They do this by taking an ensemble of mock catalogs with the appropriate geometry and computing DD, DR, and RR on each of them. Then they use χ^2 minimization on the variance of a linear combination of all possible ratios of DD, DR, and RR up to second order. This produces an estimation of the correlation function that has about 25% less variance than the Landy-Szalay estimator for reasonable correlation magnitudes. However, it has non-negligible bias that is a function of galaxy separation and cosmology. To reduce the bias, they generate mock catalogs with different cosmologies, generate an optimized estimator for each, compute the bias for each, and subtract it from the estimators. They iterate, running the original optimization with the new correction for bias to get the minimal variance estimator and calculate the new value of residual bias. The Vargas-Magaña estimator is of use in cases where the correlation signal of interest is buried under noise, such as fitting baryon acoustic oscillation signatures (Vargas-Magaña et al., 2013). Galaxy correlation functions do not fall into this category, so **we will use the Landy-Szalay estimator** because the Vargas-Magaña estimator is so involved to calculate and only provides a 25% gain in variance.

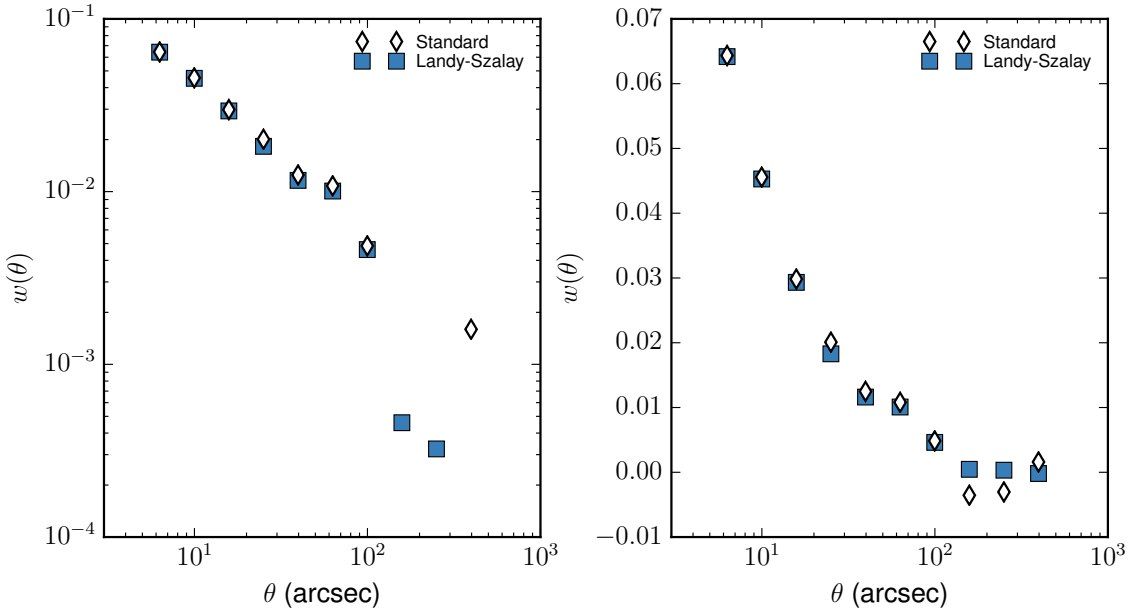

Figure 3.2: Comparison of correlation function estimators. The standard estimator is shown as open diamonds and the Landy-Szalay estimator as blue squares with Poisson error bars that are smaller than the point size. The two panels are identical except for the y-axis scaling and extent. The sample of galaxies is SHAM halos with mass $M_{\rm halo} \geq 10^{10}$ at redshifts $1.75 < z < 2.25$ in a region the shape of the CANDELS GOODS-N field.

With an estimator in hand, computing the correlation function is fairly simple (except in the case of the Vargas-Magaña estimator, which we are not considering). The first step is to construct DD, DR, and RR by computing all the separations between all the unique galaxy-galaxy, galaxy-random, and random-random pairs. These separations are then binned (see Section 3.6) to generate the DD, DR, and RR histograms. Then the correlation function in each bin is given by the counts in the DD, DR, and RR histograms inserted into the correlation function estimator formula. In Figure 3.2, we show the standard estimator and the Landy-Szalay estimator on a subsample of the SHAM. The Poisson variance for this sample is smaller than

the point size. The example correlation function shown dips below zero in the widest separation bin, so the correlation functions in the left panel, with a logarithmic y-axis, appear to drop out at large separations. The right panel shows the same correlation functions but with a linear y-axis. The variance of the Landy-Szalay estimator around the overall power law trend is clearly smaller in this view. However, the standard estimator remains unbiased: the median difference between the estimators, $\Delta w = w_{\rm std}(\theta) - w_{\rm LS}(\theta)$, is $\Delta w_{\rm med} = 4 \times 10^{-4}$ and the mean is $\langle \Delta w \rangle = -1 \times 10^{-4}$.

3.4 Randoms

An important component of all correlation function estimators is the random catalog, a collection of randomly placed points. Placing the random points properly is crucial because it serves as a baseline: correlation functions are defined as the clustering *in excess of random*. Improperly distributed randoms alter the shape of measured correlation functions. Random placement must consider field shape and observation depth so that randoms are placed in the same area as the observed galaxies and with the right number density as a function of position on the sky. In galaxy samples where the observation depth is the same across the area of the survey, the randoms can be distributed with a uniform density. Randoms can also be evenly distributed for catalogs of simulated galaxies because the "observation depth" is the same over the whole simulation (provided the catalog hasn't been altered to simulate

variable completeness). Note that the number of randoms is not constrained by the estimators- the estimators all normalize for differences in number density- but is constrained by practicalities. Using too few randoms introduces noise into the correlation function and using too many randoms results in impractical computation time.

Multi-depth surveys, such as CANDELS, require more attention to random placement than single-depth surveys or simulated galaxy catalogs because the observable number density changes as a function of position on the sky. One option for multi-depth surveys is to place randoms evenly across the observation area and cut the galaxy sample at a magnitude that is mostly complete for the shallowest area of the survey. This can introduce some artificial clustering because the deep areas will always have a higher completeness than the shallow areas (Lee et al., 2006). Even without artificial clustering concerns, one of the strengths of a multi-depth survey is the detection of fainter galaxies in the deep areas. Using the shallowest depth's completeness limit ignores many of the observed galaxies and disregards one of the main strengths of a multi-depth survey.

Properly accounting for multiple depths within a survey area is often done with simulations (e.g. Lee et al., 2006; Barone-Nugent et al., 2014). Simulated randoms for multi-depth surveys are generated by placing a small number of real or simulated galaxy images in the actual observations, accounting for noise and exposure time, and processing the images through the same pipeline that generated the galaxy cat-

alog. The fake galaxies that are recovered are added to the random catalog and the simulation is repeated with new fake galaxies. Building up a large enough sample of randoms requires many hours of simulation and image processing because only a few galaxies at a time can be placed in the images due to crowding concerns.

For this work, we calculate correlation functions of simulated galaxies, which do not require a variable completeness treatment, and of CANDELS galaxies brighter than 26th magnitude in the H-band, the 90% completeness limit for the CANDELS/Wide observations. This introduces a small risk of overestimating correlations in faint samples. We plan to implement a hybrid method of random generation in future work that uses simulations to calculate completeness functions that take into account galaxy magnitude, radius, and placement on the image. This allows for efficient variable completeness random generation without the cost of fully simulated random catalogs. Coil et al. (2004) use a similar method using completeness functions that depend only on position and redshift.

3.5 Error bars

Estimating error is important in any measurement. The theoretical lower limit on a correlation function's variance is determined by the Poisson variance: the expected number of counts in the bin (see Section 3.3). This limit is not attained with non-negligible correlations except with the Vargas-Magaña estimator. Galaxies have

non-negligible correlations and we are using the Landy-Szalay estimator for simplicity and computation time, so we must compute our errors a different way. Resampling methods, or internal error estimates, use the variance between repeated correlation function measurements on different subsamples of the data to approximate what the true variance would be in an ensemble of similar fields. In this section, we discuss the three most common methods used on correlation functions: single-galaxy bootstrapping, block bootstrapping, and jackknifing.

In general, bootstrapping refers to the process of repeatedly drawing N elements from the original list of N objects *with replacement* so that some elements may be drawn multiple times and some may not be drawn at all. In single-galaxy bootstrapping, the element is an individual galaxy. An iteration of a single-galaxy bootstrap randomly draws $N_{\rm gals}$ galaxies with replacement from the catalog of $N_{\rm gals}$ galaxies and calculates the correlation function of the randomly drawn sample. This correlation function is stored, and the process is repeated. After $N_{\rm boot,sg}$ iterations, we have $N_{\rm boot,sg}$ correlation functions. The mean value of the bootstraps estimates the value of the correlation function and the standard deviation between bootstraps estimates the error.

In block bootstrapping, the element is a spatial block of the field rather than a single galaxy. Ideally, the $N_{\rm blocks}$ blocks are roughly square and of the same size so that there is no preferred direction or area of the field. An iteration of block bootstrapping randomly draws $N_{\rm blocks}$ with replacement from the list of blocks. All of the galaxies in

each block are put into the iteration's galaxy catalog as many times as the block was drawn. The correlation function of the drawn galaxies is calculated and stored and the process is repeated. The correlation functions and errors are estimated by the mean and variance between the correlation functions from the different bootstraps, the same as in single-galaxy bootstrapping. This method takes into account the fact that galaxies are correlated: if a galaxy is in the sample, the sample should also include all the galaxies physically associated with it. Norberg et al. (2009) show that block bootstrapping of real-space correlation functions overestimates the true variance, calculated from the variance between measurements on an ensemble of N-body simulations. However, block bootstrapping overestimates the variance by the same factor at all scales, which can be corrected by drawing two to three times as many blocks as the field is divided into, artificially reducing the variance between iterations.

Jackknifing also uses spatial blocks of the field but instead of randomly drawing $N_{\rm blocks}$ blocks for each iteration, the jackknife omits each block in turn. This results in $N_{\rm blocks}$ jackknifes, each consisting of the correlation function of $N_{\rm blocks}$-1 blocks. Norberg et al. (2009) find that in the case of real-space correlation functions, the jackknife variance estimate is too large at small separations and approaches the true variance at large separations. They couldn't find a way to make the jackknife variance agree with the true variance across all separations as they did with block bootstrapping. Cabré et al. (2007) test the jackknife method on a very large field: 10% of the

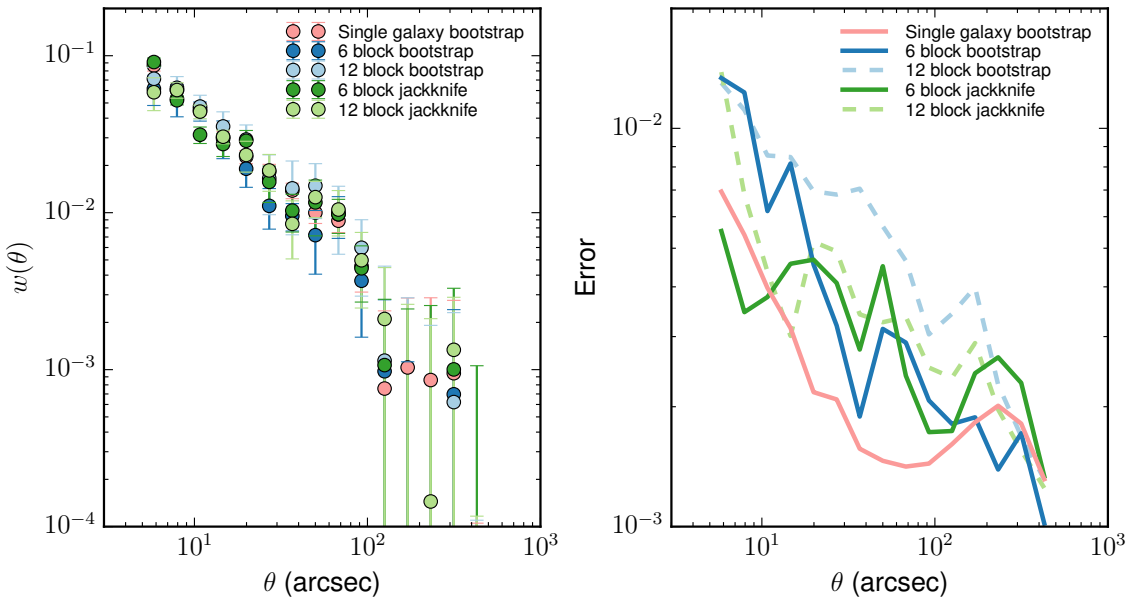

Figure 3.3: In the **left panel**, we show the Landy-Szalay correlation functions with errors calculated with single-galaxy bootstrapping, block bootstrapping, and jackknifing. The block bootstrap and jackknife errors are shown with the GOODS-N field divided into 6 tiles or 12 tiles. The **right panel** shows the sizes of the error bars in the correlation functions on the left.

sky. They find that the jackknife method reproduces the true correlation function variance between simulations as long as the blocks are roughly the same size and shape. The disagreement between Norberg et al. (2009) and Cabré et al. (2007) on the accuracy of jackknife errors is most likely because Cabré et al. (2007) investigate angular correlation functions and Norberg et al. (2009) examine real-space correlation functions. The projection of the catalogs to two dimensions may change the statistics sufficiently to affect the jackknife performance (Norberg et al., 2009).

We compare the error calculation methods in Figure 3.3. The sample in question is SHAM galaxies in a cutout the shape of GOODS-N with redshift $1.75 < z < 2.25$ and

halo mass $M_{\rm halo} \geq 10^{10}$. We test single galaxy bootstrapping, block bootstrapping with 6 or 12 blocks, and jackknifing with 6 or 12 blocks. The left panel shows the correlation functions and errors, while the right panel isolates the error bar size. In the right panel, the errors from the four block resampling methods all lie in the same general area. Single-galaxy bootstrapping deviates from the rest of the methods at intermediate separations. For most of our test correlation functions, we use single galaxy bootstrapping because it cuts down on computation time significantly. Using single galaxy bootstrapping does not significantly affect the fits, biases, or masses (see Section 4.3.2). For the final CANDELS correlation functions, **we use block bootstrapping** with blocks about 300" on a side. This works out to eight blocks each in COSMOS and UDS, six each in GOODS-N and GOODS-S, and five in EGS.

3.6 Theta binning

Converting lists of galaxy and random positions to DD, DR, and RR histograms requires a choice of binning in separation, which is seldom discussed in the literature. The total separation range affects the information contained in the correlation function and bin width affects the variance of the correlation function. Having too many bins decreases the number of counts in each bin and increases the noise in the correlation function measurement. Figure 3.4 shows the correlation function of our SHAM test sample computed over 5"$< \theta <$500" with 5, 10, and 30 bins. The right

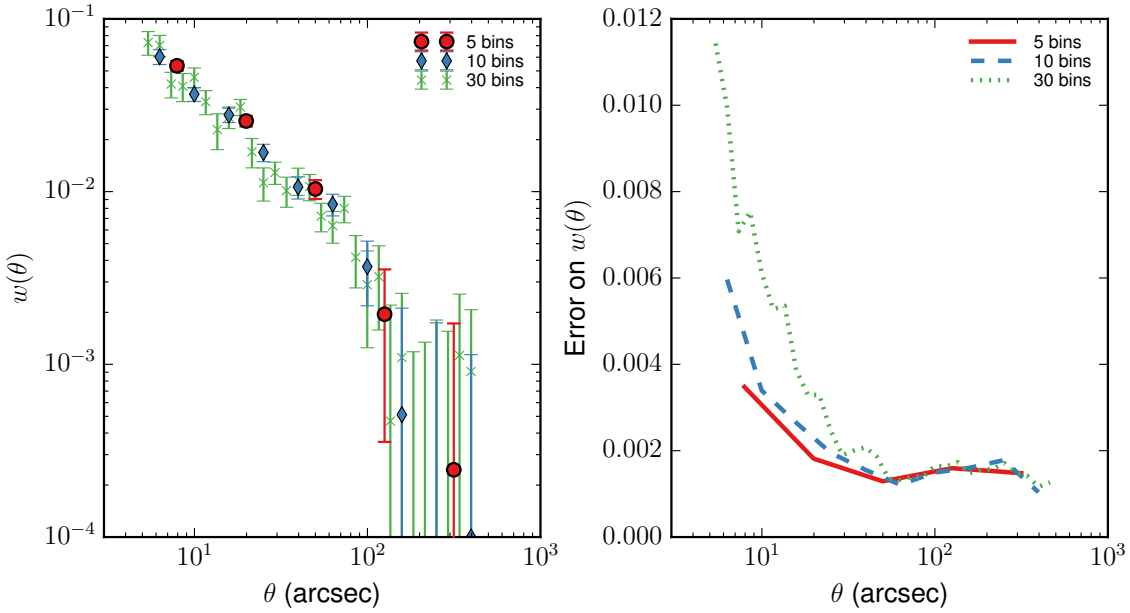

Figure 3.4: In the **left panel**, we show the correlation function for the GOODS-N SHAM with $1.75 < z < 2.25$ and $M_{\rm halo}$. The correlation functions are calculated with the Landy-Szalay estimator and single-galaxy bootstrap errors over the range 5"$< \theta <$500" with different numbers of bins. In the **right panel**, we show the error size as a function of scale for the same correlation functions.

panel shows the size of the errors on the correlation functions. The more bins, the larger the error bars. Having too many bins also means that the values of neighboring bins will be more correlated, which contradicts the assumptions of some fitting mechanisms (e.g. χ^2 minimization) (Mo et al., 1992). On the other hand, having too few bins smooths out useful information about the shape of the correlation function.

Bins are generally spaced evenly in log separation for galaxy correlation function applications (logarithmic bins). Less commonly, bins can be spaced evenly in linear separation (linear bins). Much of the signal relevant to studying galaxies is at small separations, which linear bin spacing doesn't resolve. Figure 3.5 shows the same

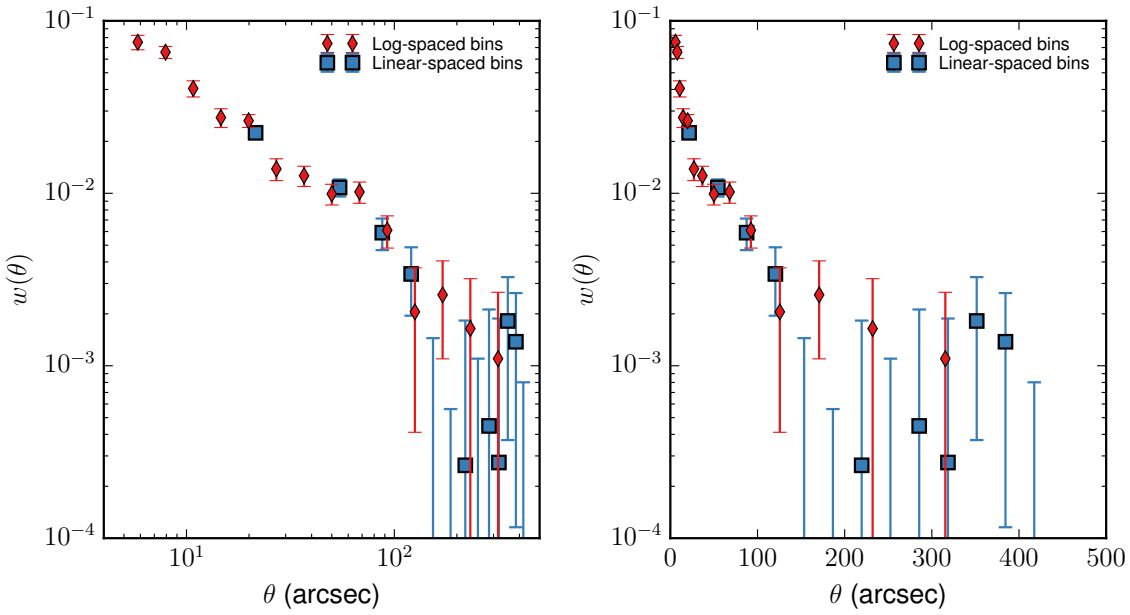

Figure 3.5: Correlation functions of the same sample calculated with logarithmic and linear binning. The same correlation functions are shown on the left and the right with logarithmic and linear x-axis scales, respectively.

correlation function calculated with logarithmic and linear binning over the same range in separation. Note that the main reason the error bars for the linear case at large separations look so large is the log scale. The errors are actually smaller than those at small separations (see the right panel of Figure 3.4). **We use logarithmic bins for the CANDELS correlation functions.**

3.7 Integral constraint

The definition of the correlation function, Equation 3.1, involves the true number density of galaxies over the entire sky, which we can't determine exactly from a finite

field. The best estimate available is the number density of galaxies in the observed field. In general, a small piece of the sky will be under-dense with respect to the universal average because under-dense regions occupy more space than over-dense regions. Underestimating the average number density leads to a overestimation of the normalization of the correlation function.[3] The correction for this is called the integral constraint. The integral constraint originates from the requirement that the integral of the correlation function over all scales be zero:

$$\begin{aligned} \int dP &= N \int \left[1 + w(\theta)\right] d\Omega \\ N_{\rm gals} &= 4\pi N + N \int w(\theta) d\Omega \\ N_{\rm gals} - 4\pi N &= 0 = N \int w(\theta) d\Omega \\ \Rightarrow \int w(\theta) d\Omega &= 0 \end{aligned} \tag{3.5}$$

The $\int dP = N_{\rm gals}$ because probability of finding a galaxy an angle θ from another integrated over the entire sky is equal to the number of galaxies on the sky.

How does this apply in practice? The most common way to apply the integral constraint correction is to integrate a fit to the correlation function over the survey

[3]The number of random-random pairs is the baseline to which galaxy-galaxy pairs are compared to compute the correlation function. The ideal normalization for the RR histogram is that which corresponds to the universal average number density. Often, we use many more randoms than galaxies to reduce the noise in the correlation function, so the factor f in the estimators renormalizes the counts that include randoms to what they would be if the randoms were placed with the same number density as the galaxies (see Equations 3.3 and 3.4). However, the galaxy number density is usually below the universal average number density, so the random counts are usually set too low. Randoms always appear in higher order in the denominator of estimators, so an underestimate in RR increases the estimate of the correlation function.

area and subtract off the result. The numerical Roche & Eales (1999) approach is most commonly used:

$$IC = \frac{\sum RRw_{\rm fit}(\theta)}{\sum RR} \tag{3.6}$$

Here, IC is the integral constraint, RR is the number of random-random counts as a function of θ and $w_{\rm fit}(\theta)$ is a functional fit to the correlation function. The quantity $RRw_{\rm fit}(\theta)$ is approximately the expected DD counts for a correlation function $w_{\rm fit}(\theta)$ (see Landy & Szalay (1993), Equation 25). That means that Equation 3.6 is approximately the integral of $w\,(\theta)$. If the integral is non-zero, using $w(\theta) = w_{\rm fit}(\theta) - IC$ will guarantee that $\int w(\theta)d\theta = 0$.

With the integral constraint calculated, the correlation function becomes

$$w_{\rm corrected}(\theta) = w_{\rm observed}(\theta) - IC \tag{3.7}$$

However, a change in normalization can change the fitting parameters. Adelberger et al. (2005) proposed an iterative method for fitting with an integral constraint correction. To do this, they fit the raw data, subtract off the integral constraint as given by Equation 3.6, and fit again. The new fit determines a new integral constraint correction and they repeat the process until it converges. Adelberger et al. (2005) found this routine was unstable in the case of a fit to a power law with the power as a free parameter. Fixing the power stabilized the routine. The Adelberger et al. (2005) extension of Equation 3.6 is ubiquitous, so we refer to this method as the Adelberger

integral constraint correction.

The Adelberger integral constraint correction is the expectation value of the integral constraint correction, which is always positive for a power law fit to a correlation function. The correct integral constraint correction may be negative if the survey area falls into an over-dense region instead of an under-dense one, which couldn't be reproduced with a power law fit and the Adelberger formulation. The actual integral constraint corrections for an ensemble of fields with correlation function $w(\theta)$ and the same field shape will be distributed about the expectation value from Equation 3.6 with some scatter. The integral constraint distribution has a large scatter, meaning that the value given by the Adelberger integral constraint correction is not necessarily the appropriate one for the particular field measured.

An alternative to the Adelberger integral constraint correction is to fit the integral constraint as a constant offset. Most of the time, the two-halo term of the angular correlation function is fit with a power law:

$$w(\theta) = A\theta^{-\beta} \tag{3.8}$$

but it can instead be fit with a power law minus a constant:

$$w(\theta) = A\theta^{-\beta} - C \tag{3.9}$$

The resulting correlation function does not necessarily integrate to zero over the field,

but the degeneracy between the integral constraint and the power law fit parameters is broken. **We use the offset integral constraint** rather than the Adelberger integral constraint because we find that it produces better, more reliable fits (see Section 4.3.2).

3.8 Combining fields

In surveys like CANDELS, observations are taken over several widely spaced fields to minimize the effects that cosmic variance has on measurements. Measuring a correlation function over multiple fields requires a scheme for combining the information from the different fields. The options are:

1. Calculate a single correlation function for all the fields by treating the fields as different parts of a single field. The single correlation function is then fit and the integral constraint correction is applied.

2. Calculate a correlation function for each field, apply the integral constraint correction to each field individually, and average the fields together. The average correlation function is then fit but does not need to be corrected for the integral constraint.

3. Calculate a correlation function for each field and do not apply the integral constraint correction. Fit and apply the integral constraint correction to the ensemble.

The first option combines the fields while still in count histogram space (DD, DR, RR). This is particularly useful for correlation functions of small numbers of galaxies where individual fields do not contain enough information for a clean correlation function. The DD, DR, and RR histograms are constructed by summing the individual fields' histograms: $DD = \sum_{i=1}^{N_{\text{fields}}} DD_i$, $DR = \sum_{i=1}^{N_{\text{fields}}} DR_i$, and $RR = \sum_{i=1}^{N_{\text{fields}}} RR_i$. The correlation function is calculated from the aggregate histograms with the estimator as usual. Doing this properly requires particularly careful placement of randoms. In the single field case, as long as the distribution of randoms matches the variations in observation depth in the field, the estimators take care of the normalization. In the multi-field case, the relative number of randoms from field-to-field is also important. If one field has twice as many randoms placed in it as the others (at a particular observation depth), its RR and DR histograms will be too high relative to the other fields. The excess is scale dependent because it depends on the shape of the field with too many randoms. The normalization factors in the estimators only account for scale-independent excess, so excess in a single field changes the shape of the correlation function. However, if this is done carefully, it provides a single correlation function for multiple fields.

The second option is to calculate, fit, and apply the integral constraint correction to each individual field before averaging the correlation functions together. This method requires each single-field correlation function to be clean enough to have a high-quality fit for the integral constraint correction. It does not leverage the multiple

estimates of the average surface density of galaxies in the universe (one for each field), so the integral constraint correction may not be as accurate as other methods. This is the most conceptually simple of the methods and is straightforward to implement.

The last option is to fit and apply the integral constraint correction to the ensemble. This takes advantage of the multiple fields from which to estimate the integral constraint and isn't sensitive to field-to-field variations in the random distributions. The simplest way to do this is to average the correlation functions from the different fields, then fit and apply the integral constraint correction to the average. If there are more than two or three fields, this method can be extended to yield an error estimate on the fit in a way similar to the bootstrap error estimates on the correlation function (see Section 4.3.3). **We choose to fit and correct the ensemble of correlation functions** because we find it to be more robust than other methods and tolerant of small sample sizes.

3.9 Summary

In this chapter, we have presented the main options available for all aspects of calculating angular correlation functions. Our recommendations for correlation function calculation are based on our intent: to estimate dark matter halo masses in the CANDELS fields. Because we are examining the two-halo term in relatively small fields, we calculate our correlation functions over 10"$< \theta <$350". This minimum sepa-

ration is also used in Ouchi et al. (2005) and Lee et al. (2006), both of which allow for scale dependent bias but find constant bias at separations larger than 10". Kravtsov et al. (2004b) find that their HOD model predicts departure from a power law at scales smaller than 0.3 comoving h^{-1}Mpc, which is around 15" at redshift $z = 2$, decreasing to 10" at redshift $z = 6$. We test the effects of our choice of minimum separation in Section 4.3.2 and find that 10" produces the same results as 70", which is safely beyond all influence of the one-halo term. Our results are not sensitive to the maximum separation, so we choose 350", where the correlation functions start to get noisy.

We calculate the correlation function in seven logarithmically spaced bins with the Landy-Szalay estimator. We find that all three error estimation methods–single-galaxy bootstrapping, block bootstrapping, and jackknife–produce similar results. Single-galaxy bootstrapping is the fastest to calculate but least accurate, so we use it only for tests. The final CANDELS correlation functions we present have block bootstrap errors. See Section 4.3.2 for further motivation of these specific choices.

In this work, we have calculated the correlation functions for galaxies above the 90% completeness limit for the CANDELS/Wide exposure depth. For these correlation functions, we distribute the random sample evenly across the survey area. In future work, we will compute correlation functions with the entire galaxy sample, placing randoms with a variable completeness treatment. We choose to combine fields and integral constraint correct as part of the fitting routine, option (3) in Section 3.8:

	H-band mag > 26
Estimator	Landy-Szalay
Number of bins	7
Separation range	[10", 350"]
Error estimation	Galaxy bootstrap
Random placement	Uniform number density

Table 3.1: Summary of choices for the correlation functions we calculate.

we fit a power law plus an offset to the average of the correlation functions uncorrected for the integral constraint. This is mainly because we are pushing the limits of the correlation function quality that we can fit in order to get maximal resolution in mass and redshift for the $M_\star\,(M_{\rm halo})$ relation. The bootstrap estimate of the error on the fit is also useful. Fitting the ensemble of fields allows the use of noisier correlation functions and does not depend on variations in random catalog number density across fields. We find that fitting the integral constraint as a constant offset is somewhat more stable and produces better results than using the Adelberger et al. (2005) method. A summary of our choices is presented in Table 3.1 and we show our correlation functions for the CANDELS fields in Figure 4.12.

This exact procedure may not be optimal for all uses of correlation functions. For instance, the baryon acoustic oscillation signature is very faint and requires high angular resolution, so the Vargas-Magaña estimator may be worth the extra effort. The best course of action for uses in surveys unlike CANDELS or for applications different from mass measurement is to perform tests to determine result dependence on correlation function calculation choices, as in Section 4.3.2.

Chapter 4

Mass measurement from correlation functions

In Chapter 3, we described the process we use to calculate correlation functions for bins of mass and redshift in the CANDELS fields. In this chapter, we will discuss the steps needed to convert those correlation functions into measurements of dark matter halo masses. To do this, we will fit a power law to the five fields' correlation functions, deproject the fit, convert to a bias, and use the Tinker et al. (2010) $b\left(M_{\rm halo}\right)$ relation to turn the bias into a halo mass. We will also discuss the effects of the choices we made in Chapter 3.

4.1 Introduction

Intuitively, it makes sense that correlation functions hold information about dark matter halo masses: large groups of galaxies in close proximity are generally only found in giant clusters with high halo masses, while solitary galaxies, far from their neighbors, tend to live in much lower mass halos. Quantifying this relationship is often done via the halos' bias, a metric of how clustered halos are relative to some baseline.

One way to measure the typical halo mass for a population of galaxies is to measure the correlation function of the population, compute the population's bias, and compare to the predicted halo bias as a function of halo mass from N-body simulations. An alternative approach is to relate the predicted halo correlation function to the galaxy correlation function with a halo occupation distribution (HOD). HODs describe the number of galaxies expected to be observed in a halo as a function of its mass. This has more free parameters, making it harder to use on noisy data, but makes different assumptions. We focus on the first technique, measuring masses via the linear bias and the $b\left(M_{\rm halo}\right)$ relation, because this technique is the most model-independent way to calculate halo masses from clustering and is widely used with few analyses of its accuracy.

Galaxy correlation functions have two main components: the one- and two-halo terms (see Section 3.1.2). The one-halo term is the contribution of pairs of galaxies in the same halo whereas the two-halo term is the contribution from pairs of galaxies

in different halos. The two-halo term of the real-space correlation function seems to be well described by a power law (e.g. Kravtsov et al., 2004a). There is a simple relationship between the coefficients of a power law fit to a real-space correlation function and the linear bias of the sample. This relationship is useful even with angular correlation functions because a power law real-space correlation function implies a power law angular correlation function. The Limber equation relates the coefficients of two power laws using the redshift distribution (Limber, 1953; Peebles, 1980). This means that a power law fit to an angular correlation function can be converted into a linear bias fairly easily with the Limber equation and a redshift distribution. Then, the $b\left(M_{\rm halo}\right)$ relation measured from simulations converts the linear bias to a halo mass.

Converting from an angular correlation function to a bias to a halo mass assumes a number of things:

1. The calculation and integral constraint correction of the correlation function have been performed properly.

2. Fitting a line to a ratio of histograms returns the right fit parameters.

3. The fitting mechanism used on the correlation function takes into account or is unaffected by the correlations between bins.

4. The two-halo term is well-described by a power law.

5. The bias measured is the linear bias (i.e. only measured where the two-halo term dominates).

6. The galaxy bias and the halo bias are the same.

We talk extensively about the different aspects of measuring correlation functions in Chapter 3. The main point of concern in calculating the correlation function is the choice of angular separations used. The minimum separation is particularly important. If this separation is too small, nonlinear bias contaminates the bias measurement, which is likely to skew the mass estimates high. The maximum separation may also affect the mass measurement, though the choice thereof is limited by field geometry. In Section 4.3.2, we show the impact of choices in minimum separation, number of bins in separation, error estimator, and integral constraint correction.

Measuring the linear bias is crucial because the theoretical $b\left(M_{\rm halo}\right)$ relation is computed on scales where structure formation can still be approximated with linear collapse theory. The canonical choice of scale is 8 Mpc. Ideally, one would measure the bias on the data in the same way used to generate the $b\left(M_{\rm halo}\right)$ relation from simulations, but this would require impractically precise distance measurements. Instead, we rely on the power law shape of the correlation function and the scale-independence of linear bias to measure it with correlation functions at somewhat smaller scales.

Lastly, converting from a measured *galaxy* bias to a halo mass using the *dark matter* $b\left(M_{\rm halo}\right)$ relation assumes that the galaxy bias on large scales matches the halo bias exactly. This is not necessarily the case. For example, measurements of galaxy colors on scales up to several megaparsecs suggest that galaxy stellar mass may be linked to halo age as well as mass (e.g. Hearin & Watson, 2013). If the galaxy

sample is biased with respect to the halos, the halo masses we infer from galaxy bias will be too large.

In this chapter, our goal is to justify further our choices for correlation function calculations, to demonstrate the potential pitfalls in the mass measurement processes, and to lay out a path from measured correlation functions to dark matter halo masses. We examine the fitting mechanism, the deprojection of the angular correlation function into the real-space correlation function, the conversion to linear bias, and the inference of halo mass from bias. Once we have a justifiable method of converting correlation functions to halo masses, we measure halo masses for the CANDELS galaxies in bins of stellar mass and redshift to show the $M_\star$ ($M_{\rm halo}$) relation at several redshifts.

To test our methods, we generate and analyze correlation functions from the SHAM catalogs (see Section 3.2.2). With the SHAMs, we know the right answer and galaxy bias doesn't play a role because the positions are those of the halos rather than galaxies. If the method doesn't work on the SHAMs, it has no chance of working on the actual data, which include all the messiness that baryonic physics and observation entail.

4.2 Theory

In this section, we present the mathematics behind the techniques we discuss in this chapter. In particular, we deal with the bias of galaxies and halos. Conceptually

speaking, bias is a number that quantifies the preference for a population, for example elliptical galaxies or dark matter halos of a particular mass, to be found in dense environments over being found in low-density environments. For instance, brightest cluster galaxies (BCGs) should be very biased because they reside at the centers of giant clusters, while small blue spiral galaxies that primarily reside in the field should have low bias. Bias can be defined and calculated in different ways, so we show the definition of bias that we use and relationships between bias and other quantities, particularly the coefficients of a power law fit to the angular correlation function.

4.2.1 Definition of bias

Correlated primordial density fluctuations in the universe are the origin of correlations between galaxies or halos. At early times, the universe was almost perfectly homogeneous: the density fluctuations in the cosmic microwave background (CMB) are at the level of one part in 10^5. These correlated density fluctuations grew as the universe expanded and cooled, and now densities at the centers of luminous galaxies are 10^5 times the critical density (Binney & Tremaine, 2008). This transition between mostly homogeneous at early times and the current large variation in density is called structure formation. Structure formation is generally described in terms of the density, $\rho(\mathbf{x})$, or the dimensionless over-density, $\delta(\mathbf{x}) \equiv [\rho(\mathbf{x})/\rho_0] - 1$. Here, $\mathbf{x}$ is a comoving coordinate and ρ_0 is the average density of the universe measured in a volume V large enough that the universe is homogeneous on the scale of V^{-3}.

(Binney & Tremaine, 2008)

Structure formation can be divided into two regimes: the linear regime in which $\delta(\mathbf{x}) \ll 1$, and the non-linear regime in which $\delta(\mathbf{x}) \gtrsim 1$. The linear regime allows for simplifications that make the equations governing structure formation analytically solvable. In particular, it simplifies the behavior of $\delta_{\mathbf{k}}$, the Fourier transform of $\delta(\mathbf{x})$. In the linear regime, $\delta_{\mathbf{k}}$ grows proportional to a power law with time, $\delta_{\mathbf{k}} \propto t^{2/3}$ for a non-relativistic fluid and $\delta_{\mathbf{k}} \propto t$ for a relativistic fluid. Knowing this, we can predict the linear $\delta_{\mathbf{k}}$, and thus $\delta(\mathbf{x})$, at any time. Note that we will be using the linear $\delta_{\mathbf{k}}$ prediction even outside of the linear regime (i.e. $\delta(\mathbf{x}) \gtrsim 1$). The linear $\delta_{\mathbf{k}}$ serves as a baseline, even when extrapolated beyond its physical applicability. Linear theory also predicts that regions over-dense by a factor of 1.686 or more will eventually collapse and that halos will virialize (settle into a stable configuration) at an over-density of about 200 (Binney & Tremaine, 2008). These numbers are remarkably applicable despite the simplifications needed to derive them.

The universe isn't accurately described by the linear prediction for $\delta_{\mathbf{k}}$ at all scales and at all times. The densities of collapsed structures today (i.e. halos and galaxies) are many times the average density of the universe, meaning that $\delta(\mathbf{x}) \gg 1$ and that density fluctuations on the scales of collapsed structures no longer fall into the linear regime. Structure on large scales stays in the linear regime for a longer time than small scales, which must be the case because the universe is still homogeneous on large enough scales.

Often, it is more useful to think in terms of the power spectrum, $P(k)$, instead of $\delta_{\mathbf{k}}$. The power spectrum is defined by Peebles (1980) as $P(k) = V|\delta_{\mathbf{k}}|^2$.[1] Note that you can calculate a power spectrum for any density field or set of objects, not just the linear dark matter fluctuations. This includes discrete samples like galaxies and dark matter particles in N-body simulations. To calculate the power spectrum of a discrete sample, you can either represent each particle as a delta function in $\delta(\mathbf{x})$ and take the Fourier transform or you can map the densities onto a grid of some sort and take a fast Fourier transform (Jing, 2005). If you choose the latter, the mapping smooths out power on scales smaller than the grid and introduces sampling effects. Jing (2005) describes how to analytically correct the power spectrum for these effects.

One of the useful quantities that can be calculated with the power spectrum is the variance of $\delta(\mathbf{x})$ on a particular scale. Imagine measuring the average density within randomly placed spheres of a fixed radius R. The variance of those average densities, $\sigma(R)$, is the variance of $\delta(\mathbf{x})$ on the scale R. This $\sigma(R)$ is expressed as an integral of a power spectrum times the Fourier transform of the top hat window function of radius R, $\hat{W}$ (Tinker et al., 2010).

$$\sigma(R) = \frac{1}{2\pi^2}\int P(k)\,\hat{W}^2(k,R)\,k^2 dk \tag{4.1}$$

This variance can also be written as $\sigma(M)$, where $M \equiv 4\pi R^3\rho_0/3$. We will use this

[1] Binney & Tremaine (2008) use a slightly different convention for the Fourier transform, so they have a factor of $1/V$ rather than V. This doesn't change the value of $P(k)$, it's just a different convention for calculating $\delta_{\mathbf{k}}$.

quantity later in the expression of bias as a function of halo mass from Tinker et al. (2010). Also note that the variance $\sigma(R)$ is generally used to quantify the linear density fluctuations but can also be used with any population by substituting the population's $P_{\rm pop}(k)$ for the linear density's $P_{\rm lin}(k)$. In this case, we'll be interested in the dark matter halo variance.

The power spectrum of a population can be used to define the bias of that population. Recall that the linear power spectrum, $P_{\rm lin}(k)$, is the primordial power spectrum extrapolated with $\delta_{\mathbf{k}} \propto t^{2/3}$. The bias can be written as

$$b^2(k) = \frac{P_{\rm pop}(k)}{P_{\rm lin}(k)} \tag{4.2}$$

Here, $P_{\rm pop}(k)$ is the power spectrum of the population of interest, such as dark matter halos of a certain mass (Tinker et al., 2010). Physically speaking, this bias quantifies how much more clustered the population is than one would expect from the extrapolation of linear structure growth. Bias is scale-dependent in general. However, if the scale in question is still in the linear regime, bias is constant with k (Tinker et al., 2010).

If you compute the bias for populations of dark matter halos in narrow bins of halo mass from N-body simulations, you find a close relationship between the bias and the halo mass (Tinker et al., 2005, 2010; Peacock & Dodds, 1996). Tinker et al. (2010) compute this bias to halos mass relation, $b(M_{\rm halo})$, for halos detected with

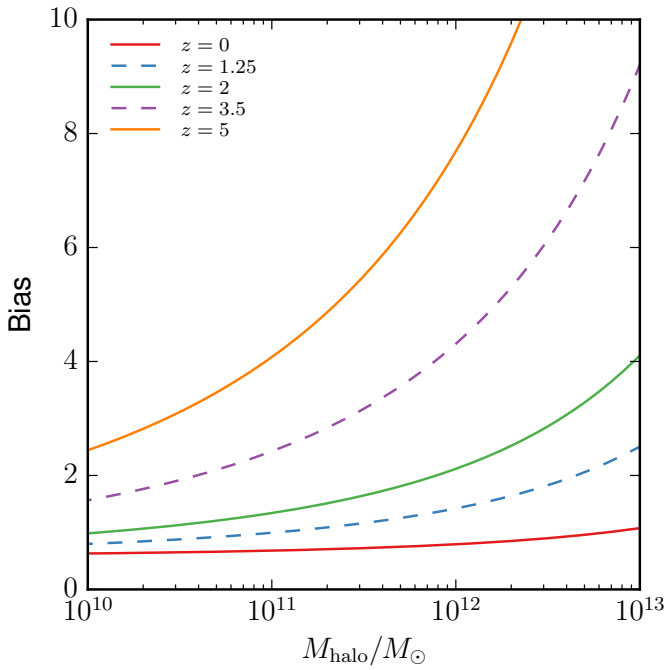

Figure 4.1: The bias as a function of halo mass from Tinker et al. (2010) for redshifts z =0, 1.25, 2, 3.5, and 5.

the spherical over-density technique, which grows spheres around over-densities until the average density inside the sphere is some multiple, Δ, of the average density of the universe. They then compute the power spectrum for halos in bins of halo mass by mapping their dark matter halos of a particular mass to a grid using a cloud-in-cell technique, taking the fast Fourier transform, and correcting the resulting power spectrum with the method described in Jing (2005). Then they describe the bias to halo mass relation as a function of redshift and halo mass with a fitting function. Instead of using the halo mass directly, Tinker et al. (2010) define their fitting function in terms of $\nu = \delta_c/\sigma(M)$, where δ_c is 1.686, the critical over-density required for collapse.

$$b(\nu) = 1 - A\frac{\nu^a}{\nu^a + \delta_c^a} + B\nu^b + C\nu^c \tag{4.3}$$

With this relation, if we measure the bias of a population of halos, we can look up the corresponding halo mass. The best fit parameters from Tinker et al. (2010) for the standard halo over-density, $\Delta = 200$, are $A = 1.00006$, $a = 0.132$, $B = 0.183$, $b = 1.5$, $C = 0.265$, and $c = 2.4$. We show this function for several redshifts in Figure 4.1.

4.2.2 Calculating bias from correlation functions

In the previous section, we describe the $b(M_{\rm halo})$ relation; the question now is how to measure the bias of a population of interest. This is where correlation functions

come in. There will always be some spatial correlation in density if $\delta(\mathbf{x})$ is continuous: neighboring values of $\delta(\mathbf{x})$ must be correlated and the smaller the separation between the two points, the more strongly correlated they are. In Section 3.1.1, we defined the correlation function in terms of a probability of finding two galaxies separated by some distance (Equation 3.2). Another way to define the real-space correlation function is in terms of the over-density:

$$\xi(r) \equiv \langle \delta(\mathbf{x}') \, \delta(\mathbf{x}' + \mathbf{r}) \rangle \tag{4.4}$$

Here, $\mathbf{x}'$ is a position, $\mathbf{r}$ is the vector separation between the two points under consideration and $r = |\mathbf{r}|$ (Binney & Tremaine, 2008). One can also write the correlation function in terms of the power spectrum (Peebles, 1980; Peacock & Dodds, 1996; Binney & Tremaine, 2008).

$$\xi(r) = \frac{V}{(2\pi)^3} \int d^3k \left\langle |\delta_{\mathbf{k}}|^2 \right\rangle e^{-i\mathbf{k}\cdot\mathbf{r}} = \frac{1}{2\pi^2} \int dk k^2 P(k) \frac{\sin(kr)}{kr} \tag{4.5}$$

If the bias is not a function of k ($b^2(k) = b^2$), then $P_{\rm pop}(k) = b^2 P_{\rm lin}(k)$ (see Equation 4.2). In this case, the squared linear bias b^2 is equal to the ratio of the correlation function of the population of interest to the correlation function of the linear density distribution. This is can be seen from the definition of the correlation

function in terms of the power spectrum (Equation 4.5).

$$\begin{aligned}\xi_{\rm pop}(r) &= \frac{1}{2\pi^2}\int dk k^2 P_{\rm pop}\left(k\right)\frac{\sin(kr)}{kr} \\ &= b^2\frac{1}{2\pi^2}\int dk k^2 P_{\rm lin}\left(k\right)\frac{\sin(kr)}{kr} = b^2\xi_{\rm lin}(r) \\ \Rightarrow \frac{\xi_{\rm pop}(r)}{\xi_{\rm lin}(r)} &= b^2 \end{aligned} \tag{4.6}$$

Similarly, because the $\sigma\left(M\right)$ equation is an integral over the power spectrum, bias can be calculated as a ratio $b^2 = \sigma_{\rm pop}/\sigma_{\rm lin}$.

In general, the bias is a function of scale, so we need to find a regime over which bias is constant. This regime is over scales that can still be described by linear collapse. When using the galaxy or halo angular correlation function to find bias, this means using only the two-halo term, where the correlation signal is from pairs of halos that are not in the same collapsed structure (see Section 3.1.2). The one-halo term, with signal from galaxies or halos that are gravitationally bound, is in the nonlinear regime because collapsed structures are inherently nonlinear.

With a correlation function measured in the correct regime in hand, how do we calculate our bias? We could use Equation 4.6, but there's a simpler way if the correlation function $\xi\left(r\right)$ is a power law,

$$\xi\left(r\right) = \left(\frac{r}{r_0}\right)^{\gamma} \tag{4.7}$$

where r_0 is the correlation length. With a power law correlation function, the bias can be written simply in terms of the coefficients r_0 and γ (Peebles, 1980; Lee et al., 2006).

$$b^2 = \sigma_{8,\mathrm{gal}}/\sigma_{8,\mathrm{lin}}(z)$$
$$\sigma^2_{8,\mathrm{gal}} = \frac{72\,(r_0/8h^{-1}Mpc)^{\gamma}}{(3-\gamma)\,(4-\gamma)\,(6-\gamma)\,2^{\gamma}} \tag{4.8}$$

Here, $\sigma_{8,\mathrm{lin}}(z)$ is the variance in density for the linear density distribution within an 8 h^{-1}Mpc window, calculated with Equation 4.1 and the linear power spectrum. Equation 4.8 is the equation that we will be using for our bias calculations. Note that $\sigma_{8,\mathrm{gal}}$ is the variance in numbers of galaxies in the same 8 h^{-1}Mpc window, not the dark matter mass variance. Our assumption that $\sigma_{8,\mathrm{gal}}$ can be used in the place of $\sigma_{8,\mathrm{halo}}$ is equivalent to assuming that galaxies are unbiased tracers of halos.

4.2.3 Getting 3D fit parameters from 2D fits

In Section 4.2.2, we defined the galaxy bias in terms of the coefficients of a real-space power law correlation function, $\xi\,(r)$ (Equation 4.8). However, we are measuring the angular correlation function, $w\,(\theta)$, so we'll need to deproject our angular correlation function to a real-space correlation function. The Limber equation provides the formalism for going the other direction: projecting real-space correlation functions to angular correlation functions with the redshift distribution $N(z)$, the proper mo-

tion distance $D_M(z)$, and the Hubble radius $R_{\rm H}$. Limber (1953) presents the original approximation, which has since been reshaped into a more digestible form (see, e.g., Lee et al. (2006)).

$$w(\theta) = \frac{\int_0^\infty dz N^2(z) \int_{-\infty}^\infty \left[dx/R_{\rm H}(z)\right] \xi\left(\left[D_M(z)\theta\right]^2 + x^2\right)^{1/2}}{\left[\int dz N(z)\right]^2} \tag{4.9}$$

This is very ugly, but not hard to calculate given $\xi(r)$ and an $N(z)$. Conveniently, a power law real-space correlation function, $\xi(r) = (r/r_0)^{-\gamma}$ (Equation 4.7) implies a power law angular correlation function, $w(\theta) = A\theta^{-\beta}$ (Equation 3.8), and the relationship between coefficients of the two power laws can be extracted from the full Limber equation above (see, e.g., Adelberger et al., 2005).

$$\begin{aligned} \beta &= \gamma - 1 \\ A &= \frac{r_0^\gamma B\left[1/2, (\gamma-1)/2\right] \int_0^\infty N^2(z) f^{1-\gamma} g^{-1} dz}{\left[\int_0^\infty N(z') dz'\right]^2} \end{aligned} \tag{4.10}$$

Here, B is the beta function, $g(z) \equiv c/H(z)$ is the change in comoving distance with redshift, $f(z) \equiv (1+z)D_{\rm A}(z)$ is the change in comoving distance with angle,[2] and $D_{\rm A}(z)$ is the angular diameter distance. Note that if the slope β and redshift distribution are held constant, the bias is proportional to the square root of A: $b^2 \propto r_0^\gamma \propto A$.

The Limber equation is set up to project a real-space correlation function to an

[2]Two objects separated by $\Delta\theta$ at redshift z have $f(z)\Delta\theta$ comoving distance between them.

angular correlation function, but it can be used to deproject instead. The equation for A can be analytically inverted, but in practice it's easier to define a function that is the absolute value of the difference between the fitted parameter A and the Limber value of A given β and a guess for r_0. Then you can minimize the difference to find the best r_0.

There is uncertainty in this conversion that comes from not knowing the exact $N(z)$, the selection function in redshift for the objects in the data catalog (Adelberger et al., 2005). This uncertainty arises mainly from the photometric redshift errors, but there is also some uncertainty from the the finite sampling of the $N(z)$ distribution, which limits the precision to which you can determine the true underlying distribution. Adelberger et al. (2005) addresses the uncertainty from the finite sampling of $N(z)$: if $N(z)$ is Gaussian, the relative uncertainty in r_0 can be written in terms of γ and the number of objects in the data catalog, $n_{\rm obj}$:

$$\frac{\sigma_{r_0}}{r_0} = \frac{1}{\gamma\sqrt{2\left(n_{\rm obj}-1\right)}} \tag{4.11}$$

They start with Equation 4.10. If $N(z)$ is a Gaussian, the ratio of $\int N^2(z)dz$ to $\left[\int N(z)\right]^2$ is proportional to the variance of the Gaussian, σ. This means that r_0 is proportional to $\sigma^{1/\gamma}$. The variance on σ is $\sigma_\sigma = \sigma/\sqrt{2\left(n_{\rm obj}-1\right)}$. Propagating uncertainty through the equation $r_0 = C\sigma^{1/\gamma}$ gives you Equation 4.11. This is only the contribution from not knowing the spread of the distribution exactly. Equation

4.11 is a lower limit on the uncertainty in r_0 from the Limber deprojection because it doesn't take into account the uncertainty on the redshifts themselves.

Equations 4.10 let us convert the coefficients of a power law fit to a measured angular correlation function to a the real-space coefficients, r_0 and γ. Equation 4.8 transforms the real-space coefficients into a bias, and Equation 4.3 plus a few definitions and cosmological parameters gives us the halo mass for that bias. This completes our mission. If we can fit our angular correlation function with a power law, we can infer a halo mass.

4.2.4 Caveats

The previous sections have described the pathway from a power law fit to a correlation function to a halo mass. This pathway must be walked with care. The method depends on the proper measurement of the power law coefficients, which we discuss in Section 4.3.2. The method also rests on the proper choice of $N(z)$ for deprojection and the scale-independence of the bias.

The range of separations analyzed should only involve the two-halo term so that the bias measured is the linear bias, and thus scale-independent. If you include the one-halo term, it changes the shape of the correlation function and throws off the fit values. For example, Ouchi et al. (2005) measure the correlation length, r_0, of $z = 4$ Lyman Break Galaxies with a correlation function over 2"$< \theta <$1000". They find $r_0 = 3.8^{+0.2}_{-0.2} h^{-1}$ Mpc, which they contrast with the Giavalisco & Dickinson (2001)

result for a similar sample, $r_0 = 1.0^{+0.8}_{-0.7} h^{-1}$ Mpc. They attribute this difference to the the difference in range in separation. When they refit their correlation functions over 1"$< \theta <$20", the range Giavalisco & Dickinson (2001) use, the result is consistent within the error bars. Both ranges include part of the one-halo term, so the actual value may be different than both results.

4.3 Fitting a power law to the angular CF

Converting correlation functions to masses as described in Section 4.2 begins with a power law fit to a correlation function. Reliable masses require reliable power law fit parameters. Part of this is fitting the right part of the correlation function, but the fitting method also matters. Fits should be stable across reasonable variation in the correlation function, such as small changes in fitting range and the number of bins in separation. Choices for combining fields and integral constraint correction can also affect the mass measurement. In this section, we discuss how to fit a power law to a set of correlation functions robustly.

4.3.1 Fitting procedure

The first step in generating reliable fit parameters is choosing an appropriate fitting mechanism. The two basic classes of fitting mechanism that we'll consider are χ^2-type minimization routines and Markov chain Monte Carlo (MCMC) sampling.

The χ^2-type minimization routines define a distance metric between the data and a function with free parameters. The best fit parameters are those that produce the minimum value of the distance metric. We will be using χ^2 minimization, for which the distance metric is $d = \sum_i((y_{\mathrm{fit,i}} - y_{\mathrm{data,i}})/\sigma_{\mathrm{data,i}})^2$. The χ^2 fitting routine only uses the diagonal elements of the covariance matrix, $\{\sigma_{\mathrm{data,i}}\}$, which can be dangerous if the off-diagonal elements of the covariance matrix are non-negligible. Matthews & Newman (2012) compare fits with only the diagonal elements of the covariance matrix and to fits with the full covariance matrix. They find that the main effect of using the full covariance matrix is to decrease the errors on the amplitude of the power law fit (Equation 3.8). The inferred parameter values also appear to change slightly, but they do not quantify this effect.

MCMC methods are sampling techniques designed to estimate probability distributions by performing a random walk through a parameter space. Generally, the likelihood of measuring a specific data set given a theory is simple to express. Finding the inverse, the likelihood of a theory given the data, is not as simple. MCMC methods take a theory with free parameters and sample the parameter space by making a random walk. Each step is taken only after calculating the likelihood of the data given the set of parameters at the location of the next step. Steps are more likely to be taken from areas of lower likelihood to areas of higher likelihood. The rules for how the random walks are performed ensure that the sample density in the equilibrium state of the MCMC chain corresponds to the probability distribution of

the theory given the data over the parameter space. The location of the largest peak in sample density marks the most likely set of parameters and the width of the peak estimates the uncertainty on the fit. MCMC is much more computationally expensive than minimization routines, but is very good for estimating errors and exploring degeneracies between parameters.

We used an MCMC python package, `emcee`, to fit a correlation function with a power law minus the Adelberger integral constraint. For each point in the $A-\beta$ space, we compute the theoretical correlation function values, $\{y_{\rm fit,i}\}$, for the separations $\{\theta_i\}$ with measured correlation function values. The likelihood function we used is the sum of log probabilities for each data point, which were calculated assuming a Gaussian distribution with mean equal to $y_{\rm fit,i}$ and standard deviation equal to the error bar size for the data at that θ_i.

We show an example MCMC fit in Figure 4.2. The left panel contains the two-dimensional histogram of MCMC samples and the right panel contains the correlation function and fits. The correlation function we are fitting in this example is the Landy-Szalay, single-galaxy bootstrap correlation function of the GOODS-N SHAM between redshifts $1.75 < z < 2.25$. This example looks fairly typical of a CANDELS MCMC fit, with a narrow, banana-shaped ridge that shows the degeneracy between A and β. This particular bin is well fit, so the maximum is fairly localized around $\beta = 0.87$ and $A = 0.0003$. The lime green square shows the center of mass of the distribution. The various points shown are χ^2 minimization fits with various options for β and either

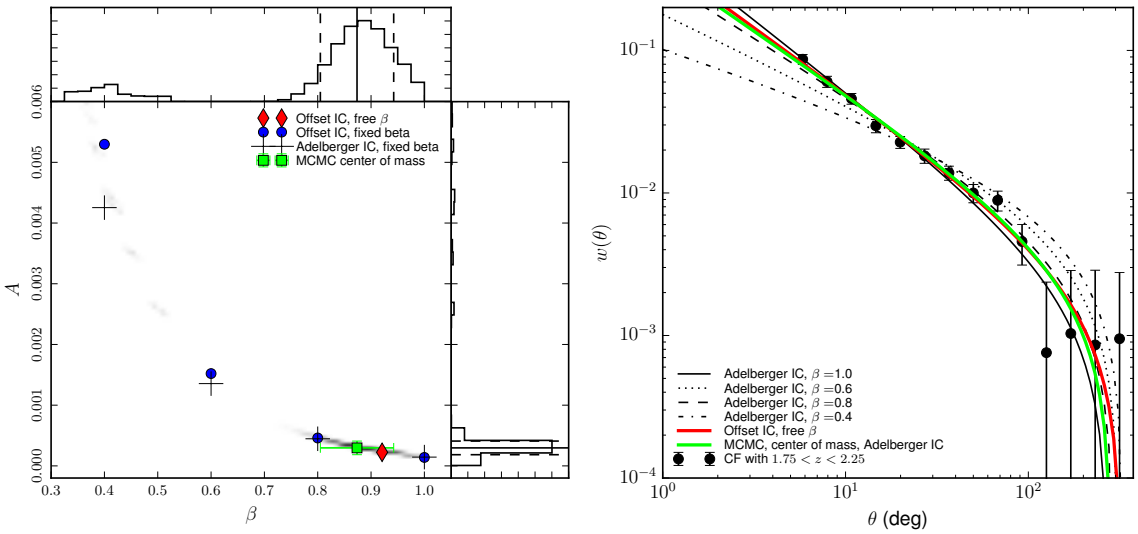

Figure 4.2: Comparison of fits to a correlation function from a SHAM catalog with the GOODS-N field outline. The catalog contains halos with mass $M \geq 10^{10}$ and redshift $1.75 < z < 2.25$. The **left panel** contains the fit values obtained in different ways. The gray shading shows the density of MCMC samples from a fit with an Adelberger integral constraint correction. The lime green square shows the center of mass of the MCMC sample distribution, obtained from the one-dimensional histograms. The blue circles show χ^2 fits to the data with fixed β the integral constraint as a free parameter offset. The black crosses show the χ^2 fits with fixed β and the Adelberger integral constraint. The red diamond shows the best χ^2 fit with β as a free parameter and the integral constraint fit as an offset. The **right panel** shows the correlation function we fit to in the left panel. The points in the left panel correspond to curves in the right. The integral constraint correction varies between fits, so the integral constraint correction is applied to the fits and not to the correlation function.

of the integral constraint options, as noted in the legend. The main thing to note is that all of the fitting options broadly trace the same degenerate ridge in $A - \beta$ space but the fits with the Adelberger integral constraint find a slightly different ridge than the offset integral constraint.

The MCMC samples have to be processed in some way to get a single value of A and β. The ridge of high probability is too curved to successfully fit with a two-dimensional Gaussian distribution. The location of maximum sample density is usually a good estimate of the parameters from the MCMC fit. However, in some cases there are small, high-density peaks along the ridge but far from the bulk of the samples that look like they're due to noise rather than actually being the most likely values. An alternative that finds the center of mass rather than the highest peak is to get the values from the one-dimensional histograms. The projected histogram for β can get a secondary peak at very low values that's due to the relatively low-probability tail stacking up, as seen in Figure 4.2. This can throw off measurements in the one-dimensional histograms. The secondary peak's amplitude is mainly dependent on the extent of the parameter space sampled, not any intrinsic properties of the likelihood space. We found that the best approach was to run the MCMC routine over a wide range in both parameters, then clip off the low density tails. For reproducibility, we used K-means clustering to identify the most clustered N percent of the points and discard the rest. The exact percentage didn't strongly affect the results, but we found that about 80-90% worked well. This procedure produces the lime green fit in Figure

4.2. As you can see, all of the best fits are approximately comparable. **We use the χ^2 minimization** because it is significantly faster than the MCMC sampling and requires no post-processing.

In addition to choosing a fitting algorithm, we must also choose which parameters to fit. In general, authors choose to fix the value of the power law slope, β (e.g. Roche & Eales, 1999; Adelberger et al., 2005; Gawiser et al., 2006; Lee et al., 2006; Barone-Nugent et al., 2014). Adelberger et al. (2005) does this because they find their iterative fitting mechanism to be unstable when β is allowed to vary. Most papers don't discuss their choice to fix β, they simply justify their choice for the value of β: we expect a value of $0.6 \lesssim \beta \lesssim 0.8$ from dark matter simulations. This choice is important. The same correlation function fit with different power law slopes changes the amplitude of the correlation function (and thus the bias and mass). Choosing the wrong β systematically biases the mass estimate, as shown in Figure 4.3. The commonly-used values of the power law slope are 0.6 and 0.8. In this case, the two values differ in inferred mass by about half a dex.

The remedy for this would seem to be fitting β to the data set in question. Unfortunately, fitting β is not a viable option for the CANDELS correlation functions, assuming that the SHAMs are a reasonable analog. We tested this by fitting correlation functions from halos in bins of halo mass. In some cases, the fitting fails to find a viable solution because the correlation functions are too noisy. In the successful cases, the slopes found tend to be too shallow: the biases are too high for the mass

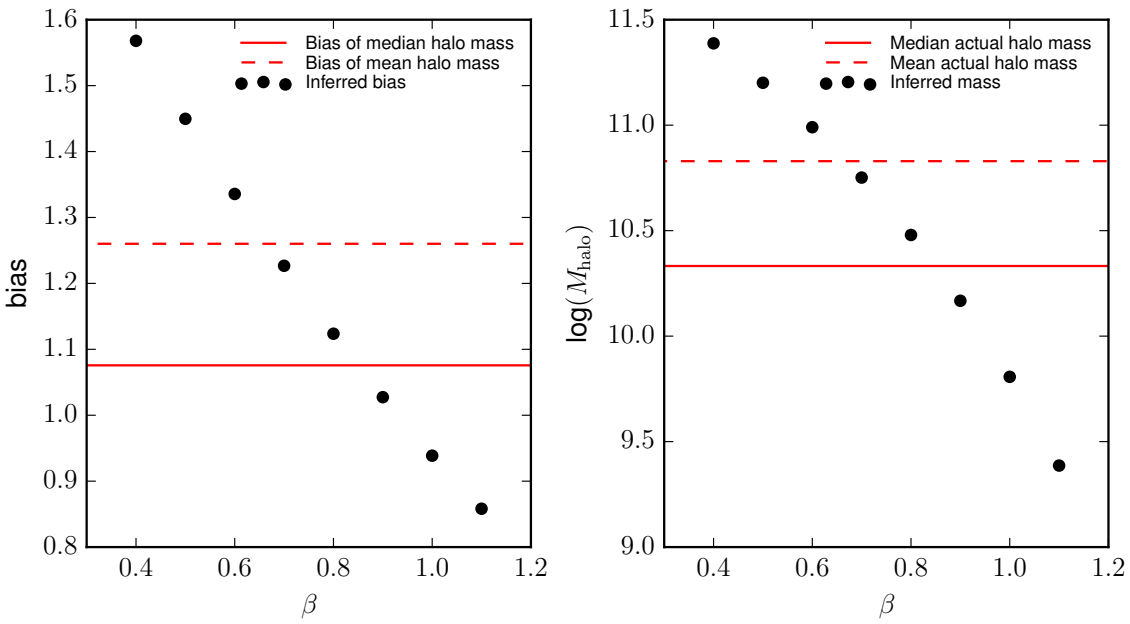

Figure 4.3: Effects of varying the fixed value of β. In the **left panel**, the black points show the bias inferred from χ^2 fits with β fixed to the value on the x axis and the integral constraint as a free parameter offset. The correlation function is the same as the one fit in Figure 4.2. The redshift $z = 2$ Tinker et al. (2010) bias that corresponds to the mean and median actual halo masses in the sample are shown as the dashed and solid lines respectively. The **right panel** shows the mass inferred from the biases in the left panel. The mean and median actual halo masses are shown as the dashed and solid red lines, respectively.

bin in question.

4.3.2 Effects of CF calculation choices

In Chapter 3, we discussed our choices for different aspects of correlation function calculation. In this section, we quantify the effects of correlation function choices on fit parameters. We focus on the correlation function error generation, the number of bins in separation, and the minimum separation. The fits that we show in this section are GOODS-N-shaped cutouts from the SHAM. The entire GOODS-N SHAM field is large enough to fit six CANDELS GOODS-N fields, so we calculated correlation functions for all six to show the parameter variation between fields. The correlation functions are for galaxies in the SHAM with halo mass greater than 10^{10} $M_{\odot}$ with between redshifts $1.75 < z < 2.25$.

In Figure 4.4, we show fit results from the six SHAM GOODS-N fields for correlation functions calculated with different error estimators. The left panel shows results for the amplitude with β fixed at 0.8. These are largely consistent, but the single galaxy bootstrapping seems to yield somewhat lower results. The right panel shows A and β for fits with β as a free parameter. Again, the three are similar but the single galaxy bootstrapping is somewhat apart from the others. Between these results and the findings in the literature that single galaxy bootstrapping doesn't reproduce external error estimates, we chose to use block bootstrapping for the final correlation functions.

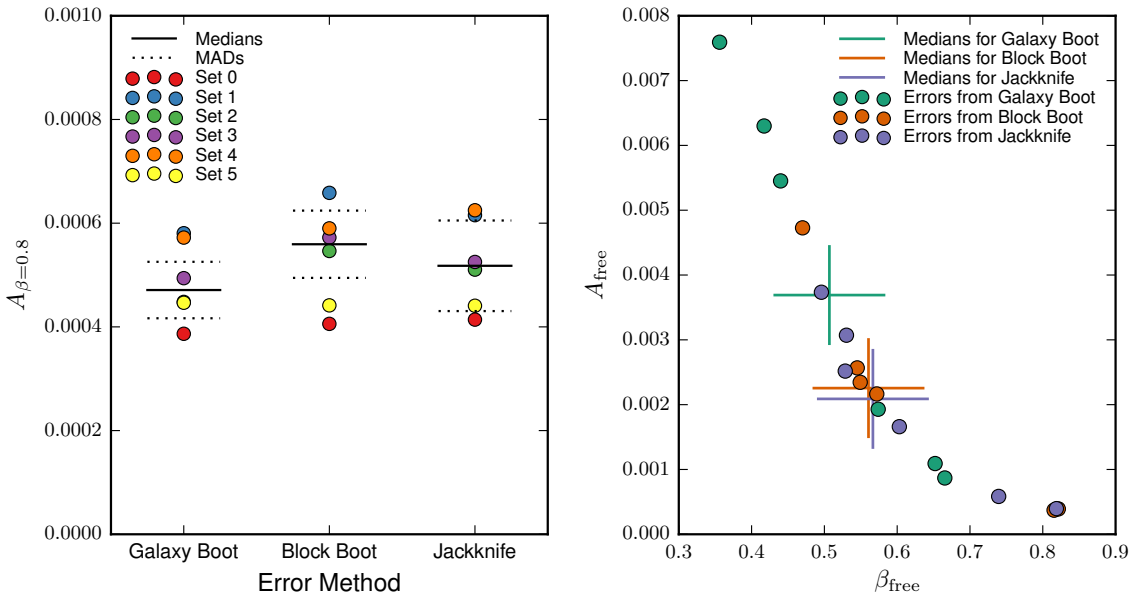

Figure 4.4: Fit parameters vs. error estimation method for six independent SHAM GOODS-N fields fit with the integral constraint as a free parameter offset. **Left panel:** amplitude for fixed β=0.8 for the different three error methods. The colors of the points show which of the fields the fit is for and the horizontal black lines show the medians for each error method. Dotted black lines show the median absolute deviation. **Right panel:** fit parameters with β fit to the correlation function, still with the integral constraint as a free parameter offset. In this plot, the color of the points denotes which error method is used. The crosses show the medians for each error method.

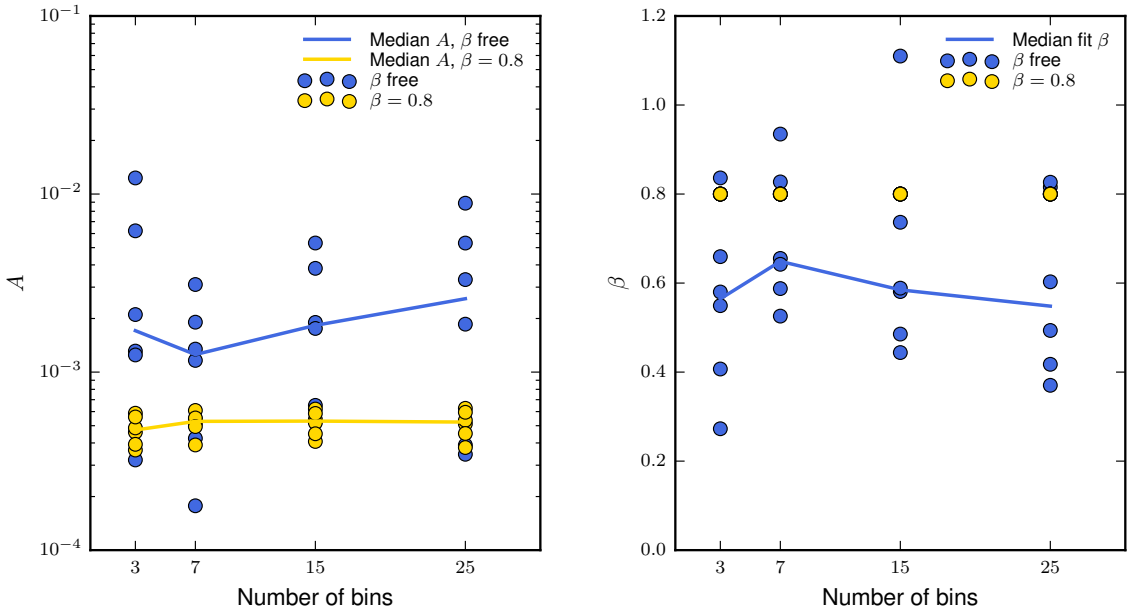

Figure 4.5: Fit parameters vs. number of bins in separation for six independent SHAM GOODS-N fields. The blue points show results for β fit to the correlation function and the gold points show β fixed to β=0.8. The **left panel** shows the amplitude, A, and the **right panel** shows the slope β. In both panels, the median fit values are shown with lines.

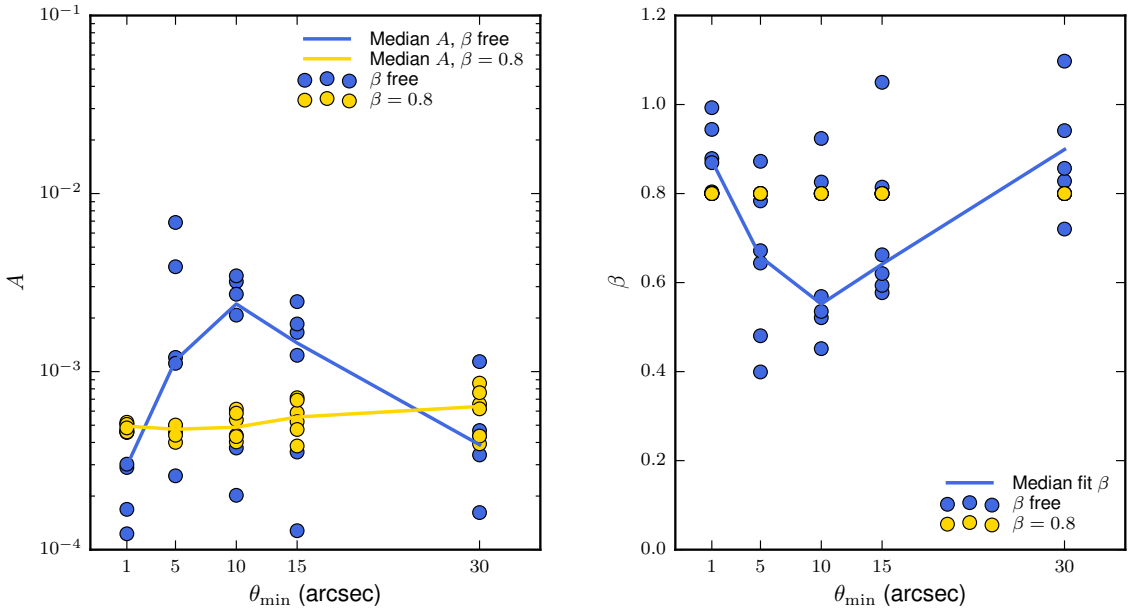

Figure 4.6: Fit parameters as a function of minimum separation for six independent SHAM GOODS-N fields. The blue points show results for β fit to the correlation function and the gold points show β fixed to β=0.8. The **left panel** shows the amplitude, A, and the **right panel** shows the slope β. In both panels, the median fit values are shown with lines.

In Figure 4.5, we show fit parameters for the six SHAM GOODS-N fields from correlation functions with different numbers of bins in separation, all covering 10"$<$ θ $<$350". The amplitude is shown in the left panel and the β in the right. The fits with β as a free parameter, shown in blue, have a slight dependence on the number of bins, but with fixed β, the amplitude is consistent between all of the numbers of bins.

In Figure 4.6, we show the effect of the minimum separation on the fit values, again for both β=0.8 and β fit as a free parameter. The minimum separation has a much larger effect on the end value than the error calculation method or the number

of bins. This is to be expected for a correlation function that is not a pure power law. The dependence on the minimum separation is present both for β fit to the correlation function and fixed to 0.8, but is much stronger if β is allowed to vary. The value we use for the CANDELS correlation functions is the middle value, $\theta_{\rm min}$=10". This is slightly smaller than the scale that Kravtsov et al. (2004a) cite as the transition between the one- and two-halo terms. Kravtsov et al. (2004a) find that 0.3 comoving h^{-1}Mpc is a safe minimum separation for including only the two-halo term at all redshifts. This corresponds to about 15" at redshift $z = 2$, as shown in Figure 4.7. We compared the fit parameters for the CANDELS fields with $\theta_{\rm min}$=10", our standard choice and that of Ouchi et al. (2005) and Lee et al. (2006), and $\theta_{\rm min}$=70", which is greater than or equal to 1 comoving h^{-1}Mpc, well beyond any influence of the two-halo term over the majority of redshifts examined. We show this comparison in Figure 4.8. The two fits are largely consistent within errors, so we do not expect our measurements to be biased by our choice of $\theta_{\rm min}$.

The integral constraint correction changes the normalization of the correlation function, so it has the potential to affect the amplitude A of the fit. In Figure 4.9, we compare the amplitudes for fits to the CANDELS fields with the two kinds of integral constraint corrections. The two are consistent within the error bars.

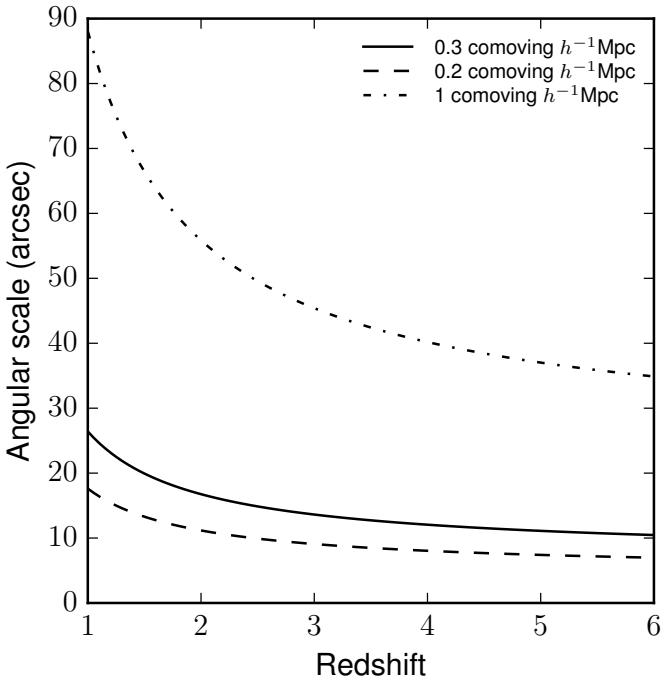

Figure 4.7: Angular scale of three comoving distances, 0.2, 0.3, and 1 h^{-1}Mpc, as a function of redshift.

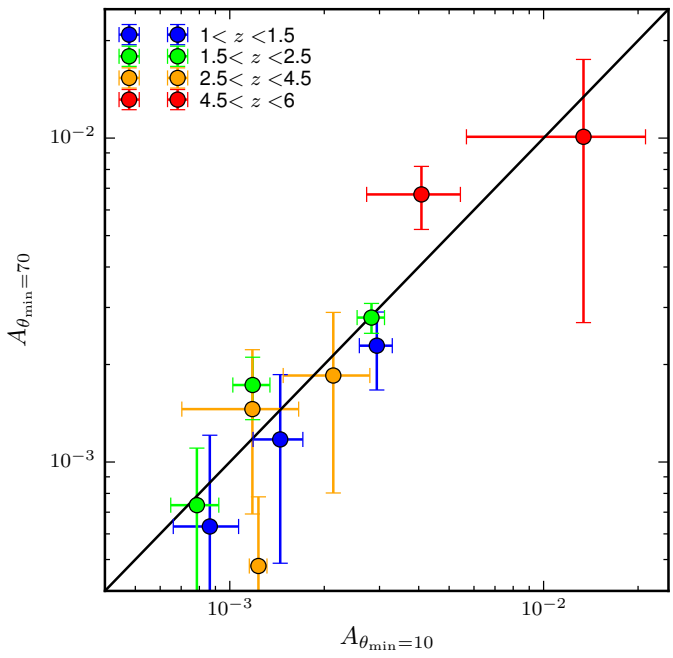

Figure 4.8: Amplitudes for fits to the CANDELS correlation functions with $\theta_{\rm min}$=10" on the x-axis and $\theta_{\rm min}$=70" on the y-axis. Both sets of fits were done with the integral constraint as a free parameter offset, block bootstrap errors, and β=0.8. Error bars are from the field bootstrap procedure (see Section 4.3.3). Point colors differentiate between redshifts.

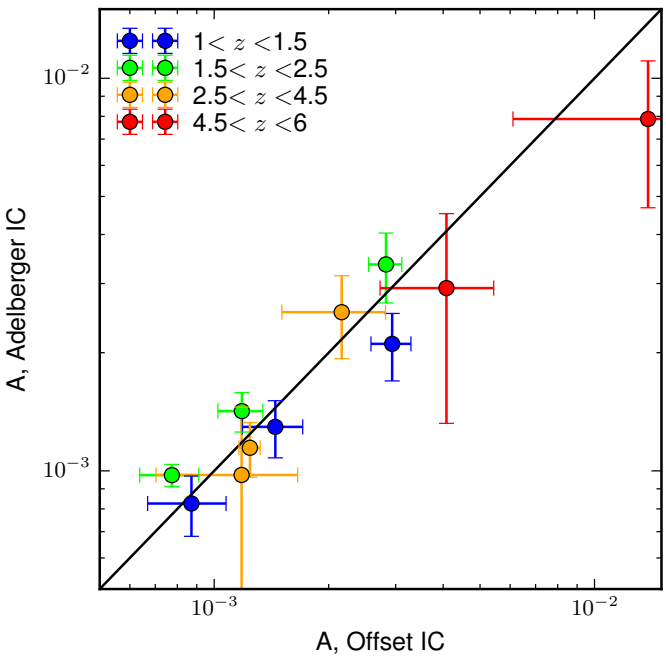

Figure 4.9: Amplitudes for fits to the CANDELS correlation functions with the offset integral constraint on the x-axis and the Adelberger integral constraint on the y-axis. Both sets of fits were done with block bootstrap errors and β=0.8. Error bars are from the field bootstrap procedure (see Section 4.3.3). Point colors differentiate between redshifts.

4.3.3 Error estimation on fit parameters

The error on fit parameters comes from both the error on the correlation function and the uncertainty of the fit itself. Uncertainty on the correlation function propagates to uncertainty on the fit parameters, but even a perfectly-measured correlation function would have somewhat uncertain fit parameters. The fitting algorithm is looking for an extremum in either the log likelihood or a distance measure and the wider the extremum, the harder it is to locate. Noise in the data interferes with pinpointing the exact location of the extremum (Andrae et al., 2010). We discuss the error on the correlation function in Section 3.5. In this section, we discuss the errors on the fit parameters assuming that the errors on the correlation functions are accurate.

There are two basic types of error estimation available when fitting a function to data. One is examining the extremum in the likelihood or distance metric that the fitting algorithm is trying to find. This is simple in the case of an MCMC fit because the samples returned trace the log likelihood, so the fit uncertainty is described by the size and shape of the sample density peak. The peak is somewhat curved (see the left panel of Figure 4.2), so the errors are more complicated than a single error for each parameter or even a full covariance matrix, which describes a multidimensional Gaussian distribution. The most basic approximation is to find the center of the sample density peak and extract the median absolute deviation (MAD) from the one-dimensional histograms. This doesn't account for any of the co-dependence of

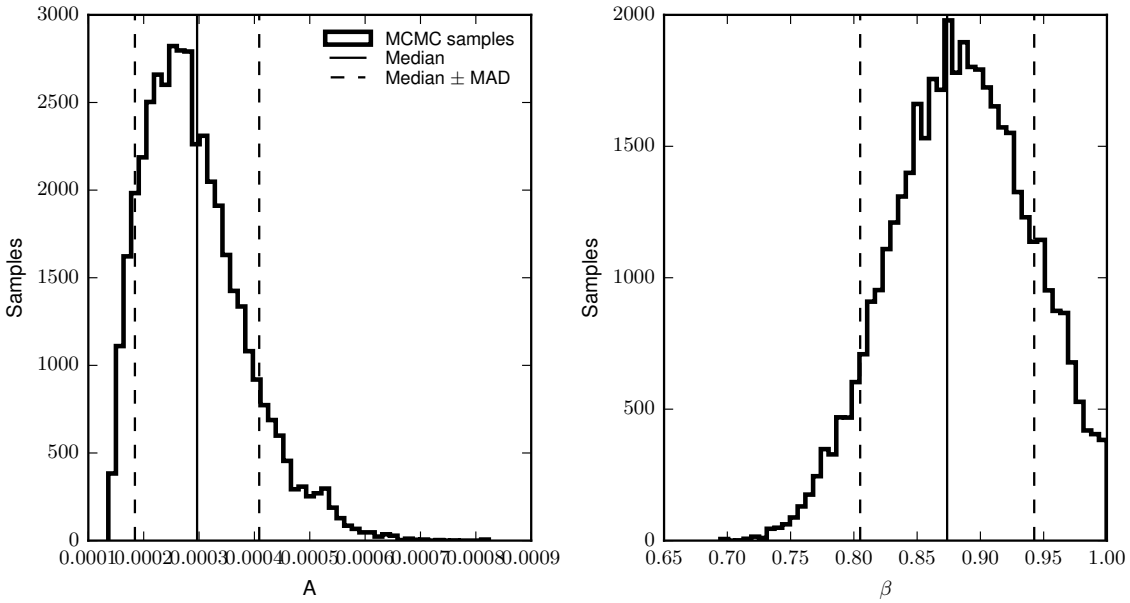

Figure 4.10: One-dimensional histograms of the trimmed MCMC samples from the example shown in Figure 4.2. The median and median absolute deviation are shown as vertical solid and dashed lines, respectively. The trimming is done by using K-means clustering to identify the main peak, then including the closest K-means clusters such that 80% of the samples are included. This excludes the low-probability tails that cause secondary peaks, which can be seen in Figure 4.2.

the parameters, but suffices as a quick-and-dirty estimate of the error. Figure 4.2 shows the sample density for the MCMC fits with the fit and errors from the one-dimensional histograms, trimmed as described in Section 4.3.1, shown in lime green. Figure 4.10 shows the histograms trimmed to the center 80% with the median and MAD shown as vertical lines. Note that the secondary peaks present in the one-dimensional histograms of Figure 4.2 have been removed by the trimming process.

A similar procedure can be used with χ^2 fitting, examining the value of the distance metric instead of sample density over parameter space, but the width of the minimum is more difficult to quantify since χ^2 can become arbitrarily large. In Figure 4.11, we show the $\log(\chi^2)$ as a function of A and β for the same range in parameters that Figure 4.2 shows for the MCMC fit. The left panel shows the χ^2 with an offset integral constraint and the right panel shows χ^2 with the Adelberger integral constraint. The crosses mark the minima of χ^2. Both are highly degenerate, but the Adelberger integral constraint tends to have a higher χ^2 because it has fewer free parameters. One thing to note about the intrinsic fitting uncertainty is that the uncertainties are only large if both A and β are allowed to vary. For a given value of β, the value of A tends to be well-constrained. Because we fix β to fit the CANDELS correlation functions, error from correlation function uncertainty and cosmic variance dominates and we neglect the smaller fitting error.

The second type of error estimation is an internal error estimate, similar to the error estimation on the correlation function itself (see Section 3.5). This estimates

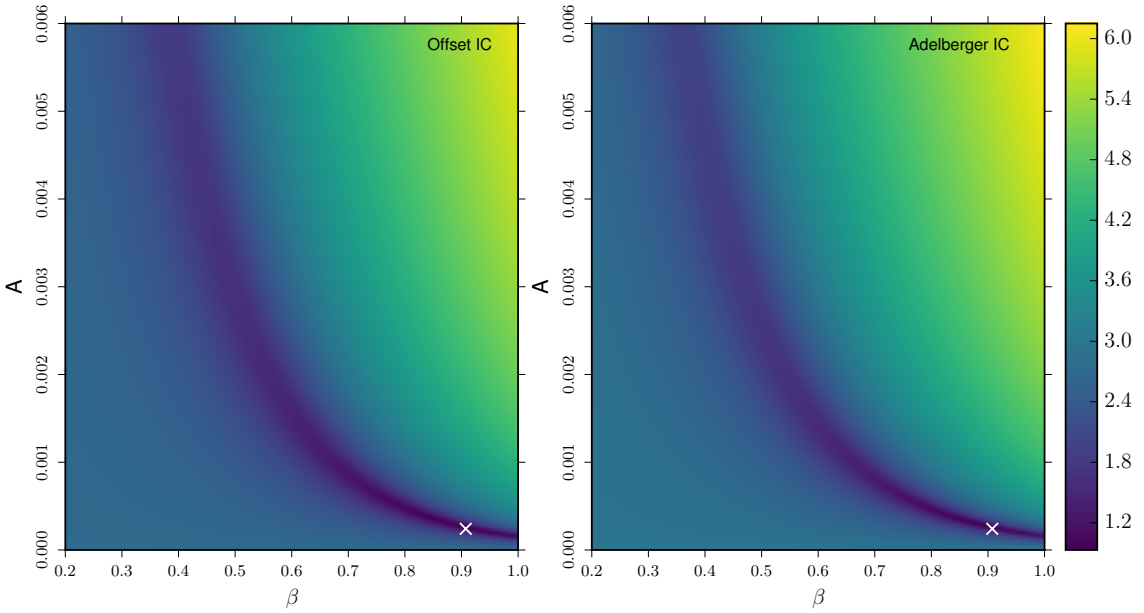

Figure 4.11: Value of $\log(\chi^2)$ as a function of A and β for a free parameter offset integral constraint (left panel) and the Adelberger integral constraint (right panel). The minima in χ^2 are marked by the crosses. The correlation function fit is described and shown in Figure 4.2.

the uncertainty due to cosmic variance. The version of this error estimator that we use requires multiple fields, but other schemes, similar in spirit, could be used on other surveys. The fitting algorithm is fed a single correlation function with errors: the average of the individual field's correlation functions with the error bars on each point determined through error propagation. There are of course alternatives to this, but this method works best for CANDELS (see Section 3.8). To estimate the error, instead of fitting just once to the evenly weighted average of all the fields we draw five fields' correlation functions from the set with replacement, average them, propagate errors, and fit. We repeat this, performing a sort of "field bootstrapping" procedure. The value of the fit parameter can either be taken from the median of the bootstrap fits or from the values of the unweighted average. The two are essentially identical. The error on that value is the width of the distribution, which we estimate with the median absolute deviation.

4.3.4 Methods we use

In this section, we've discussed the different options for fitting to the correlation functions that we calculated in Chapter 3. We fit to the angular correlation functions calculated in seven logarithmically spaced bins of separation over $10'' \leq \theta \leq 350''$. The fit parameters we use are from a field bootstrapped χ^2 fit with a fixed β and the integral constraint fit as a free parameter offset. The values for the fit parameters are the values from the fit to the evenly-weighted average of all five fields. This unweighted

fit does not differ greatly from the median value from the field bootstrapping: the largest difference in for the CANDELS fits is 3.2%. The error bars are the median absolute deviation between the bootstraps, multiplied by 1.48 to be equivalent to the 1σ Gaussian error.

Since multiple values of beta are used in the literature, we calculate the amplitude and integral constraint offset for a range of β values and hold off on deciding which to use until we examine the accuracy of the mass measurements. We ultimately settle on β=0.8, so we present the β=0.8 fit parameters and the fits with β as a free parameter for comparison in Table 4.1. In Figure 4.12, we show the CANDELS correlation functions for galaxies with H-band magnitudes brighter than 26th magnitude with the final power law fits. The correlation functions are shown as calculated and the integral constraint correction has been included in the fit.

4.4 Masses from fit parameters

In Section 4.3, we showed how to get reliable power law fit parameters from angular correlation functions. In this section, we discuss deprojecting the fit parameters with the Limber equation, converting fit parameters to a bias with Equation 4.8 and then to a mass using the Tinker et al. (2010) $b\left(M_{\rm halo}\right)$ relation. We test our methods on the SHAM catalogs (see Section 3.2), where the halo masses are known. We find that our best estimates for the angular power law fit parameters result in biases that are too

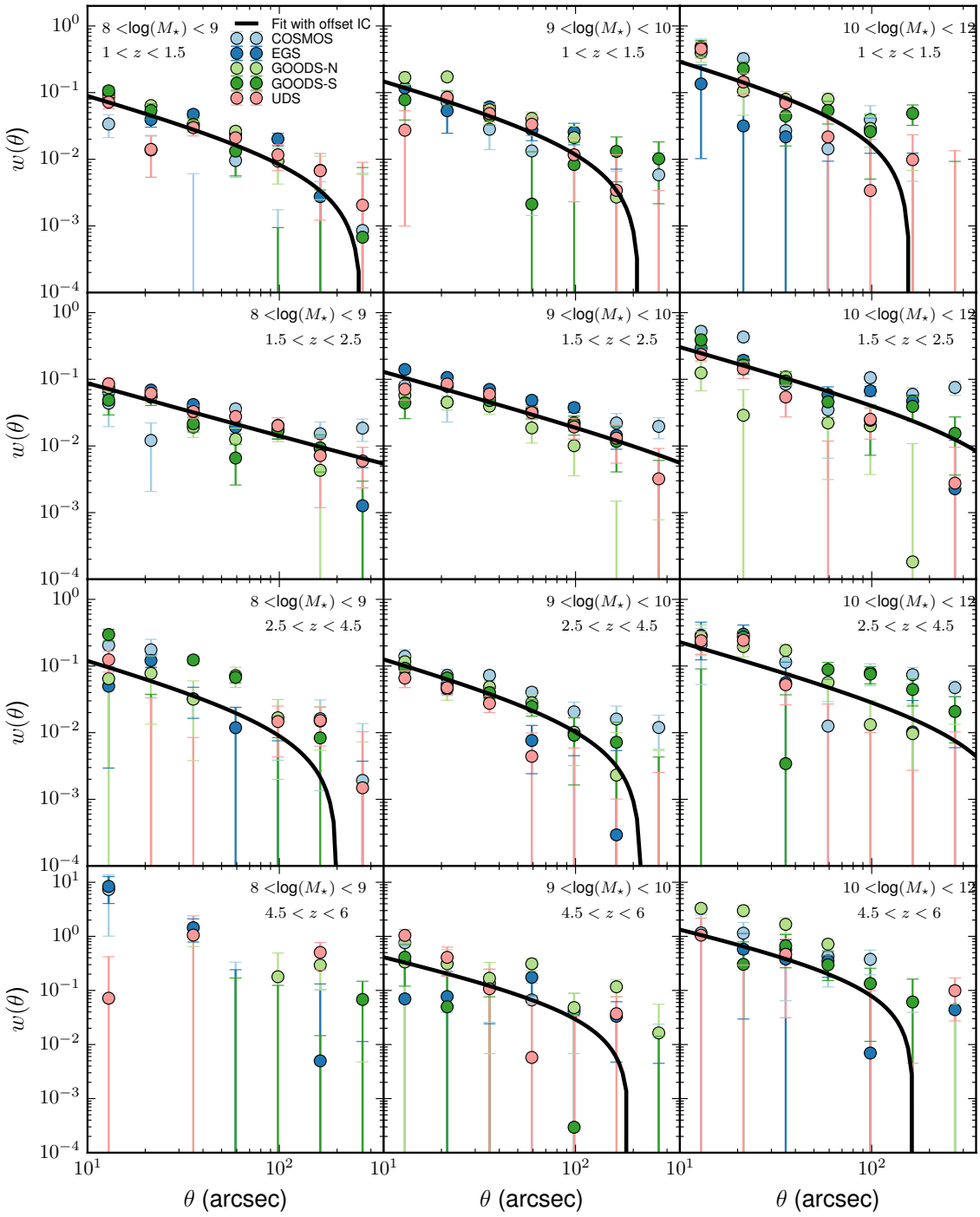

Figure 4.12: CANDELS correlation functions in bins of mass and redshift with only galaxies with H-band magnitudes greater than 26. Black lines show χ^2 fits with fixed β=0.8 and a free parameter offset. The lowest mass, highest redshift bin is not populated well enough to fit. Rows correspond to redshift bins, columns to mass bins.

$M_\star$ bin	z bin	$(A \pm \sigma_A)/(1e\text{-}3)$ $\beta = 0.8$	$(A \pm \sigma_A)/(1e\text{-}3)$ β free	$\beta \pm \sigma_\beta$ β free
$8 < \log(M_\star) < 9$	$1 < z < 1.5$	0.87 ± 0.2	0.8 ± 0.81	0.81 ± 0.21
	$1.5 < z < 2.5$	0.77 ± 0.14	2.5 ± 1.9	0.59 ± 0.14
	$2.5 < z < 4.5$	1.2 ± 0.48	0.0068 ± 0.041	1.8 ± 1.0
	$4.5 < z < 6$	–	–	–
$9 < \log(M_\star) < 10$	$1 < z < 1.5$	1.4 ± 0.26	4.5 ± 4.7	0.6 ± 0.18
	$1.5 < z < 2.5$	1.2 ± 0.16	32.0 ± 26.0	0.28 ± 0.1
	$2.5 < z < 4.5$	1.2 ± 0.08	1.1 ± 0.57	0.82 ± 0.097
	$4.5 < z < 6$	4.1 ± 1.4	1.0 ± 1.5	1.1 ± 0.66
$10 < \log(M_\star) < 12$	$1 < z < 1.5$	2.9 ± 0.35	0.056 ± 0.069	1.6 ± 0.32
	$1.5 < z < 2.5$	2.8 ± 0.28	0.093 ± 0.1	1.4 ± 0.29
	$2.5 < z < 4.5$	2.2 ± 0.66	0.12 ± 0.19	1.4 ± 0.44
	$4.5 < z < 6$	14.0 ± 7.7	9.0 ± 12.0	0.88 ± 0.43

Table 4.1: Fit values for the CANDELS fields with χ^2 minimization and the integral constraint fit as a free parameter offset. Fit values are presented for β=0.8 and β fit as a free parameter.

high, so we use the simulations to correct the biases so that our mass measurements on the simulations match the known halo masses.

4.4.1 Fit parameters to bias

To derive bias from angular correlation function fits, we deproject our angular fit parameters to real-space parameters with the Limber equation and use Equation 4.8 to get the bias, as discussed in Section 4.2.3. The main adjustable parameter in converting angular fit parameters to bias is the form of the redshift distribution, $N(z)$. The width of the slice in redshift directly affects the inferred correlation length, r_0, and bias. The slice width, Δz, is essentially a distance: the larger the Δz, the deeper the volume selected. Things that are widely separated in space are less

correlated than things that are nearby, so an angular correlation function over a very wide slice in redshift appears less correlated than the angular correlation function of the same population for a smaller slice in redshift. In a wide redshift slice, the largely uncorrelated pairs of galaxies dilute the signal from physically close pairs. The Limber equation takes this into account, so if the Limber equation assumes narrow $N(z)$ when the reality is a wider $N(z)$, the inferred bias will be too low because it will assume less signal dilution than there actually is. Conversely, if the $N(z)$ used is wider than the actual $N(z)$, the inferred bias will be too high because the signal dilution will be overestimated.

We demonstrate the effect of using the incorrect $N(z)$ in Figure 4.14. The correlation function we use is still the same example shown in Figure 4.2, taken from halos in a SHAM GOODS-N field with redshifts $1.75 < z < 2.25$ and halo mass $M_{\rm halo} \geq 10^{10}$. The true $N(z)$ is shown in Figure 4.13, along with the top hat approximation in red. We calculate the bias and mass with the top hat $N(z)$ closest to the actual distribution as well as top hat $N(z)$s that are 1.5 or 2 times smaller or larger than the actual distribution. The locations of the edges of the incorrect top hat $N(z)$s are shown by the vertical blue lines along the x-axis in Figure 4.13. The biases and masses derived with this set of top hat $N(z)$s are shown in Figure 4.14. The wider the $N(z)$, the more biased/massive and the narrower the $N(z)$, the less biased/massive. A factor of two in $N(z)$ width changes the bias by about a factor of $\sqrt{2}$. When the $N(z)$ is too narrow by a factor of two, this decreases the mass by a factor of about 33 and

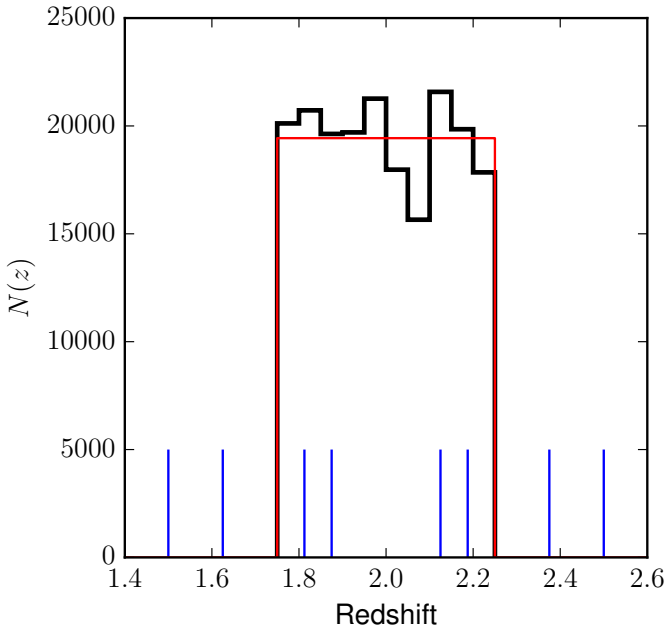

Figure 4.13: True $N(z)$ for our example SHAM bin shown in black with the top hat $N(z)$ shown in red. The wider and narrower bin edges are shown as blue vertical lines.

when the $N(z)$ is too wide by a factor of two, this increases the mass by a factor of about 9.

To check the sensitivity of this method to the choice of $N(z)$, we test the conversion of fit parameter to bias on the SHAM. In the SHAM, the $N(z)$ is simple to calculate because we know the exact redshifts of all of the halos. Our selection function is a top hat: we choose all of the galaxies with redshifts between a lower limit and an upper limit. The actual redshift distribution is not a top hat, however, since the number of galaxies in the simulated field of view is not constant with redshift. In fact, the redshift distributions are different for each mass bin since the number density as a function of redshift is different for each bin in mass. Figure 4.15 shows

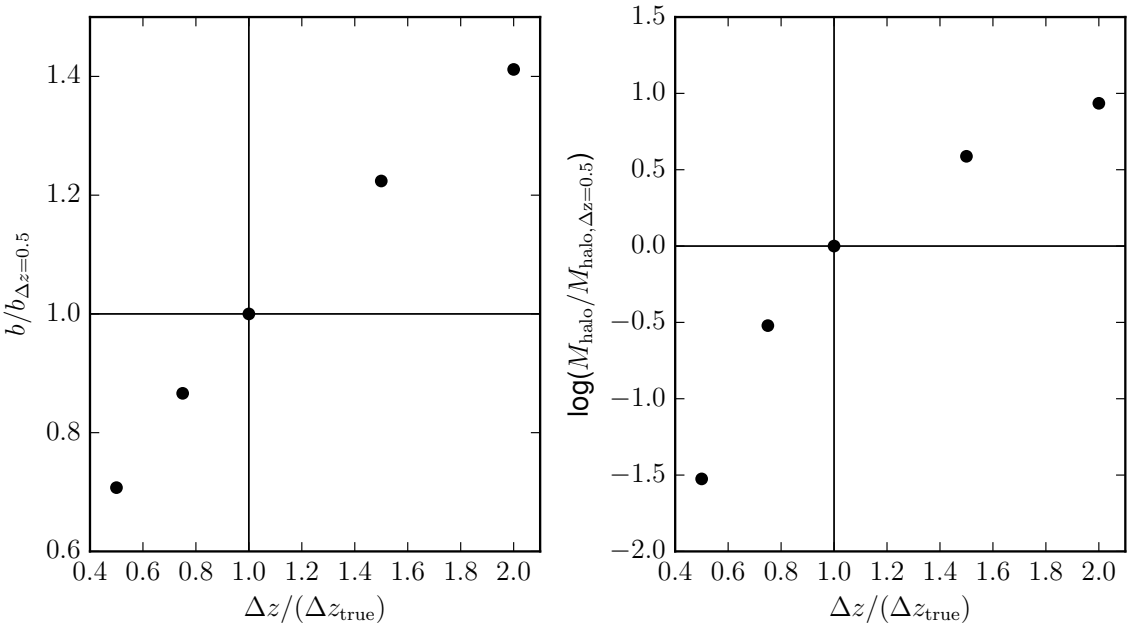

Figure 4.14: Effects of using a wider or narrower $N(z)$ on the bias and mass. **Left panel:** bias as a function of the redshift bin width used to the true redshift bin width. The larger the value on the x-axis, the wider the $N(z)$ used relative to the actual distribution. The points show the ratio of the derived bias for the same fit but different $N(z)$ widths to the bias for the correct bin width. **Right panel:** the log of the ratio of the derived mass with different $N(z)$ widths to the true mass as a function of bin width relative to the true bin width.

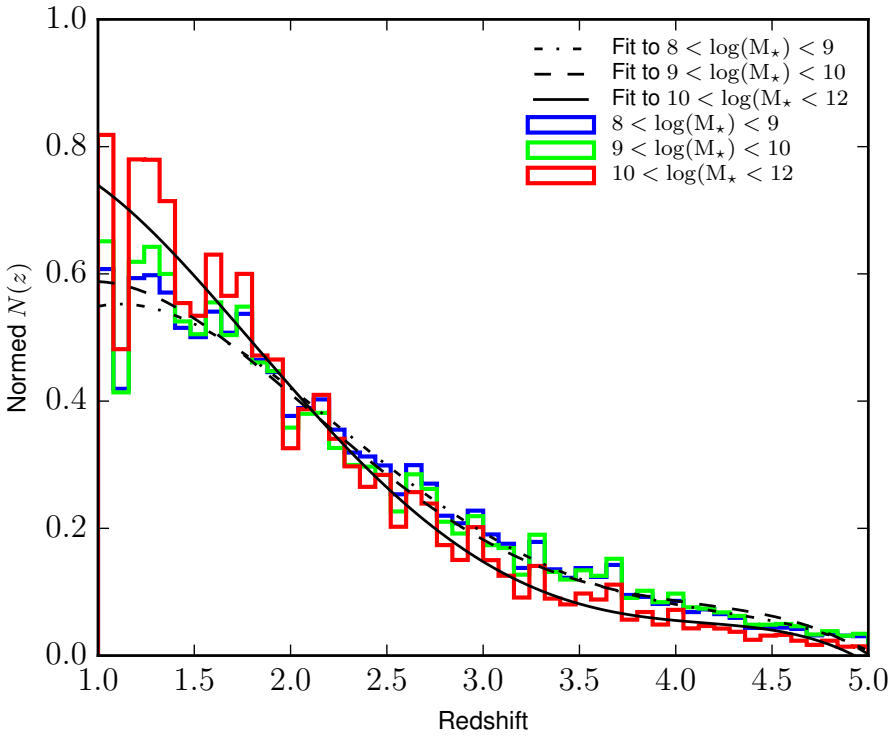

Figure 4.15: Redshift distributions of halos in the SHAM catalogs in bins of stellar mass. The normalized histograms of redshifts is shown in blue, green, and red for mass bins $8 < \log(M_\star) < 9$, $9 < \log(M_\star) < 10$, and $10 < \log(M_\star) < 12$ respectively. The dot-dashed, dashed, and solid lines are fourth order polynomials fit to the redshift distributions and normalized to match the histogram amplitude.

the actual redshift distributions for the SHAM in bins that reproduce the CANDELS bins as closely as possible. The colored histograms are the normalized redshifts in bins of stellar mass from abundance matching and the black lines show fourth order polynomial fits to each bin. We compared the results of using a top hat $N(z)$ to using the true $N(z)$ distribution, represented by a top hat times the polynomial fit to the appropriate mass bin. We find that a top hat $N(z)$ gives us basically the same masses as the top hat times the polynomial, as shown in Figure 4.16.

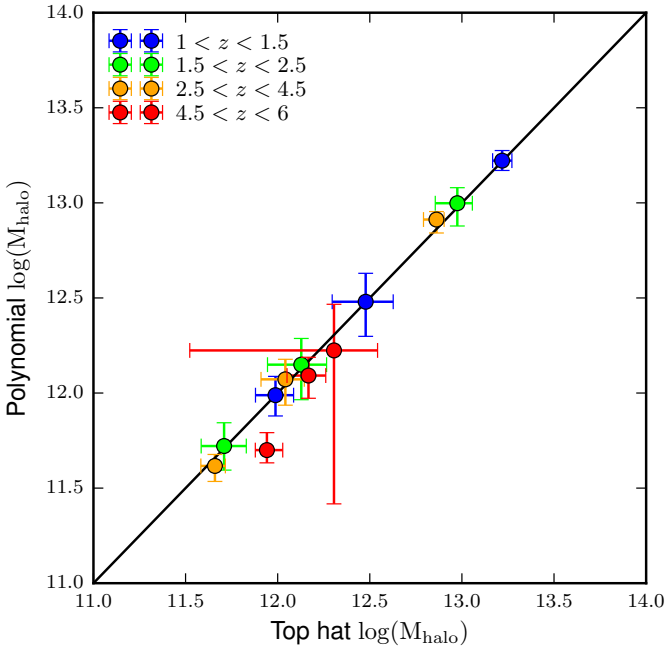

Figure 4.16: Differences between masses obtained with the top hat $N(z)$ on the x-axis and the polynomial fit $N(z)$ on the y-axis. The color of the points corresponds to the halo mass bin.

Because we only have photometric redshifts for the galaxies in CANDELS, the top hat $N(z)$ is probably not a good approximation. The best estimate that we have for the true $N(z)$ is generated by the SED fitting. Along with a final photometric redshift, SED fitting routines generate probability distribution functions (PDFs) for the redshifts of each galaxy (Kodra et al. 2016, in preparation). We can use these to get an idea of what the true $N(z)$ looks like for each bin.

To estimate both $N(z)$ and the uncertainty on $N(z)$ that comes from combining the PDFs, we use the median of 200 bootstrap resamplings of the PDFs from galaxies in each bin. For each bootstrap, we average together the PDFs selected with replacement. After computing all of the bootstrap $N(z)$s, we take the median value at each redshift to be the $N(z)$. We show these $N(z)$s in Figure 4.17. Note the secondary peaks at low redshift for the higher redshift bins. This is an inherent problem with photometric redshifts: red objects at low redshift can be difficult to distinguish from galaxies at high redshift. With these more realistic $N(z)$ distributions, we can now convert the CANDELS fit parameters to biases, listed in Table 4.3.

4.4.2 Corrections to the derived bias

A simple consistency check of our method is to compare the biases we get from the SHAM to the biases we expect for halos of that mass at that redshift. The bias we expect for halos in a bin with any width in mass or redshift is not a single number because bias is a function of both mass and redshift. In order to compare the single

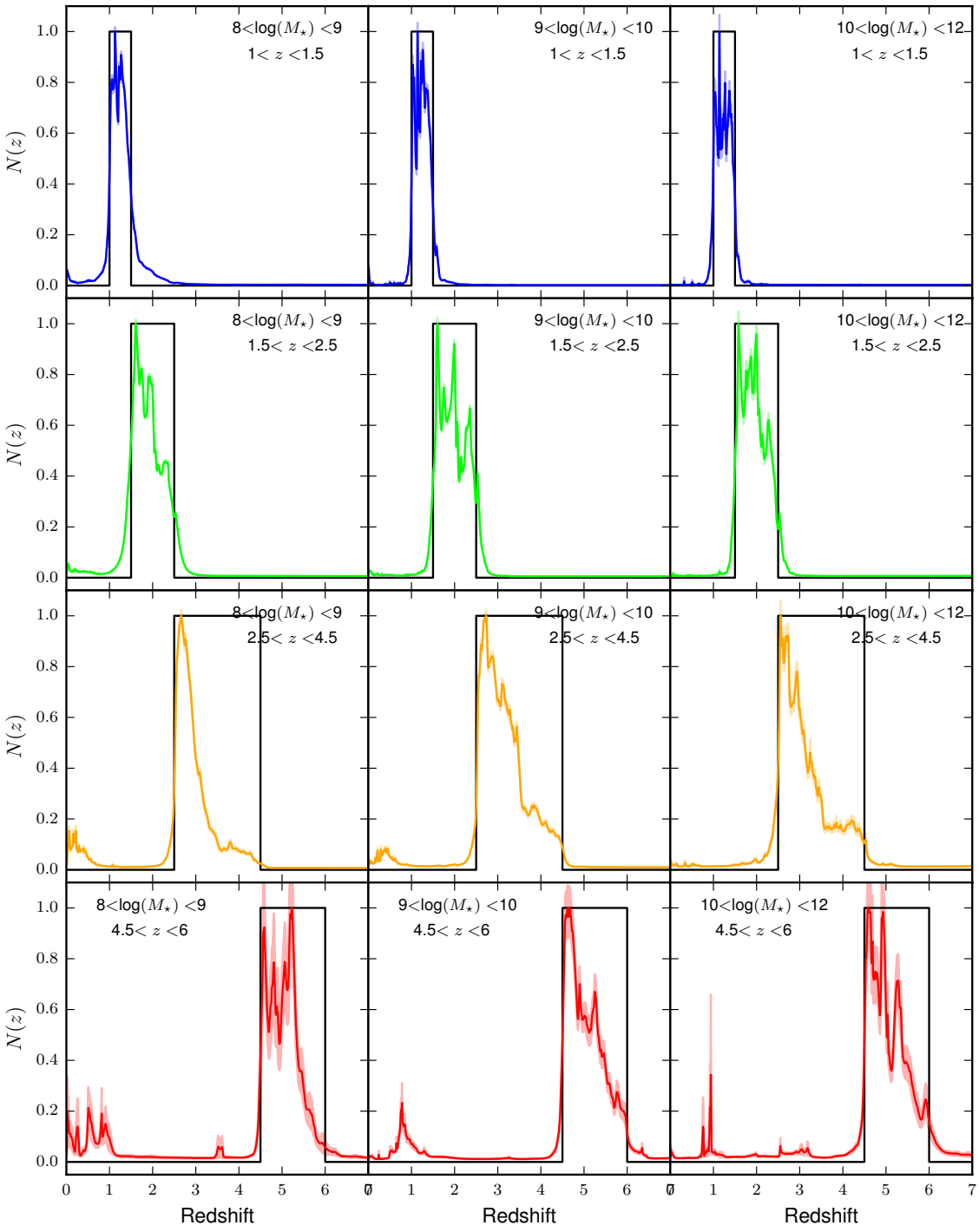

Figure 4.17: Normalized $N(z)$s from photometric redshift probability distribution functions. The center line in each panel is the median value of the bootstraps. Each bootstrap is the average of PDFs drawn with replacement from the PDFs in that bin of stellar mass and redshift. The shaded region around the center line shows the standard deviation of the $N(z)$ values at that redshift.

bias that we get from the correlation functions to the "true" bias, we must choose a single mass and redshift to be truth. We use the median halo mass and redshift to calculate the true bias from the Tinker et al. (2010) $b\,(M_{\rm halo})$ relation.

For this comparison, we calculated the biases from correlation functions of SHAM galaxies. We used two different samples, which we call the "fine grid" and the "coarse grid." The coarse grid matches the CANDELS observations as closely as possible, using CANDELS field outlines and the same stellar mass and redshift bins. The stellar masses in the SHAMs come from the Behroozi et al. (2013a) abundance matching procedure. The fine grid uses the same redshift bins but is separated into fifteen mass bins. The mass bins run from $\log(\mathrm{M}_\star) = 6.5$ to $\log(\mathrm{M}_\star) = 9$ in bins of width 0.25 dex, then from $\log(\mathrm{M}_\star) = 9$ to $\log(\mathrm{M}_\star) = 11$ in bins of width 0.5 dex. The last bin covers $11 < \log(\mathrm{M}_\star) < 12$. In order to have enough halos in each fine grid bin, we use the entire SHAM fields rather than CANDELS field outlines. This is about six or seven times the area of the CANDELS fields. Despite having a larger area, we still calculate correlation functions from 10"$< \theta <$350".

In 4.18, we show the comparison between the derived biases, calculated from the correlation functions, and the true halo bias. The left panel of Figure 4.18 compares the two biases directly with the one-to-one line in the solid black and the two-to-one line in dotted black. While the derived and true biases are nicely correlated, the derived biases are much closer to being twice the actual bias then they are to matching. The right panel shows $\Delta b = b_{\rm obs} - b_{\rm true}$, the difference between the derived bias and the

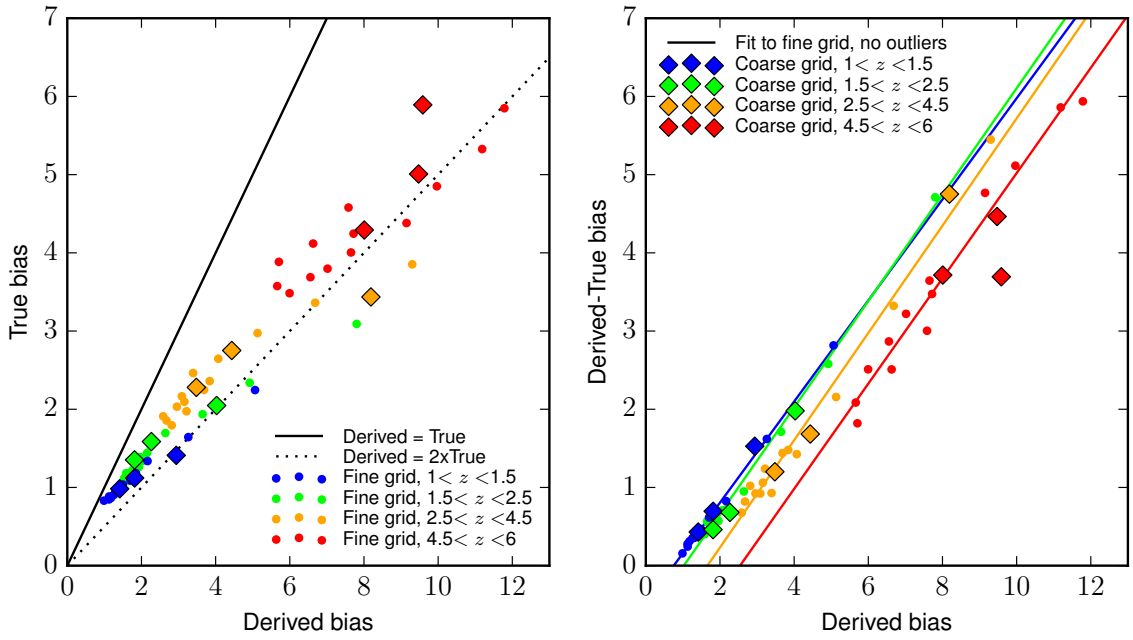

Figure 4.18: Comparison of the true bias to the derived bias for two different sets of SHAM measurements. The small circular points are from the fine grid, measured over the entire SHAM fields for narrow bins in stellar mass. The large diamonds are from the coarse grid, which mimics the CANDELS observation area and binning. Point color denotes redshift bin. **Left panel:** true bias vs. derived bias. The solid black line shows the one-to-one line, where derived bias is equal to true bias and the dotted black line shows the two-to-one line where the derived bias is twice the actual bias. **Right panel:** difference between derived and true bias as a function of derived bias. The points are as in the left panel and the lines are linear fits to the fine grid results at each redshift, excluding outliers.

z bin	m	C
$1 < z < 1.5$	0.646	-0.487
$1.5 < z < 2.5$	0.680	-0.698
$2.5 < z < 4.5$	0.686	-1.140
$4.5 < z < 6$	0.673	-1.711

Table 4.2: Linear fits to $\Delta b\,(b_{\rm obs})$, where $\Delta b\,(b_{\rm obs}) = b_{\rm obs} - b_{\rm true} = m b_{\rm obs} + C$.

true bias. The relationship between derived bias and the Δb, the function $\Delta b\,(b_{\rm obs})$, appears conveniently linear. To correct the biases we derive for the CANDELS fields, we fit $\Delta b\,(b_{\rm obs})$ as a linear relationship between derived bias and Δb. We fit to the fine grid for each bin in redshift, excluding outliers by only including bins with $-5 < \Delta b < 15$. These fits are shown in the right panel of Figure 4.18 as solid lines with colors that correspond to the redshift bin. We list the parameters for these fits in Table 4.2.

Figure 4.19 compares the actual bias to the corrected bias. On the left, it shows the correction with fits to the coarse grid and on the right it shows the correction with fits to the fine grid, excluding outliers (only using points with $-5 < \Delta b < 15$). We choose to use the fits to the fine grid (right panel) because the small number of points in each redshift bin in the coarse grid means that each point has a large amount of leverage over the final result. For instance, the overall relation in both fine and coarse grids seems to have about the same slope in the right panel of Figure 4.18, but the fit to the coarse grid for the highest redshift bin is almost horizontal because of the two bins with similar derived biases. Both coarse and fine grids seem to lie on the

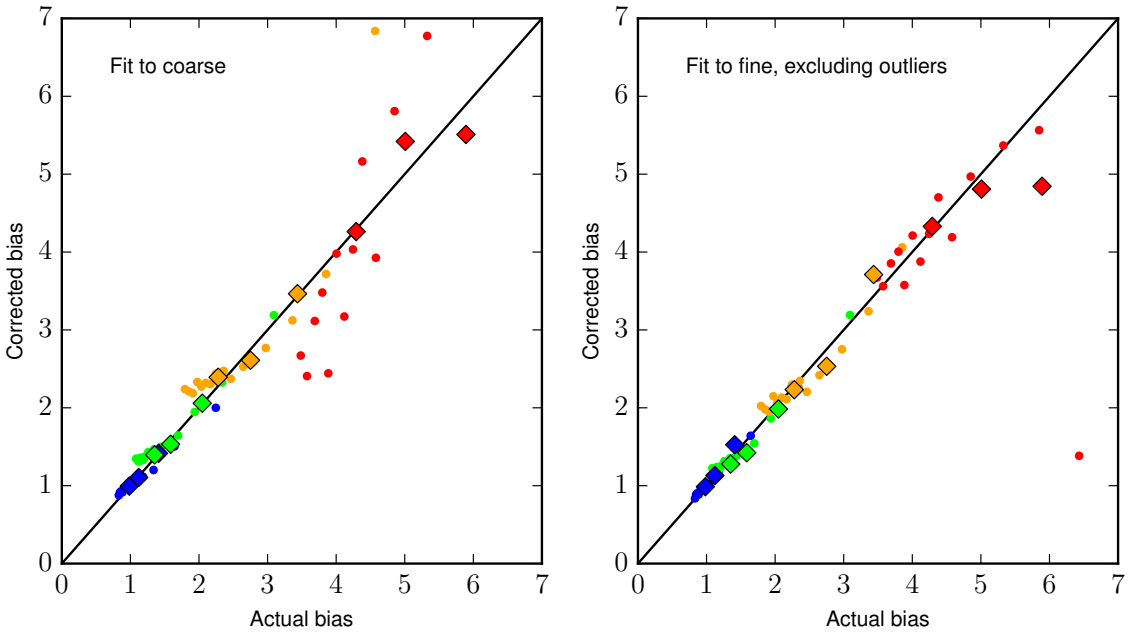

Figure 4.19: Derived biases corrected with linear fits to the $\Delta b\,(b_{\rm obs})$. **Left panel:** corrected biases with linear fits to the coarse grid only. **Right panel:** corrected with linear fits to the fine grid only, excluding outliers.

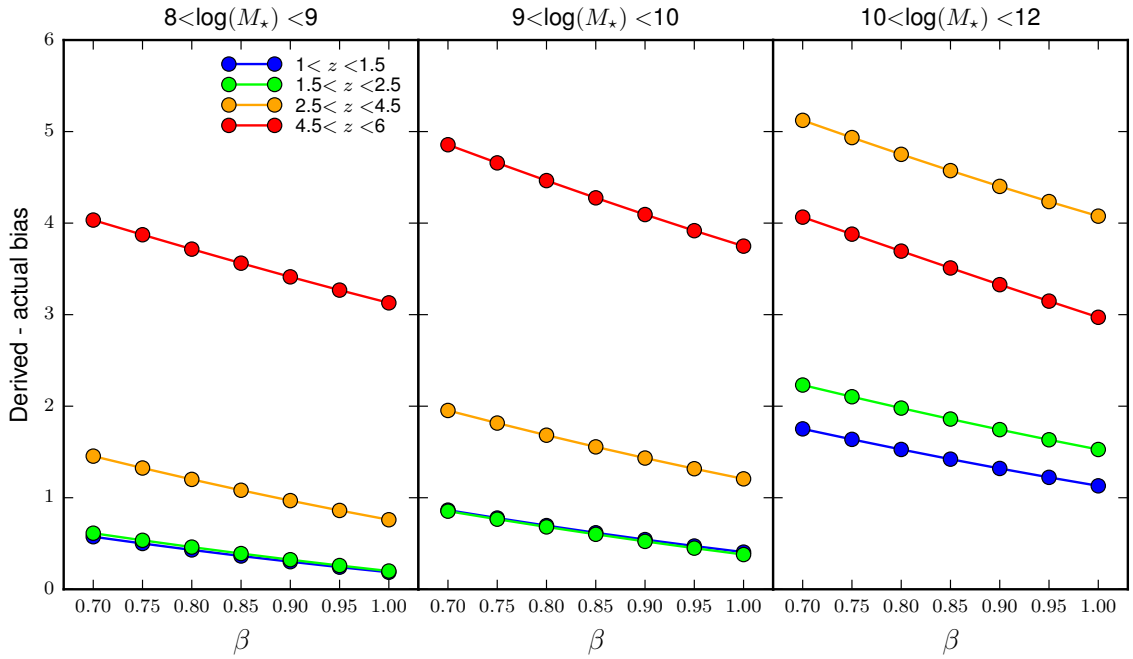

Figure 4.20: Difference between derived and true bias for the coarse grid with different values of β. Each panel is a stellar mass bin with the range of masses above each panel. The colors denote redshift.

same $\Delta b\,(b_{\rm obs})$, so we fit to the grid for which we have more information.

The derived bias depends on the value of β that we choose, so we tried several values of β. The hope was that the mass estimates would be correct for a reasonable value of β, but we find that no reasonable β matches in any bin of mass or redshift. In Figure 4.20, we show the Δb as a function of β for a different mass bin from the coarse grid in each panel. The colors denote redshifts. The bias does change with β, but no value of $\beta \leq 1$ matches any bin. In addition, there are still trends with mass and redshift, so the value of β would have to be different for every bin. It is cleaner to use β=0.8 and correct with the linear $\Delta b\,(b_{\rm obs})$. We show the corrected CANDELS biases in Figure 4.21 and list corrected and uncorrected biases in Table 4.3.

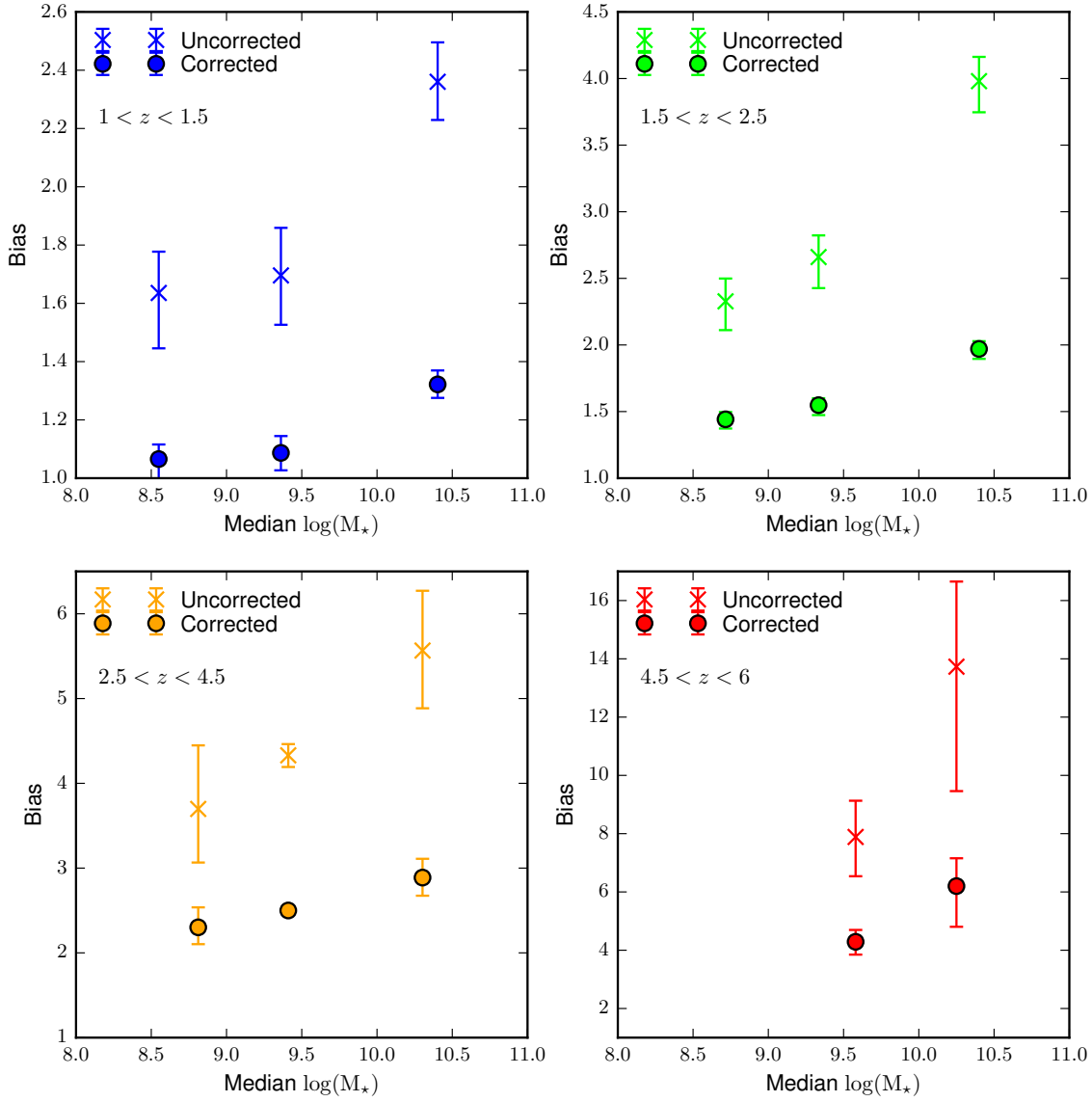

Figure 4.21: Corrected and uncorrected biases for all the bins in mass and redshift for the CANDELS correlation functions with valid power law fits. The stellar mass on the x-axis is the median stellar mass for the galaxies in the bin.

The reason that this process requires such extreme correction is unclear, but there are a number of aspects of the calculation that could bias the mass high.

1. **Field size**

   The CANDELS fields are all relatively small compared to low redshift surveys and cosmic variance effects (and thus integral constraint corrections) are stronger for smaller fields. This is unlikely the source of our problem, however. To do the bias correction, we used correlation functions from the SHAM as close as possible to our CANDELS bins, including the field outlines. However, we also ran much smaller mass bins over the entire SHAM fields, which is 6 or 7 times as much area. The bias corrections for both methods look about the same (Figure 4.18). The maximum separation, $\theta_{\rm max}$, may have some influence on the results and is limited by field size. The $\theta_{\rm max}$ for the fine grid was held to 350" to match the CANDELS correlation functions.

2. **Artificial clustering from the completeness cut**

   Our choice to use only galaxies brighter than the 90% completeness limit of the shallowest depth could potentially affect the biases we derive from CANDELS galaxies, but the problem is present in the SHAMs, which do not have such potential difficulties.

3. **Inclusion of the one-halo term**

   We do fit to scales smaller than the radii of the largest clusters, which is about 1

comoving h^{-1}Mpc. This scale corresponds to 90" at redshift $z = 1$, decreasing 35" at $z = 6$ (see Figure 4.7), a larger scale than our minimum separation over the entire redshift range. However, Kravtsov et al. (2004a) find that the one-halo term is only significant at radii smaller than 0.3 comoving h^{-1}Mpc, which is about 15" for most of our redshift range. To test for one-halo term contamination, we generated correlation functions over 70"$< \theta <$350", which is comfortably outside the 0.3 comoving h^{-1}Mpc at all redshifts in our range. This change does not affect our results (see Figure 4.8).

4. **Choice of β**

   The values of A and β are highly degenerate, so choosing a β that is too low would bias our results towards higher masses. The value of β that we choose, 0.8, is on the high end of the expected values. In Figure 4.20, we show the excess bias as a function of β. The excess bias does indeed change with β, but even β=1 leaves a large redshift- and mass-dependent excess bias. The values of β from fits with β as a free parameter give values in the 0.5 to 0.6 range, and no one expects values of β larger than 1. Also, no single value of β with eliminate all of the excess bias for all masses and redshifts. Correcting the problem with β only would require an unrealistically steep slope that is dependent on both mass and redshift.

5. **Integral constraint correction**

The integral constraint correction does affect the fitting, but not significantly enough to change the mass so drastically. Differences between the Adelberger integral constraint and the free parameter offset integral constraint are significant mainly at low values of β (see points in the left panel of Figure 4.2). Figure 4.9 compares fits to the CANDELS data with fixed β=0.8 for both the Adelberger and the free parameter offset integral constraint corrections. The two are consistent within the error bars.

6. **Correlation function isn't actually a power law**

   If the two-halo term isn't a power law, fitting it with one is unlikely to generate the correct results, let alone do so robustly. This may be the case; Figure 4.6 shows that the slope, fit as a free parameter, varies significantly as the minimum separation changes. The power law shape of the two-halo term is common in the literature and seems to be fairly well supported. For instance, Ouchi et al. (2005) find that the bias as calculated with a ratio of correlation functions approaches a single value at scales larger than 10", which shows that their correlation function has the same shape as the dark matter correlation function, which is a power law.

7. **Deprojection with the incorrect** $N(z)$

   Using an $N(z)$ that is too wide will bias results to higher masses. This cannot be the root of the problem because using the true redshift distribution on the

SHAM does not fix the problem (see Figure 4.16). Our bias correction assumes that the $N(z)$ used is the correct one, so the problem that we are correcting for is not caused by $N(z)$.

8. **Bins span a range of mass and redshift, so the expected bias is not a single number**

   In simulations, the bias is a function of halo mass and redshift. Each of our bins spans a significant range in both quantities, but the derived bias is only a single number. When we tested the technique in Section 4.4.2, we used the median halo mass and redshift, which may not be the correct choice. The measured bias is expected to represent the most common halos in the bin, which are the lower mass and redshift halos. We measure biases that are too high, which would indicate either a higher mass or a higher redshift than we are assuming, contrary to the expectation that the measured bias is representative of the most common halos.

Most of the options we presented above are not likely to be the culprit and none of them can be addressed within the power law bias technique with the CANDELS fields. Our maximum separation is determined by the field shape, which cannot be altered. The other two options listed that could affect our outcome are the shape of the two-halo term diverging from a power law and the mixing of biases from different halo masses and redshifts. These could be addressed with a halo occupation distribution, but are not something that can be accounted for while still deriving a single bias from

$M_\star$ bin	z bin	$\log(\mathrm{M}_{\star,\mathrm{med}})$	z_{med}	$b_{\mathrm{raw}} \pm \sigma_{b_{\mathrm{raw}}}$	$b_{\mathrm{corr}} \pm \sigma_{b_{\mathrm{corr}}}$
$8 < \log(\mathrm{M}_\star) < 9$	$1 < z < 1.5$	8.55	1.25	$1.6^{+0.14}_{-0.19}$	$1.1^{+0.05}_{-0.07}$
	$1.5 < z < 2.5$	8.72	1.78	$2.3^{+0.17}_{-0.22}$	$1.4^{+0.05}_{-0.07}$
	$2.5 < z < 4.5$	8.81	2.79	$3.7^{+0.75}_{-0.63}$	$2.3^{+0.24}_{-0.20}$
	$4.5 < z < 6$	8.78	5.02	–	–
$9 < \log(\mathrm{M}_\star) < 10$	$1 < z < 1.5$	9.36	1.25	$1.7^{+0.16}_{-0.17}$	$1.1^{+0.06}_{-0.06}$
	$1.5 < z < 2.5$	9.33	1.94	$2.7^{+0.16}_{-0.23}$	$1.5^{+0.05}_{-0.07}$
	$2.5 < z < 4.5$	9.41	3.04	$4.3^{+0.13}_{-0.14}$	$2.5^{+0.04}_{-0.04}$
	$4.5 < z < 6$	9.58	4.98	$7.9^{+1.24}_{-1.35}$	$4.3^{+0.41}_{-0.44}$
$10 < \log(\mathrm{M}_\star) < 12$	$1 < z < 1.5$	10.40	1.24	$2.4^{+0.14}_{-0.13}$	$1.3^{+0.05}_{-0.05}$
	$1.5 < z < 2.5$	10.40	1.92	$4.0^{+0.18}_{-0.23}$	$2.0^{+0.06}_{-0.07}$
	$2.5 < z < 4.5$	10.30	2.96	$5.6^{+0.71}_{-0.68}$	$2.9^{+0.22}_{-0.21}$
	$4.5 < z < 6$	10.25	4.93	$13.7^{+2.92}_{-4.27}$	$6.2^{+0.96}_{-1.4}$

Table 4.3: Uncorrected ("raw") biases and corrected biases for the bins in mass and redshift in the CANDELS fields.

a power law fit to a correlation function.

4.4.3 Measured masses

Once we have corrected the biases, the conversion to halo mass is simple: we take the $b\,(M_{\mathrm{halo}})$ relation from Tinker et al. (2010) at the median redshift of the galaxies in our bin and find the halo mass that corresponds to the corrected bias. This is our measured halo mass and should be approximately the median halo mass for that bin. In Section 4.2.1, we discuss the theory behind the relationship between bias and halo mass, $b\,(M_{\mathrm{halo}})$. The $b\,(M_{\mathrm{halo}})$ we use from Tinker et al. (2010) is a fitting function to halos in a dark matter simulation (Equation 4.3). This fitting function is in terms

of ν, defined as $\nu = \delta_c/\sigma\,(M)$, where δ_c is the critical over-density for collapse, taken to be 1.686, and $\sigma\,(M)$ is the variance in density on scales of $R = [3M/4\pi\rho_0]^{1/3}$. We can calculate $\sigma\,(M)$ with Equation 4.1 and the relationship between R and M.

When we convert in this way for the SHAMs, we find masses that are largely consistent with the actual median halo masses in the bins. We show the corrected and uncorrected results in Figure 4.22. The uncorrected masses tend to be between 0.5 and 1 dex high, while the corrected masses are generally in agreement with the median halo mass. We generate the error bars by correcting all of the biases generated by the field bootstrapping procedure, converting each to a mass, then finding the 16th and 84th percentiles of the bootstrapped masses. There is also error associated with the bias correction which we have not quantified. With the errors as they are, some excess mass remains in the corrected halo masses at lower masses and redshifts. This suggests that the bias correction may be slightly nonlinear, though a more complete characterization of the error is required to say if the divergence from linearity is statistically significant.

We show the corrected and uncorrected results from the CANDELS galaxies in Figure 4.23, compared to the Behroozi et al. (2013a) $M_\star\,(M_{\rm halo})$ relation. Our corrected results agree with the Behroozi et al. (2013a) results, while the uncorrected results disagree significantly. Again, the error bars on the halo masses are only from the field bootstrapping procedure and should be taken as lower limits on the error. The bias correction does not apply equally at all stellar masses. This is seen most

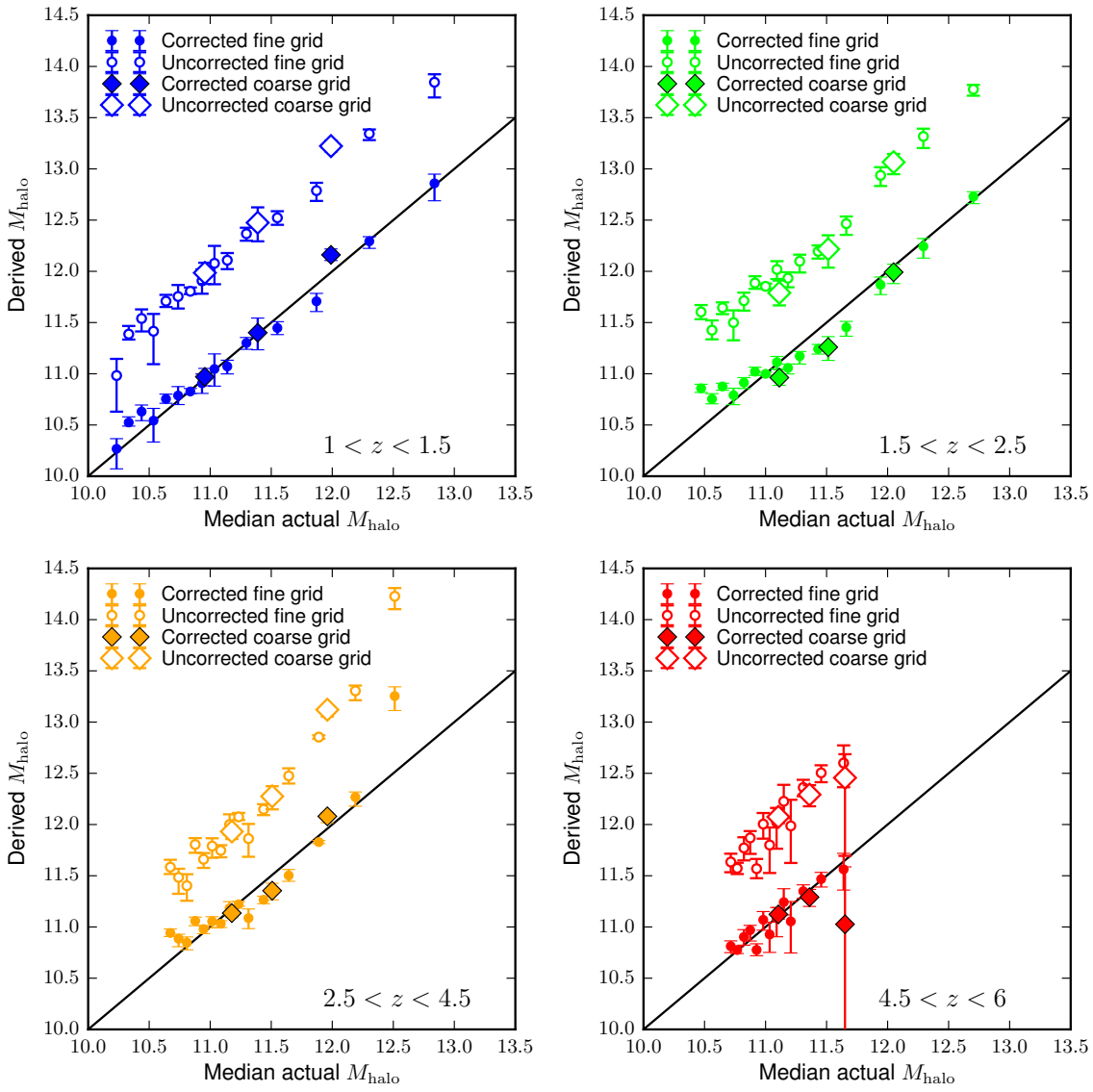

Figure 4.22: Halo mass derived from correlation functions in the SHAMs compared to the actual median halo masses. Each panel shows all of the SHAM bins both corrected (filled symbols) and uncorrected (open symbols). The fine grid is shown as circles and the coarse grid as wide diamonds. The black lines show where derived mass is equal to true mass.

$M_\star$ bin	z bin	$\log(\mathrm{M}_{\star,\mathrm{med}})$	z_{med}	$\log(\mathrm{M}_{\mathrm{halo,raw}})$	$\log(\mathrm{M}_{\mathrm{halo,corr}})$
$8 < \log(\mathrm{M}_\star) < 9$	$1 < z < 1.5$	8.55	1.25	$12.30^{+0.16}_{-0.25}$	$11.24^{+0.14}_{-0.22}$
	$1.5 < z < 2.5$	8.72	1.78	$12.37^{+0.11}_{-0.17}$	$11.43^{+0.09}_{-0.12}$
	$2.5 < z < 4.5$	8.81	2.79	$12.26^{+0.27}_{-0.29}$	$11.46^{+0.18}_{-0.18}$
	$4.5 < z < 6$	8.78	5.02	–	–
$9 < \log(\mathrm{M}_\star) < 10$	$1 < z < 1.5$	9.36	1.25	$12.36^{+0.17}_{-0.21}$	$11.30^{+0.16}_{-0.18}$
	$1.5 < z < 2.5$	9.33	1.94	$12.44^{+0.09}_{-0.15}$	$11.42^{+0.08}_{-0.12}$
	$2.5 < z < 4.5$	9.41	3.04	$12.31^{+0.04}_{-0.05}$	$11.41^{+0.03}_{-0.03}$
	$4.5 < z < 6$	9.58	4.98	$12.04^{+0.20}_{-0.27}$	$11.10^{+0.15}_{-0.19}$
$10 < \log(\mathrm{M}_\star) < 12$	$1 < z < 1.5$	10.40	1.24	$12.92^{+0.08}_{-0.09}$	$11.85^{+0.08}_{-0.09}$
	$1.5 < z < 2.5$	10.40	1.92	$13.02^{+0.06}_{-0.08}$	$11.94^{+0.05}_{-0.07}$
	$2.5 < z < 4.5$	10.30	2.96	$12.71^{+0.15}_{-0.17}$	$11.73^{+0.12}_{-0.14}$
	$4.5 < z < 6$	10.25	4.93	$12.80^{+0.21}_{-0.43}$	$11.72^{+0.21}_{-0.40}$

Table 4.4: Uncorrected ("raw") halo masses and corrected halo masses for the bins in stellar mass and redshift in the CANDELS fields.

clearly in the lower left panel, with the results from redshift $2.5 < z < 4.5$. The lower two stellar mass bins show the expected behavior in the uncorrected case: the higher stellar mass bin has a higher median halo mass. In the corrected case, the middle stellar mass bin has lower halo mass than the lowest stellar mass bin. This happens because the median redshifts in the two bins are different: 2.787 in the low mass bin and 3.043 in the middle stellar mass bin, a difference of $\Delta z = 0.256$. The bias correction is comparable, but the difference in the $b\,(M_{\mathrm{halo}})$ relation is such that the mass correction is larger for the middle stellar mass bin at higher redshift.

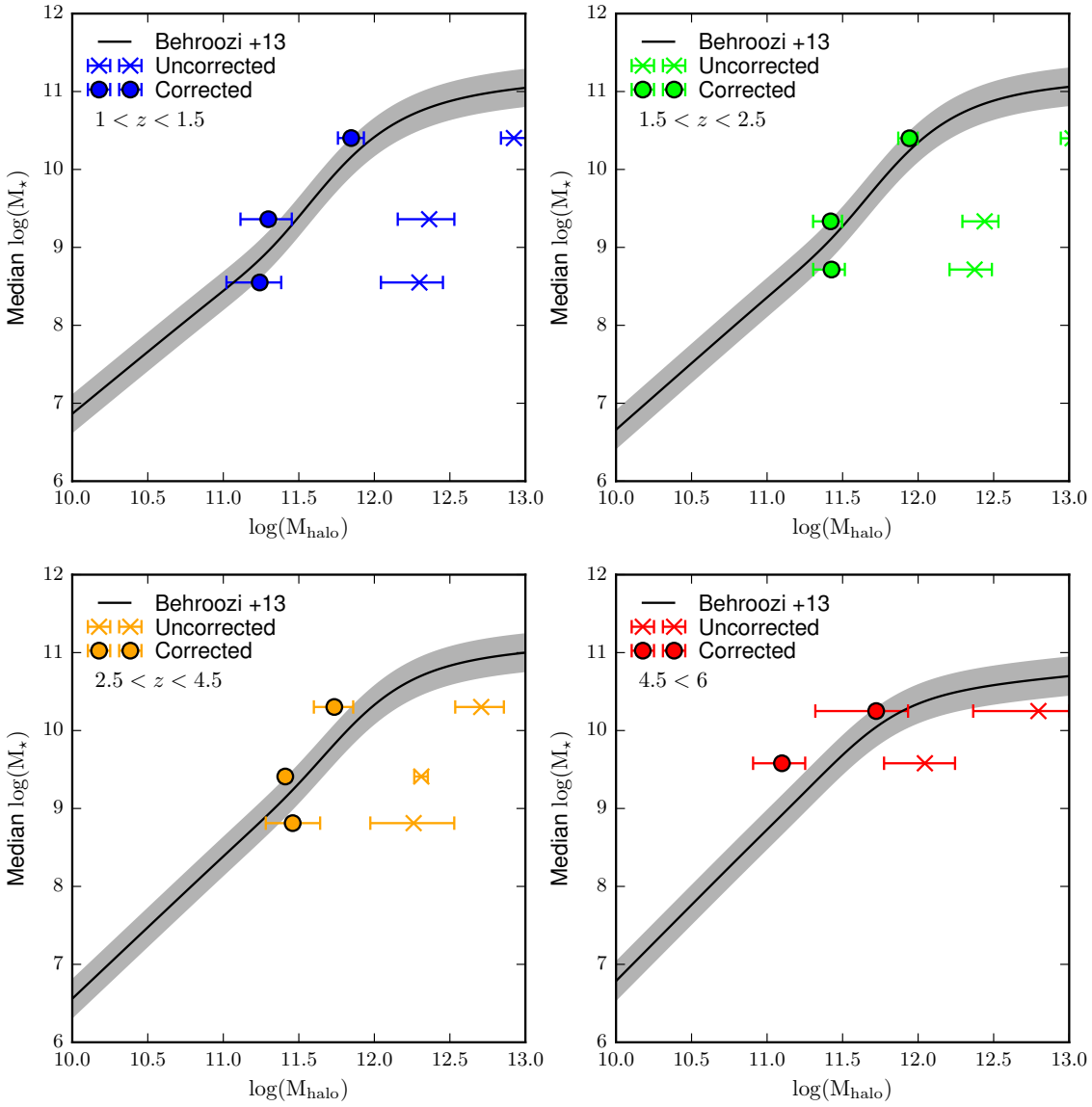

Figure 4.23: $M_\star\,(M_{\rm halo})$ relation in four bins of redshift for CANDELS galaxies with H-band magnitude less than 26. The points show the halo masses in bins of stellar mass both uncorrected and corrected. The black lines are $M_\star\,(M_{\rm halo})$ from Behroozi et al. (2013a) with the scatter shown in gray.

4.5 Discussion

In this chapter, we have discussed the calculation of halo masses from correlation functions via power law fitting. This technique is, in principle, the most straightforward way to estimate the halo mass from an angular correlation function, depending only on the assumption of linear, scale-independent bias. However there are subtleties in the measurement that have not been addressed in detail in the literature, which we identify and quantify. Through extensive tests on a catalog of halos drawn from an N-body simulation, we have identified that the standard estimates from measuring correlation functions on fields of the CANDELS geometry are biased high by up to an order of magnitude, and we use the simulations to calibrate and remove this bias.

Our halo mass estimates for galaxies in the CANDELS fields come from correlation functions calculated over 10"$< \theta <$350" in seven bins of separation with block bootstrap errors (see Section 4.3.2). We use the average redshift probability distribution function from SED fitting of the galaxies in each bin as the $N(z)$ to deproject our angular correlation functions to real-space correlation functions (see Section 4.4.1). We correct the biases from the deprojected fit parameters by using the SHAM results to infer bias overestimation as a function of measured bias and redshift (see Section 4.4.2). Last, we map the corrected biases to halo masses with the Tinker et al. (2010) $b(M_{\rm halo})$ relation at the median redshift of the objects in each bin. These masses are shown with abundance matching results in Figure 4.23.

Our masses are in good agreement with abundance matching results, particularly

considering that our error bars are lower limits on the true error: they include field-to-field variance but not error from the fitting, the $b\,(M_{\rm halo})$ relation, or the bias correction. We expect these additional sources of error to be sub-dominant. There are several potential sources of systematic uncertainty as well. We treat our measured galaxy bias as equivalent to halo bias. If galaxies are significantly biased with respect to halos, it would tend to bias our measurement towards higher halo masses. Our redshift estimation and our choice to use the median redshift $b\,(M_{\rm halo})$ relation may also affect our mass estimates, though this effect is likely small: our tests with the SHAM reproduced the known halo masses well.

In Figure 4.24, we show the bias as a function of redshift with several sets of published results. The three sets of biases we show are biases for Lyman Break Galaxies (LBGs) from the GOODS fields (Lee et al., 2006), CANDELS (Barone-Nugent et al., 2014), and CANDELS plus the Hubble Frontier Fields (HFF) parallels and Hyper Suprime-Cam data from the Subaru Strategic Program (HSC SSP) (Harikane et al., 2015). Lee et al. (2006) derive biases for LBGs in a similar manner as this work, calculating an angular correlation function over $10" < \theta \lesssim 200"$ and fitting a power law with β=0.6 with the Adelberger integral constraint correction. They convert their power law fit to bias via Equation 4.8 with $N\,(z)$ taken from applying their selection criteria to simulations.

Barone-Nugent et al. (2014) use LBGs from catalogs published by Bouwens et al. (2015) and McLure et al. (2013) in the CANDELS fields to compute angular correla-

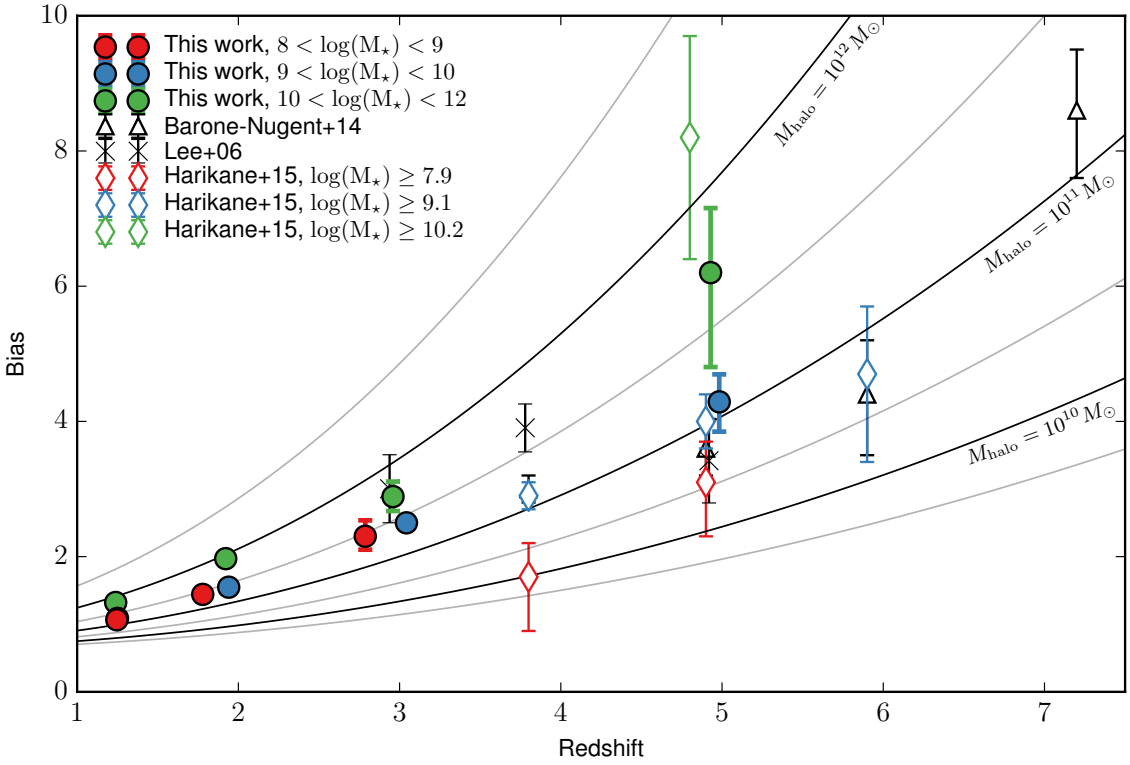

Figure 4.24: Bias as a function of redshift. Our work is shown as filled circles, with color denoting the stellar mass bin. The redshift used for our work is the median redshift of the galaxies in that bin. We show results for Lyman Break galaxies from Lee et al. (2006) as black crosses, from Barone-Nugent et al. (2014) as black triangles, and Harikane et al. (2015) as open diamonds whose colors denote stellar mass selection. We also show the bias as a function of redshift for halos with $\log(M_{\rm halo}) =$ 9.5, 10, 10.5, 11, 11.5, 12, and 12.5 as solid lines. Integer $\log(M_{\rm halo})$ curves are black and labeled with their halo mass. Half integer curves are gray.

tion functions for each field with linear binning over 0"$< \theta <$ 250" with bins of width 25" for redshift $z \sim 7.2$ and of width 12.5" otherwise. They fit each of these correlation functions with a power law with β=0.6 and the Adelberger integral constraint correction, then combine the fields. They deproject with the $N(z)$ from Bouwens et al. (2015) and calculate bias with Equation 4.8.

Harikane et al. (2015) study LBGs in the CANDELS data; the HFF parallels for HFF-Abell2744P and HFF-MACS0416P, which are observed to a limiting magnitude of 29 and cover 3.1 and 3.8 arcmin^2 respectively; and the HSC SSP data, which is observed to limiting r-band magnitude of 26, 27, and 28 over 1400, 27, and 3.5 deg^2 respectively. They calculate the correlation functions in logarithmically spaced bins from a few arcseconds to a few hundred arcseconds and apply the Adelberger integral constraint correction with fixed slope β=0.8. They then calculate the bias from the ratio of the real-space correlation functions at 8 h^{-1}Mpc by deprojecting their measured angular correlation functions with the full Limber equation, Equation 4.9, and the Bouwens et al. (2015) $N(z)$s. Harikane et al. (2015) calculate bias for samples with different limiting UV magnitudes, which they translate to a minimum stellar mass with the $M_\star - M_{UV}$ relation. In Figure 4.24, we show the samples that match most closely with our own stellar mass bins.

The Harikane et al. (2015) biases, which most resemble ours, are in agreement with our biases for the highest two mass bins, $9 < \log(\mathrm{M}_\star) < 10$ and $10 < \log(\mathrm{M}_\star) < 12$, at redshift $z \sim 5$. The $10 < \log(\mathrm{M}_\star) < 12$ bin seems to approximately follow

the $\log(M_{halo}) = 12$ bias curve, including both our results and the single Harikane et al. (2015) bias at that stellar mass. The $9 < \log(M_\star) < 10$ bin hovers around $\log(M_{halo}) = 11.5$ below redshift $z \sim 3$ and around $\log(M_{halo}) = 11$ at higher redshifts. The LBG samples from Lee et al. (2006) and Barone-Nugent et al. (2014), which have no stellar mass estimates, fall roughly in line with our $9 < \log(M_\star) < 10$ results at redshift $z \gtrsim 4$ and our $10 < \log(M_\star) < 12$ results at redshifts $z \lesssim 4$.

The lowest stellar mass bin, $8 < \log(M_\star) < 9$, has no overlap in redshift between our results the and Harikane et al. (2015) results. However, our measurements for this bin are close to $\log(M_{halo}) = 11.5$ and the Harikane et al. (2015) results are $\log(M_{halo}) = 10-10.5$. Assuming these two are genuinely representing the same stellar masses, there is little physical reason to expect such a jump. In addition, our results from the $8 < \log(M_\star) < 9$ bin fall on the same bias curve as our $9 < \log(M_\star) < 10$ results. This seems unlikely for stellar mass bins an order of magnitude different. Our halo masses for the $8 < \log(M_\star) < 9$ bin also tend to be higher than the others in comparison to abundance matching results (Figure 4.23). A possible explanation for this excess bias is the artificial clustering effects of completeness cut (Lee et al., 2006). Cutting at a limiting magnitude, in this case an H-band magnitude of 26, the 90% completeness limit in the CANDELS/Wide exposures, leaves a slight excess of galaxies in the deeper fields. This most strongly affects the faintest samples, or the lowest stellar mass bin.

One of the most striking features of Figure 4.24 is that our biases, corrected by

almost a factor of two, are roughly in agreement with other measurements of the bias which did not make this correction. The reasons for this agreement is unclear. All three sets of published results cover similar ranges in separation and fit power laws with a Adelberger integral constraint correction. They range from a smaller area (Lee et al., 2006) to an identical area (Barone-Nugent et al., 2014) to a significantly larger area (Harikane et al., 2015). The main difference between our sample and the published results is the redshift selection: we use photometric redshifts to select our bins and we compare to Lyman Break Galaxies. This shouldn't affect the results if the $N(z)$ used to deproject is accurate in both cases and Lyman Break Galaxies are drawn from the same population as the galaxies in the photometric redshift selection. However, at $z > 3$, we might expect the LBG selection to miss some of the most massive objects or underestimate their masses. Massive galaxies that start to shut down their star-formation will become redder and fainter faster than average and galaxies that become dusty may be red enough to evade LBG selection. Thus we expect our sample, which estimates stellar mass by fitting individual galaxies, to be more representative of the entire population at these redshifts and not just the blue, star-forming population. To test for effects from different selection criteria, future work could compare LBGs to a photometrically selected sample using the same correlation function calculation and analysis techniques on both. Tests with Lyman Break selection criteria applied to SAMs would also be enlightening.

4.6 Conclusion

Dark matter halos are distributed on the sky in a way that is related to their mass: high mass halos tend to be found in denser environments and low mass halos tend to be found in less dense environments. This difference can quantified by a halo population's bias. Bias is tightly related to halo mass and, with some assumptions, can be used to estimate an observed population's halo mass. The bias of a population can be derived from an angular correlation function, assuming that it is well-approximated by a power law. In this chapter, we have examined that process in detail.

There are many moving parts in this process of converting correlation functions to masses. First is the correlation function itself. As discussed in Section 4.3.2, the main parameter of import is the minimum separation, $\theta_{\rm min}$, particularly if the slope, β, is a free parameter. Fitting the correlation function requires a choice of β which affects the end result nontrivially. A change from β=0.6 to β=0.8, both values used in the literature, reduced the inferred halo mass by 0.5 dex for our example correlation function (Figure 4.20). The conversion from a power law in angular separation to a power law in physical separation requires a redshift distribution, $N\left(z\right)$. Choosing too wide a distribution results in masses that are too high and too narrow a distribution results in masses that are too low. Even with a redshift distribution known to be correct, as in the SHAM catalogs, the masses are systematically high (Section 4.4.2). We use the SHAM results to correct our measured biases for the CANDELS fields and convert to a halo mass using the Tinker et al. (2010) $b\left(M_{\rm halo}\right)$ relation.

With all the above concerns addressed, we measure the $M_\star\,(M_{\rm halo})$ relation in three bins of stellar mass and four bins of redshift for the CANDELS fields. We find masses in agreement with abundance matching results and biases in broad agreement with previous clustering measures. The main tension is in the lowest stellar mass bin, $8 < \log(\mathrm{M}_\star) < 9$. This bin may have some artificial clustering introduced by the completeness cut that we do not address in the placement of the randoms. In future work, we will implement a variable completeness treatment that will lay down randoms in a way that echoes the actual detection probability for galaxies. If the excess bias in the lowest mass bin is due to artificial clustering, a variable completeness treatment should give a lower bias in that bin.

Another test to facilitate the comparison between this work and the published biases we compare to would be to analyze in the same way galaxies selected with the Lyman break technique and galaxies selected with photometric redshifts. This test would also help identify why our biases require correction to match simulated halos' masses. Bouwens et al. (2015) compares the simulated LBG redshift distribution to the photometric redshifts of the same galaxies and finds that they are similar but not identical, which could affect the bias results somewhat. In addition, this would allow a comparison of the other properties of the two populations, particularly stellar masses. If the redshift distributions had little effect on the measured bias and the samples looked to be drawn from the same population, a halo occupation distribution model could be used to model the correlation functions in more detail.

In this chapter, we have measured the $M_\star\,(M_{\rm halo})$ relation at high redshift with clustering in the CANDELS fields, providing an independent confirmation of the commonly-used abundance matching results. We measured the two-point angular correlation function in bins of stellar mass and photometric redshift, avoiding possible incompleteness in galaxy samples selected with Lyman break criteria. In addition, we validated every step of the process from galaxy catalogs to halo masses, verifying that we could reproduce the known halo masses of simulated galaxies. The $M_\star\,(M_{\rm halo})$ relation provides an important constraint on galaxy formation and is often used to tune models of galaxy formation, so confirmation of results from the more indirect abundance matching $M_\star\,(M_{\rm halo})$ is encouraging.

Chapter 5

Conclusions

The $M_\star\,(M_{\rm halo})$ relation describes how stellar mass inhabits dark matter halos and places an important constraint on galaxy formation models. Most often, models compare to $M_\star\,(M_{\rm halo})$ as estimated by abundance matching, an empirical model that matches observed stellar masses to theoretical dark matter halos. The majority of modeled low mass galaxies produce their stars earlier in their lives than observations, including $M_\star\,(M_{\rm halo})$, would suggest. This results in stellar masses that are too high at high redshift and star formation rates that are too low today. In Chapter 2, we explored this problem by introducing physically motivated alterations into the Santa Cruz semi-analytic model of galaxy formation (Somerville et al., 2008b, 2012). In Chapters 3 and 4, we measure the $M_\star\,(M_{\rm halo})$ relation with correlation functions in the CANDELS fields, a constraint independent from abundance matching.

In Chapter 2, the three alterations we made to the semi-analytic model (SAM)

were designed to simulate star formation suppression from (1) more effective supernova feedback at higher redshifts, (2) less efficient star formation at higher redshifts, and (3) less efficient gas accretion into lower-mass halos. All three approaches produced results closer to the $M_\star\,(M_{\rm halo})$ relation from abundance matching than the fiducial SAM. However, the three differed greatly in the extremity of the changes required. The direct suppression of star formation, option (2) in the list, is the least tractable method, requiring star formation suppression drastic enough to be in conflict with observations of star formation in local galaxies. Preferential reheating, option (1), was fairly simple to adapt to the observed $M_\star\,(M_{\rm halo})$ relation, but requires outflow efficiencies to be a far steeper function of halo mass than expected from basic scaling arguments. The most promising of the options was the parking lot model, option (3), where gas falling into the halo is held in a "parking lot" for some time before it can accrete onto the galaxy. The way in which gas falls into halos is poorly constrained by observations, so the parking lot model is within our uncertainties on how models should handle accretion.

The parking lot model successfully delays star formation in low mass galaxies, improving the model's agreement with observations. This can be seen in the evolution of the $M_\star\,(M_{\rm halo})$ relation, the low mass end of the galaxy stellar mass function, and the specific star formation rates. One of the crucial aspects of getting the parking lot model to work was a detail of bookkeeping: in the fiducial model, satellites are stripped of their gas when they merge with a larger galaxy. The gas lost from the

satellite is added to the central's hot gas halo and immediately allowed to cool and form stars. The principle behind the parking lot model is that gas cannot easily *enter* low mass halos, but the behavior of the gas already in the halo is unchanged. The gas from satellites is a significant fraction of new gas accreting onto halos, particularly at early times. In order for the parking lot model to work, gas stripped from satellites must held outside of the halo instead of allowed into the hot gas halo. The parking lot model set up this way is similar to the model of Henriques et al. (2013, 2015), who also find success with delayed accretion.

In Chapters 3 and 4, we derive the $M_\star\left(M_{\rm halo}\right)$ relation from redshifts $z \sim 1-5$ using clustering in the CANDELS fields. The angular two-point correlation function, a clustering metric, can be used to estimate typical halo masses for a population of interest. Specifically, we fit the angular correlation function with a power law in bins of stellar mass and redshift, then use theoretical results to convert the power law fit coefficients to halo masses. The process to go from a list of galaxy positions on the sky to a halo mass contains many subtleties, so we examine each choice carefully and verify our results with simulated halos, showing that the process successfully reproduces the correct halo mass. We do find that the standard procedure is biased to masses higher than the actual halo mass, so we calibrate our method with the simulations. The reason this calibration is necessary is unclear.

In Figure 5.1, we compare the semi-analytic model results from Chapter 2 to the $M_\star\left(M_{\rm halo}\right)$ relation from our clustering work in Chapter 4 and to abundance match-

ing results from (Behroozi et al., 2013a). For the SAM, we show the fiducial model, the preferential reheating model, and the parking lot model with reinfall timescale $\tau_{\rm PL} \propto M_{\rm vir}^{-1}$. The two adjusted models match both the abundance matching and the clustering $M_\star\,(M_{\rm halo})$ results better than the fiducial model. The clustering results agree well with abundance matching, which is encouraging because the two are entirely independent.

Both the models and the observations of the $M_\star\,(M_{\rm halo})$ relation are imperfect. Currently, no model of galaxy formation reproduces galaxies' star formation histories while also matching other galaxy properties, though the newest generation of models are making definite improvements. Furlong et al. (2015) address star formation in low mass galaxies with the EAGLE hydrodynamic simulations. One of the recipe adaptations they try introduces a metallicity and density dependence to the supernova feedback recipe. This makes outflows at higher redshift more efficient relative to lower redshift, similar to the preferential reheating adaptation, and delays star formation somewhat in low mass galaxies. The effect is not enough to match observations, but it is a step in the right direction. Davé et al. (2016) compare the fiducial MUFASA simulation to galaxy stellar mass functions and find that it performs better than other fiducial hydrodynamic models, matching galaxy stellar mass functions well from redshifts $z = 0 - 4$. They attribute their success with low mass galaxies to the use of feedback from massive stars (equivalent to our supernova feedback) from the FIRE high-resolution simulations. Hirschmann et al. (2016) work with the GAEA semi-

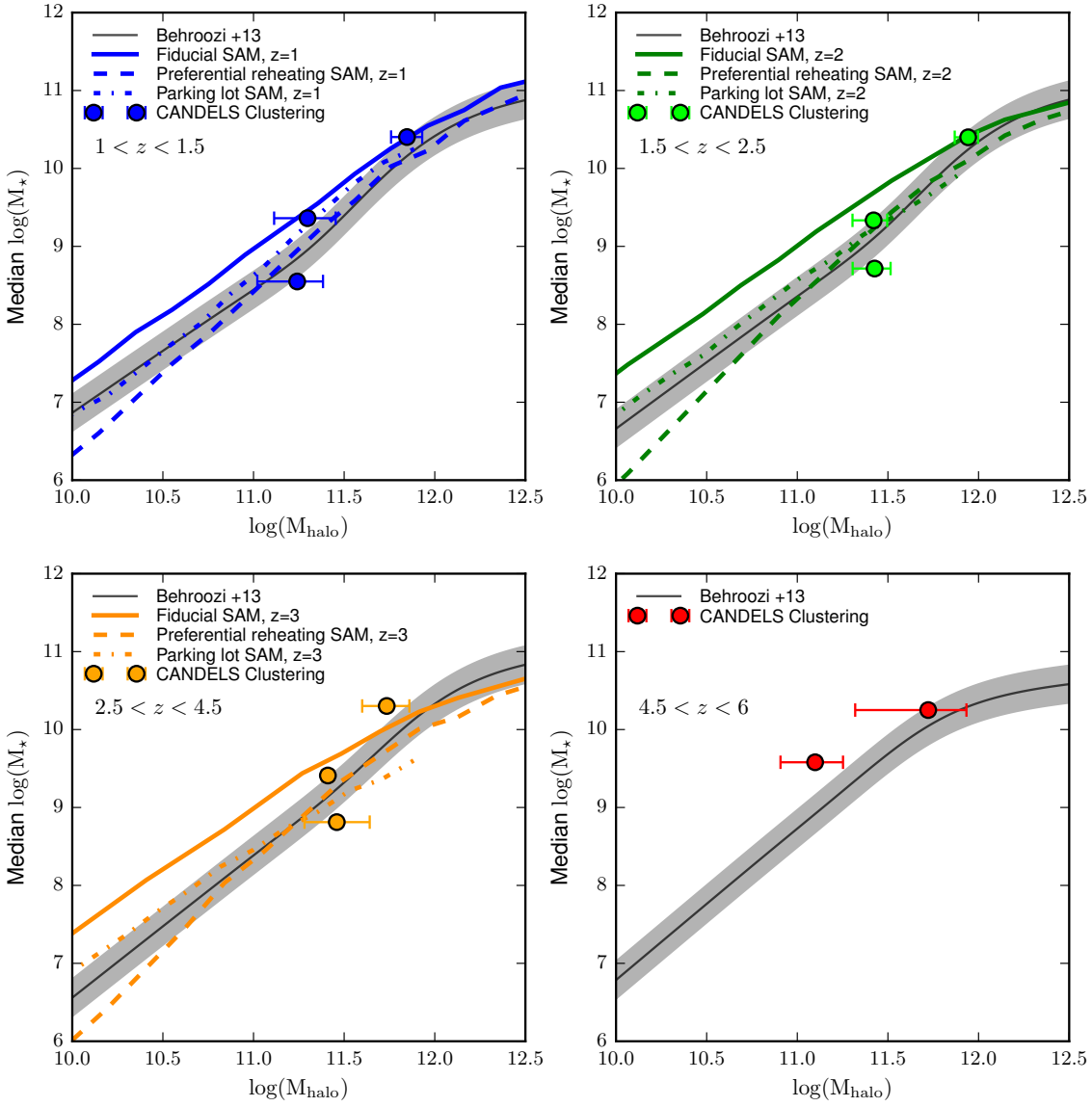

Figure 5.1: The $M_\star\,(M_{\rm halo})$ relation from the Santa Cruz semi-analytic model, from clustering in the CANDELS fields, and from Behroozi et al. (2013a). In each panel, the Behroozi et al. (2013a) results are shown in black with uncertainties in gray and our clustering measurements are shown by the colored points. The SAM results for the fiducial model, the preferential reheating model, and the parking lot model are shown as solid, dashed, and dot-dashed lines respectively. Note that the redshifts for the SAM $M_\star\,(M_{\rm halo})$ are slightly different than for the clustering bins, with the SAM redshifts noted in the legends.

analytic model to simultaneously reproduce the galaxy stellar mass function and metallicities. They find that a preventative feedback mechanism like the parking lot model can reproduce the stellar masses but not the metallicities, while ejective feedback like the preferential reheating model can reproduce both the stellar masses and metallicities.

On the observational front, abundance matching has done an excellent job of adapting to match more and more of the observed galaxy trends, such as the color-dependence of clustering (Hearin & Watson, 2013). Direct measurements of halo masses from clustering are stretching to higher redshifts (Barone-Nugent et al., 2014; Harikane et al., 2015) and our work has made a significant step towards robust clustering measurements of the high redshift $M_\star\,(M_{\rm halo})$ relation. Extending these measurements to even higher redshifts and lower stellar masses will provide valuable constraints on models in regimes where the abundance matching results are entirely extrapolated. Our work used only galaxies brighter than 26th magnitude in the H-band, but future work will use a more sophisticated completeness treatment that will allow the use of all the galaxies in the CANDELS fields, improving the measurements presented here. Future deep observations of faint, high redshift galaxies will open up the possibility of making these measurements over a wider range in stellar mass and redshift.

In addition to further observations, more study is needed on the methods used to make clustering measurements of halo mass. The approach we use to extract halo

masses from power law fits has its strengths, but is not perfect nor is it the only way in which halo masses may be derived from clustering. A systematic comparison of the different methods of halo mass derivation on simulated galaxies could pinpoint the cause of our overestimation of the bias and determine the optimal way of extracting halo masses from clustering. Determining halo mass from the ratio of the galaxy correlation function to the linear dark matter correlation function relies on similar assumptions as our work, but does not require that the correlation function be well-described by a power law. Halo occupation distributions would account for both the shape of the correlation function and the distributions of galaxy masses and redshifts within a bin. A comparison of the biases derived from the same correlation functions in all three ways would narrow down the reasons the naive power law bias differs from the expected bias in our tests on simulated halos.

In summary, in this thesis, we have worked to reconcile the observed $M_\star\,(M_{\rm halo})$ relation with predictions from models. We find that the current model of star formation regulated by ejective feedback has a remarkable tendency to build up stellar mass in low-mass galaxies sooner than predicted by abundance matching and that we can successfully correct this tendency with adaptations of either ejective or preventative feedback, our preferential reheating and parking lot models. We measure the $M_\star\,(M_{\rm halo})$ relation with clustering in the CANDELS fields, the first high redshift measurement of correlation functions in bins of stellar mass and photometric redshift, and we find good agreement with abundance matching results. The ten-

sion between the majority of galaxy formation models and the observed $M_\star\,(M_{\rm halo})$ relation remains, although the newest generation of models are less discrepant. In the future, continued deep observations of high redshift galaxies will allow for even more detailed measurement of the $M_\star\,(M_{\rm halo})$ relation, constraining galaxy formation models further.

Bibliography

Abbott, B. P., et al. 2016, Physical Review Letters, 116, 131103

Adelberger, K. L., Steidel, C. C., Pettini, M., Shapley, A. E., Reddy, N. A., & Erb, D. K. 2005, ApJ, 619, 697

Andrae, R., Schulze-Hartung, T., & Melchior, P. 2010, ArXiv e-prints

Angulo, R. E., Springel, V., White, S. D. M., Jenkins, A., Baugh, C. M., & Frenk, C. S. 2012, MNRAS, 426, 2046

Baldry, I. K., et al. 2012, MNRAS, 421, 621

Baldry, I. K., Glazebrook, K., & Driver, S. P. 2008, MNRAS, 388, 945

Barone-Nugent, R. L., et al. 2014, ApJ, 793, 17

Bauer, D., et al. 2015, Physics of the Dark Universe, 7, 16

Behroozi, P. S., Conroy, C., & Wechsler, R. H. 2010, ApJ, 717, 379

Behroozi, P. S., Wechsler, R. H., & Conroy, C. 2013a, ApJ, 770, 57

Behroozi, P. S., Wechsler, R. H., Lu, Y., Hahn, O., Busha, M. T., Klypin, A., & Primack, J. R. 2014, ApJ, 787, 156

Behroozi, P. S., Wechsler, R. H., & Wu, H.-Y. 2013b, ApJ, 762, 109

BIBLIOGRAPHY

Behroozi, P. S., Wechsler, R. H., Wu, H.-Y., Busha, M. T., Klypin, A. A., & Primack, J. R. 2013c, ApJ, 763, 18

Benson, A. J., Cole, S., Frenk, C. S., Baugh, C. M., & Lacey, C. G. 2000, MNRAS, 311, 793

Berlind, A. A., & Weinberg, D. H. 2002, ApJ, 575, 587

Bertin, E., & Arnouts, S. 1996, A&AS, 117, 393

Bigiel, F., Leroy, A., Walter, F., Brinks, E., de Blok, W. J. G., Madore, B., & Thornley, M. D. 2008, AJ, 136, 2846

Binney, J., & Tremaine, S. 2008, Galactic Dynamics: (Second Edition), Princeton Series in Astrophysics (Princeton University Press)

Bouché, N., et al. 2010, ApJ, 718, 1001

Bouwens, R. J., et al. 2015, ApJ, 803, 34

Boylan-Kolchin, M., Ma, C.-P., & Quataert, E. 2008, MNRAS, 383, 93

Bruzual, G., & Charlot, S. 2003, MNRAS, 344, 1000

Cabré, A., Fosalba, P., Gaztañaga, E., & Manera, M. 2007, MNRAS, 381, 1347

Coil, A. L. 2013, The Large-Scale Structure of the Universe, ed. T. D. Oswalt & W. C. Keel, 387

Coil, A. L., et al. 2004, ApJ, 609, 525

—. 2008, ApJ, 672, 153

Cole, S., et al. 2001, MNRAS, 326, 255

Conroy, C., & Wechsler, R. H. 2009, ApJ, 696, 620

BIBLIOGRAPHY

Conselice, C. J. 2012, ArXiv e-prints

Dahlen, T., et al. 2013, ApJ, 775, 93

Davé, R., Finlator, K., & Oppenheimer, B. D. 2011, MNRAS, 416, 1354

Davé, R., Thompson, R. J., & Hopkins, P. F. 2016, MUFASA: Galaxy Formation Simulations With Meshless Hydrodynamics

de la Torre, S., et al. 2013, A&A, 557, A54

Duncan, K., et al. 2014, MNRAS, 444, 2960

Dunne, L., et al. 2009, MNRAS, 394, 3

Efstathiou, G. 1992, MNRAS, 256, 43P

Erb, D. K., Shapley, A. E., Pettini, M., Steidel, C. C., Reddy, N. A., & Adelberger, K. L. 2006, ApJ, 644, 813

Fontanot, F., De Lucia, G., Monaco, P., Somerville, R. S., & Santini, P. 2009, MNRAS, 397, 1776

Furlong, M., et al. 2015, MNRAS, 450, 4486

Galametz, A., et al. 2013, ApJS, 206, 10

Gallazzi, A., Charlot, S., Brinchmann, J., White, S. D. M., & Tremonti, C. A. 2005, MNRAS, 362, 41

Gawiser, E., et al. 2006, ApJS, 162, 1

Giavalisco, M., & Dickinson, M. 2001, ApJ, 550, 177

Giocoli, C., Tormen, G., Sheth, R. K., & van den Bosch, F. C. 2010, MNRAS, 404, 502

BIBLIOGRAPHY

Gnedin, N. Y. 2000, ApJ, 542, 535

Gottloeber, S., & Klypin, A. 2008, ArXiv e-prints

Greene, J. E. 2012, Nature Communications, 3, 1304

Grogin, N. A., et al. 2011, ApJS, 197, 35

Guo, H., et al. 2016, MNRAS, 459, 3040

Guo, Q., et al. 2011, MNRAS, 413, 101

Guo, Y., et al. 2013, ApJS, 207, 24

Haas, M. R., Schaye, J., Booth, C. M., Dalla Vecchia, C., Springel, V., Theuns, T., & Wiersma, R. P. C. 2013, MNRAS, 435, 2931

Hanasz, M., Lesch, H., Naab, T., Gawryszczak, A., Kowalik, K., & Wóltański, D. 2013, ApJ, 777, L38

Harikane, Y., et al. 2015, ArXiv e-prints

Hartley, W. G., Conselice, C. J., Mortlock, A., Foucaud, S., & Simpson, C. 2015, MNRAS, 451, 1613

Hawkins, E., et al. 2003, MNRAS, 346, 78

Hayward, C. C., Behroozi, P. S., Somerville, R. S., Primack, J. R., Moreno, J., & Wechsler, R. H. 2013, MNRAS, 434, 2572

Hayward, C. C., & Hopkins, P. F. 2015, ArXiv e-prints

Hearin, A. P., & Watson, D. F. 2013, MNRAS, 435, 1313

Hearin, A. P., Watson, D. F., & van den Bosch, F. C. 2015, MNRAS, 452, 1958

Hearin, A. P., Zentner, A. R., van den Bosch, F. C., Campbell, D., & Tollerud, E.

2016, MNRAS

Henriques, B. M. B., White, S. D. M., Thomas, P. A., Angulo, R., Guo, Q., Lemson, G., Springel, V., & Overzier, R. 2015, MNRAS, 451, 2663

Henriques, B. M. B., White, S. D. M., Thomas, P. A., Angulo, R. E., Guo, Q., Lemson, G., & Springel, V. 2013, MNRAS, 431, 3373

Hirschmann, M., De Lucia, G., & Fontanot, F. 2016, MNRAS

Hopkins, P. F., Quataert, E., & Murray, N. 2012, MNRAS, 421, 3522

Horesh, A., Maoz, D., Hilbert, S., & Bartelmann, M. 2011, MNRAS, 418, 54

Jena, T., et al. 2005, MNRAS, 361, 70

Jing, Y. P. 2005, ApJ, 620, 559

Kajisawa, M., Ichikawa, T., Yamada, T., Uchimoto, Y. K., Yoshikawa, T., Akiyama, M., & Onodera, M. 2010, ApJ, 723, 129

Karim, A., et al. 2011, ApJ, 730, 61

Kauffmann, G., Li, C., Zhang, W., & Weinmann, S. 2013, MNRAS, 430, 1447

Kennicutt, Jr., R. C. 1998, ApJ, 498, 541

Kewley, L. J., & Ellison, S. L. 2008, ApJ, 681, 1183

Kim, J., Park, C., Rossi, G., Lee, S. M., & Gott, III, J. R. 2011, Journal of Korean Astronomical Society, 44, 217

Klypin, A., Yepes, G., Gottlöber, S., Prada, F., & Heß, S. 2016, MNRAS, 457, 4340

Koekemoer, A. M., et al. 2011, ApJS, 197, 36

Komatsu, E., et al. 2009, ApJS, 180, 330

Kormendy, J., & Ho, L. C. 2013, ARA&A, 51, 511

Kravtsov, A. V., Berlind, A. A., Wechsler, R. H., Klypin, A. A., Gottlöber, S., Allgood, B., & Primack, J. R. 2004a, ApJ, 609, 35

Kravtsov, A. V., Gnedin, O. Y., & Klypin, A. A. 2004b, ApJ, 609, 482

Kravtsov, A. V., Klypin, A. A., & Khokhlov, A. M. 1997, ApJS, 111, 73

Krumholz, M. R., & Dekel, A. 2012, ApJ, 753, 16

Kuhlen, M., Diemand, J., Madau, P., & Zemp, M. 2008, Journal of Physics Conference Series, 125, 012008

Laidler, V. G., et al. 2007, PASP, 119, 1325

Landy, S. D., & Szalay, A. S. 1993, ApJ, 412, 64

Lee, K.-S., et al. 2012, ApJ, 752, 66

Lee, K.-S., Giavalisco, M., Conroy, C., Wechsler, R. H., Ferguson, H. C., Somerville, R. S., Dickinson, M. E., & Urry, C. M. 2009, ApJ, 695, 368

Lee, K.-S., Giavalisco, M., Gnedin, O. Y., Somerville, R. S., Ferguson, H. C., Dickinson, M., & Ouchi, M. 2006, ApJ, 642, 63

Limber, D. N. 1953, ApJ, 117, 134

Lu, Y., Mo, H. J., & Wechsler, R. H. 2015, MNRAS, 446, 1907

Lu, Y., et al. 2014, ApJ, 795, 123

Maiolino, R., et al. 2008, A&A, 488, 463

Marchesini, D., van Dokkum, P. G., Förster Schreiber, N. M., Franx, M., Labbé, I., & Wuyts, S. 2009, ApJ, 701, 1765

Matthews, D. J., & Newman, J. A. 2012, ApJ, 745, 180

McLure, R. J., et al. 2013, MNRAS, 432, 2696

Mo, H. J., Jing, Y. P., & Boerner, G. 1992, ApJ, 392, 452

Mo, H. J., Mao, S., & White, S. D. M. 1998, MNRAS, 295, 319

Mobasher, B., et al. 2015, ApJ, 808, 101

Mortlock, A., et al. 2015, MNRAS, 447, 2

Moster, B. P., Naab, T., & White, S. D. M. 2013, MNRAS, 428, 3121

Moster, B. P., Somerville, R. S., Maulbetsch, C., van den Bosch, F. C., Macciò, A. V., Naab, T., & Oser, L. 2010, ApJ, 710, 903

Moustakas, J., et al. 2013, ApJ, 767, 50

Narayanan, D., Bothwell, M., & Davé, R. 2012, MNRAS, 426, 1178

Norberg, P., Baugh, C. M., Gaztañaga, E., & Croton, D. J. 2009, MNRAS, 396, 19

Okamoto, T., Gao, L., & Theuns, T. 2008, MNRAS, 390, 920

Oppenheimer, B. D., Davé, R., Kereš, D., Fardal, M., Katz, N., Kollmeier, J. A., & Weinberg, D. H. 2010, MNRAS, 406, 2325

Ouchi, M., et al. 2005, ApJ, 635, L117

Panter, B., Jimenez, R., Heavens, A. F., & Charlot, S. 2007, MNRAS, 378, 1550

Peacock, J. A., & Dodds, S. J. 1996, MNRAS, 280, L19

Peebles, P. J. E. 1980, The large-scale structure of the universe

Peeples, M. S., Werk, J. K., Tumlinson, J., Oppenheimer, B. D., Prochaska, J. X., Katz, N., & Weinberg, D. H. 2014, ApJ, 786, 54

BIBLIOGRAPHY

Planck Collaboration et al. 2015, ArXiv e-prints

Popping, G., Behroozi, P. S., & Peeples, M. S. 2014a, ArXiv e-prints

Popping, G., Somerville, R. S., & Trager, S. C. 2014b, MNRAS, 442, 2398

Quinn, T., Katz, N., & Efstathiou, G. 1996, MNRAS, 278, L49

Roche, N., & Eales, S. A. 1999, MNRAS, 307, 703

Rodriguez-Puebla, A., Behroozi, P., Primack, J., Klypin, A., Lee, C., & Hellinger, D. 2016, ArXiv e-prints

Salim, S., et al. 2007, ApJS, 173, 267

Santini, P., et al. 2012, A&A, 538, A33

Savaglio, S., et al. 2005, ApJ, 635, 260

Schechter, P. 1976, ApJ, 203, 297

Shepherd, C. W., Carlberg, R. G., Yee, H. K. C., & Ellingson, E. 1997, ApJ, 479, 82

Silk, J., & Mamon, G. A. 2012, Research in Astronomy and Astrophysics, 12, 917

Somerville, R. S. 2002, ApJ, 572, L23

Somerville, R. S., et al. 2008a, ApJ, 672, 776

Somerville, R. S., & Davé, R. 2015, ARA&A, 53, 51

Somerville, R. S., Gilmore, R. C., Primack, J. R., & Domínguez, A. 2012, MNRAS, 423, 1992

Somerville, R. S., Hopkins, P. F., Cox, T. J., Robertson, B. E., & Hernquist, L. 2008b, MNRAS, 391, 481

Somerville, R. S., & Kolatt, T. S. 1999, MNRAS, 305, 1

Somerville, R. S., & Primack, J. R. 1999, MNRAS, 310, 1087

Spergel, D. N., et al. 2007, ApJS, 170, 377

Tinker, J. L., Robertson, B. E., Kravtsov, A. V., Klypin, A., Warren, M. S., Yepes, G., & Gottlöber, S. 2010, ApJ, 724, 878

Tinker, J. L., Weinberg, D. H., Zheng, Z., & Zehavi, I. 2005, ApJ, 631, 41

Tomczak, A. R., et al. 2014, ApJ, 783, 85

Torrey, P., Cox, T. J., Kewley, L., & Hernquist, L. 2013, in Astronomical Society of the Pacific Conference Series, Vol. 477, Galaxy Mergers in an Evolving Universe, ed. W.-H. Sun, C. K. Xu, N. Z. Scoville, & D. B. Sanders, 237

Tremonti, C. A., et al. 2004, ApJ, 613, 898

Tumlinson, J., et al. 2013, ApJ, 777, 59

—. 2011, Science, 334, 948

van den Bosch, F. C., Yang, X., & Mo, H. J. 2003, MNRAS, 340, 771

van den Bosch, F. C., et al. 2007, MNRAS, 376, 841

Vargas-Magaña, M., et al. 2013, A&A, 554, A131

Weinberg, D. H., Croft, R. A. C., Hernquist, L., Katz, N., & Pettini, M. 1999, ApJ, 522, 563

Weinmann, S. M., Pasquali, A., Oppenheimer, B. D., Finlator, K., Mendel, J. T., Crain, R. A., & Macciò, A. V. 2012, MNRAS, 426, 2797

Weinmann, S. M., van den Bosch, F. C., Yang, X., & Mo, H. J. 2006, MNRAS, 366, 2

BIBLIOGRAPHY

White, C. E., Somerville, R. S., & Ferguson, H. C. 2015, ApJ, 799, 201

White, S. D. M., & Frenk, C. S. 1991, ApJ, 379, 52

Zehavi, I., et al. 2002, ApJ, 571, 172

—. 2004, ApJ, 608, 16

—. 2011, ApJ, 736, 59

Vita

Catherine White received her Bachelor of Science degree from the University of Maryland, College Park in 2009 with a double major in Physics and Astronomy. She enrolled in the Physics and Astronomy PhD program at Johns Hopkins University the following fall with a Davidsen Fellowship from the Space Telescope Science Institute. Her first year, she started working with Rachel Somerville on galaxy formation models. In 2012, she began work with the CANDELS team, transitioning from galaxy modeling to observational clustering measures with Harry Ferguson. Starting in September 2016, Catherine will begin work at Booz Allen Hamilton as a data science consultant.